

UC Riverside

UC Riverside Electronic Theses and Dissertations

Title

Surface Modification of Magnesium and its Alloys for Orthopedic Applications

Permalink

<https://escholarship.org/uc/item/2771w7r7>

Author

Lin, Jiajia

Publication Date

2021

Peer reviewed|Thesis/dissertation

UNIVERSITY OF CALIFORNIA
RIVERSIDE

Surface Modification of Magnesium and its Alloys for Orthopedic Applications

A Dissertation submitted in partial satisfaction
of the requirements for the degree of

Doctor of Philosophy

in

Materials Science & Engineering

by

Jiajia Lin

June 2021

Dissertation Committee:

Dr. Huinan Liu, Chairperson

Dr. Cengiz Ozkan

Dr. Manuela Martins-Green

Copyright by
Jiajia Lin
2021

The Dissertation of Jiajia Lin is approved:

Committee Chairperson

University of California, Riverside

Acknowledgements

Firstly, I would like to thank my PhD advisor, Dr. Huinan Liu for her continuous support and guidance on my PhD study. I also want to thank the rest of my committee, Dr. Cengiz Ozkan and Dr. Manuela Martins-Green, for their insightful and professional feedback on my dissertation. My sincere thanks also go to my colleagues in Liu lab, Dr. Aaron Cipriano, Dr. Qiaomu Tian, Dr. Naiyin Zhang, Dr. Wensen Jiang, Dr. Chaoxing Zhang, Nhu Nguyen, Changlu Xu, Dongwei Sun, Patricia Holt-Torres, Ruoyu Sheng, Yiqing Chen and Wayne Leu for their kind help on my research.

My deep and sincere gratitude to my family for their continuous and unparalleled love, help and support. I am extremely grateful to my beloved husband Shitong Zhu for always being there for me as a lifetime partner and friend. I am forever indebted to my parents for giving me the opportunities and experiences that have made me who I am. I greatly appreciate the supports from my best friends Jing Liu, Wenshan Lin, Xinxin Xu, Guiduan Xu and Ying Chen for their continuous support and inspiration in my life.

The text of this dissertation Chapter 1, in full, is a reprint of the material as it appears in the following publication: “Antimicrobial properties of MgO Nanostructures on Magnesium Substrates. ACS Omega. 2020, 5(38): 24613-24627”, in which I am the first author.

The rest chapters of this dissertation, in part or in full, will be presented in future publications. I would like to thank all the following co-authors for their contributions:

Chapter 2: *In Vitro* Degradation, Cytocompatibility, and Antimicrobial properties of Nanostructured Oxides on Magnesium Alloys

Authors: Jiajia Lin, Patricia Holt-Torres, Changlu Xu, Dongwei Sun, Yiqing Chen, Diana Sapigao, Katie Garwood, Gilberto Luis Peraza-Martinez, Huinan Liu

Chapter 3: *In Vitro* Degradation, Cytocompatibility, and Antimicrobial properties of Micro and Nano-micro Hydroxyapatite Loaded with Gentamicin Coated Magnesium

Authors: Jiajia Lin, Chaoxing Zhang, Nhu Nhuyen, Changlu Xu, Arash Aslani, Huinan Liu

Finally, I would like to acknowledge the financial support from the U.S. National Institutes of Health (NIAMS award 1R03AR069373), U.S. National Science Foundation (CBET award 1512764, 1125801), Burroughs Wellcome Fund (1011235), Hellman Faculty Fellowship (Huinan Liu), and the University of California (UC) Regents Faculty Development Award (Huinan Liu). UC-Riverside Dissertation Year Program Grant and Dissertation Research Grant (Jiajia Lin), and UC-Riverside Undergraduate Research Mini-grant (Alexandra Ha) Any opinions, findings, and conclusions or recommendations expressed in this article are those of the authors and do not necessarily reflect the views of the funding agencies.

ABSTRACT OF THE DISSERTATION

Surface Modification of Magnesium and its Alloys for Orthopedic Applications

by

Jiajia Lin

Doctor of Philosophy, Graduate Program in Materials Science & Engineering
University of California, Riverside, June 2021
Dr. Huinan Liu, Chairperson

In recent years, Magnesium (Mg) and its alloys as bioresorbable metals have attracted increasing attention for orthopedic implant applications because of their promising mechanical and biological properties. However, the rapid degradation of pure Mg remains a key challenge toward its clinical translations. Additionally, implant infections continue to be a significant clinical problem for orthopedic applications. This dissertation develops two approaches to improve the overall performance of pure Mg. One method includes engineering a nanostructured oxide surface onto the Mg coupled with adding alloying elements into the Mg matrix, the other involves depositing a nano-micro and micro hydroxyapatite supplemented with gentamicin onto the Mg. The nanostructured oxides on Mg alloy and pure Mg resulted in a slower electrochemical degradation rate, and reduced adhesion of methicillin-resistant *Staphylococcus aureus* (MRSA) on their surfaces when compared with the corresponding non-treated Mg controls. Moreover, the soluble degradation products released from nanostructured oxides on the Mg alloy and pure Mg

did not affect the growth of bone marrow derived mesenchymal cells (BMSCs) under indirect contact, but showed reduced cell spreading and adhesion under direct contact when compared with Ti control and glass reference. In terms of the nano-micro and micro hydroxyapatite supplemented with gentamicin coated Mg, the 12-week immersion study showed that the difference in the degradation rate between the hydroxyapatite coated Mg samples and the Mg controls is negligible because no statistically significant difference was found. The micro hydroxyapatite coated Mg samples did not affect the growth of BMSCs under indirect contact, but showed reduced cell spreading and adhesion under direct contact when compared with the Ti control and glass reference. The micro hydroxyapatite supplemented with 30 wt. % gentamicin coated Mg exhibited significantly lower adhesion of *Staphylococcus aureus* on the surface among all samples *in vitro*. Overall, this dissertation provides extensive knowledge regarding surface treatments on Mg and applying alloying elements into Mg to achieve desired performance toward clinical translations.

Table of Contents

Acknowledgements.....	iv
ABSTRACT OF THE DISSERTATION.....	vi
Introduction.....	1
Chapter 1 Antimicrobial Properties of MgO Nanostructures on Magnesium Substrates	4
Abstract.....	5
1.1 Introduction.....	6
1.2 Materials and Methods.....	11
1.3 Results.....	19
1.4 Discussion.....	37
1.5 Conclusions.....	49
Chapter 2 <i>In Vitro</i> Degradation, Cytocompatibility, and Antimicrobial Properties of Nanostructured Oxides on Magnesium Alloys	51
Abstract.....	52
2.1 Introduction.....	53
2.2 Materials and Methods.....	57
2.3 Results.....	66
2.4 Discussion.....	87
2.5 Conclusions.....	94
Chapter 3 <i>In Vitro</i> Degradation, Cytocompatibility, and Antimicrobial Properties of Micro and Nano-micro Hydroxyapatite Loaded with Gentamicin Coated Magnesium...	96
Abstract.....	97
3.1 Introduction.....	98
3.2 Materials and Methods.....	100
3.3 Results.....	107
3.4 Discussion.....	131
3.5 Conclusions.....	134
References.....	136

List of Figures

Figure 1-1: Schematic illustration.....	11
Figure 1-2: Characterization of surface microstructure and composition	21
Figure 1-3: X-ray diffraction (XRD) patterns.....	22
Figure 1-4: Cross-sectional characterization of the surface-treated Mg samples	24
Figure 1-5: Micro-scratch testing for interfacial adhesion strength.....	26
Figure 1-6: Surface topography, surface roughness, surface area and contact angle measurements.....	29
Figure 1-7: Bacterial density after being cultured in TSB	31
Figure 1-8: Characterization of surface microstructure and composition after 24-h of bacterial culture.....	35
Figure 1-9: X-ray diffraction patterns of the surface-treated Mg samples and Mg control after 24-h bacterial culture.	37
Figure 2-1: Anodic polarization curves and SEM images	69
Figure 2-2: Representative potential dynamic polarization (PDP) curves.....	72
Figure 2-3: BMSC adhesion	74
Figure 2-4: BMSC adhesion	76
Figure 2-5: Analysis of solubilized degradation products in the culture media	78
Figure 2-6: CFUs of MRSA after 24-h culture	80
Figure 2-7: SEM images and EDS maps	82
Figure 2-8: The quantitative elemental compositions.....	84
Figure 2-9: Analysis of solubilized degradation products in culture media	86

Figure 3-1: Surface characterization and elemental composition	109
Figure 3-2: Fluorescence images of BMSCs under direct contact and indirect contact .	111
Figure 3-3: Adhesion density of BMSCs under direct and indirect contact	113
Figure 3-4: Mass change (ratio of final/initial dry mass M_f/ M_0).....	114
Figure 3-5: Analysis of pH and ionic concentrations in the culture media	116
Figure 3-6: Bacteria density	118
Figure 3-7: Analysis of pH and ionic concentrations in the media.....	121
Figure 3-8: Macroscopic images.....	123
Figure 3-9: Surface morphology and elemental composition.....	125
Figure 3-10: XRD spectra.....	126
Figure 3-11: The degradation properties of materials of interest when they were immerse in r-SBF.....	130

List of Tables

Table 1-1: Results of critical load (L_f) from the micro-scratch testing for the samples of 1.9 A, 1.9 AA, EPD, and A-EPD.....	27
--	----

Introduction

Musculoskeletal diseases and injuries are the leading cause of disabilities in the United States, with an increase proportion of the population from 28.0% in 1996-1998 to 33.2% in 2009-2011.¹ Musculoskeletal diseases and injuries often require biomedical implants and device for clinical treatment. In terms of biomedical implants, implant-associated infections is a key challenge for these devices ². Over 1 million joint prostheses³ and 6 million fracture fixation devices ⁴ are deployed each year, with 2% and 5% of these procedures, developing infections at an economic cost of over 2 billion dollars ⁵. It was estimated that 112,000 orthopaedic implant-associated infections occur annually in the United States, with around 66% of these bacterial infections involving *Staphylococcus* species ⁶. Fracture fixation implants have infection rate ranging from 1% to 2% for closed fractures and rates as high as 30% for open fractures ⁷. The implants could adversely affect the immune system via generating a local immune-compromised environment that inhibits spontaneous clearance of planktonic bacteria by host defense ⁸. Once bacteria adhere on the surface of implant, it could proliferate and form polymeric biofilm that provides significant protection from the host immune system and acts as a diffusion barrier for antibiotics, allowing for bacteria in biofilm to be resistant to antibiotic concentrations 1,000 times higher than that required to kill the same planktonic strain ⁹. Furthermore, bacteria in biofilm that is exposed to subinhibitory antibiotic concentrations could develop antibiotic resistance ¹⁰. The emergence of methicillin-resistant *Staphylococcus aureus* has become a key problem in implant infections. The biofilm formation on surface of implants could further inhibit host cell attachment and tissue integration, which may result in

implant failure¹¹⁻¹². Therefore, current treatment for biomedical implant infections such as aggressive surgical debridement, device removal and long-term antibiotic regimen, are significantly limited¹³. Thus, there is a need for the development of biodegradable, biocompatible implants with antimicrobial properties.

Unlike the conventional non-degradable biomaterials, Magnesium (Mg) is biodegradable in physiological solutions, could achieve a synchronized strength change to the healing bone during the whole healing process, and eliminate the secondary surgery for implant removal. Under slow degradation, the degradation products of Mg are non-toxic to the surrounding tissue because of homeostasis, and will be metabolized and absorbed by the body. Moreover, the similar strength and elastic modulus of Mg to the cortical bone would reduce the stress-shielding effects. The key challenge of Mg as orthopedic implant is that it has a fast degradation rate, which can generate excess hydrogen gas and lose mechanical integrity before complete bone healing.

Either adding alloying elements in Mg or applying surface treatments or both are promising approaches to improve the overall performance of Mg-based bio-metals for clinical applications. The first chapter of this dissertation focus on engineering nanostructured magnesium oxide (MgO) on Mg substrates and investigated the antibacterial properties *in vitro*. By coupling with adding alloying elements, the second chapter of this dissertation focus on engineering nanostructured oxides on Mg alloy pins, to further improve the overall performance of Mg for orthopedic applications. Specifically, nanostructured oxides was produced on the surfaces of Mg-Zn-Ca, Mg-Zn-Sr and pure Mg pins. The degradation, cytocompatibility with bone marrow mesenchymal cells (BMSCs)

and antibacterial properties with methicillin-resistant *staphylococcus aureus* (MRSA) was investigated *in vitro*. The third chapter of this dissertation focus on the developments of nano-micro hydroxyapatite supplemented with gentamicin on Mg rods, and determine their degradation properties, cytocompatibility with BMSCs, antibacterial properties with *Staphylococcus aureus in vitro*.

Chapter 1 Antimicrobial Properties of MgO Nanostructures on Magnesium Substrates

Abstract

Magnesium (Mg) and its alloys have attracted increasing attention in recent years as medical implants for repairing musculoskeletal injuries because of their promising mechanical and biological properties. However, rapid degradation of Mg and its alloys in physiological fluids limited their clinical translation, because the accumulation of hydrogen (H₂) gas and fast release of OH⁻ ions could adversely affect healing process. Moreover, infection is a major concern for internally implanted devices, because it could lead to biofilm formation, prevent host cell attachment on the implants, and interfere osseointegration, resulting in implant failure or other complications. Fabricating nanostructured magnesium oxide (MgO) on magnesium (Mg) substrates is promising in addressing both problems, because it could slow down the degradation process and improve the antimicrobial activity. In this study, nanostructured MgO layers were created on Mg substrates using two different surface treatment techniques, i.e., anodization and electrophoretic deposition (EPD), and cultured with *Staphylococcus aureus* (*S. aureus*) *in vitro* to determine their antimicrobial properties. At the end of 24-h bacterial culture, the nanostructured MgO layers on Mg prepared by anodization or EPD both showed significant bactericidal effect against *S. aureus*. Thus, nanostructured MgO layers on Mg are promising for reducing implant-related infections and complications, and should be further explored for clinical translation toward antimicrobial biodegradable implants.

1.1 Introduction

In recent years, Mg and Mg alloys as bioresorbable metals have attracted increasing attention for orthopedic implant applications due to their promising mechanical and biological properties.¹⁴ Mg is biocompatible and biodegradable.¹⁵ Unlike conventional non-degradable metals, Mg-based implants do not require secondary surgeries for implant removal.¹⁵⁻¹⁶ Mg and Mg alloys have higher elastic modulus and strength than biodegradable polymers and better fracture toughness than ceramics, which are more desirable for load-bearing implants.^{15, 17-20} Mg has a similar modulus to human bone and thus reduce undesirable stress-shielding effect on surrounding bone,^{16, 21-22} which is beneficial for bone health. Recent advances in biodegradable Mg have demonstrated their potential for revolutionizing the treatments for bone fractures.²³⁻²⁵ The screws made of high purity Mg (99.99 wt.% pure) have demonstrated better fracture healing and proper degradation rate when compared with the poly-L-lactide acid (PLLA) screws in the fixation of rabbit femoral intercondylar fractures.²⁶ The high purity Mg screws also showed acceptable mechanical strength and degradation rates compatible with bone formation for fixation of femoral neck fractures in goats.²⁷ Furthermore, the high purity Mg was studied clinically to fix the vascularized bone grafts for human patients with osteonecrosis of the femoral head (ONFH) and showed a higher Harris hip score (HHS) when compared with the controls using vascularized bone grafting alone without screws.²⁸ However, it is difficult and expensive to produce Mg of super high purity (>99.9%).²⁹ The small amount of impurity in commercially 99% to 99.9% pure Mg matrix could lead to rapid degradation and release of excessive hydrogen gas at the early stage of implantation.^{14, 30-31} A previous

study showed that the gas cavities induced subcutaneous emphysema and decreased the survival rate of rats, which remained as the key challenge for clinical translation of Mg-based biometals.³²

Either adding alloying elements into Mg matrix or applying surface treatment on Mg or both are promising approaches to improve the overall performance of Mg-based biometals for clinical applications. For example, the Mg-Ca-Zn alloy screws showed acceptable degradation in the fixation of hand fractures in clinical studies; and the alloy screws were completely replaced by new bone within one year of implantation and the patients regained normal range of grip power.³³ Rare earth (RE) elements have also been added to Mg to reduce the corrosion rate. Mg-RE alloy screws showed proper degradation and osseointegration in treating the patients with mild hallux valgus when compared with the titanium (Ti) screw control.²³ Surface treatment of Mg and Mg alloys has also been explored to further improve their corrosion resistance and surface bioactivity for tissue healing,^{29,34} and even provide antimicrobial properties to reduce infection.

Clinically, implant-associated infections have caused devastating complications, with a reported occurrence rate of 2% to 5% on average.^{5, 35} *Staphylococcus aureus* (*S. aureus*) and *Staphylococcus epidermidis* (*S. epidermidis*) are the major bacteria that account for 70% of orthopedic implant infections.^{6, 36-37} These bacteria could adhere onto implant surfaces, proliferate, and form protective polymeric biofilms that are more difficult to eradicate than planktonic bacteria in the body, even with the treatment of antibiotics. The reason is that biofilms facilitate the resistance against host defense mechanisms, and confer antibiotic resistance because of the slow transportation of antibiotics through the

biofilm matrix.³⁸⁻⁴⁰ Moreover, formation of biofilms on the implants could prevent the attachment of host cells on the implant surface, leading to poor osseointegration and implant failure.¹¹⁻¹² The biofilm dispersal at the late stage of biofilm formation could lead to detachment and spreading of bacteria, causing systemic infections should the bacteria reach the bloodstream.^{12, 41-43} Therefore, preventing implant infections is crucial for improving clinical outcome.

One approach to increase the corrosion resistance of Mg-based metals and disrupt bacteria adhesion is to modify the surface, including surface chemistry and topography. Magnesium oxide (MgO) nanoparticles showed antimicrobial properties against both gram-negative and gram-positive bacteria *in vitro*, including *Escherichia coli* (*E. coli*) and *Staphylococcus aureus* (*S. aureus*).⁴⁴⁻⁴⁷ We found that MgO nanoparticles interact with the gram-negative and gram-positive bacteria differently.⁴⁷ Specifically, the minimum inhibitory concentration (MIC) of MgO nanoparticles was lower for gram-positive bacteria, that is, 0.5 mg/mL for *S. epidermidis* and 0.7 mg/mL for *S. aureus*, but higher for gram-negative bacteria, that is, 1 mg/mL for *E. coli* and *Pseudomonas aeruginosa* (*P. aeruginosa*).⁴⁷ Moreover, when the gram-negative bacteria were cultured with MgO nanoparticles of greater than 1.6 mg/mL, no viable *E. coli* and less than 0.1% *P. aeruginosa* were found. In the cases of gram-positive bacteria, MgO nanoparticles of up to 2.0 mg/mL only showed inhibitory effects on the growth of *S. epidermidis* and *S. aureus*, but did not kill the bacteria completely. Importantly, when MgO nanoparticles were coated onto poly-L-lactic acid (PLLA), the samples showed antimicrobial properties against *S. aureus*, *S. epidermidis* and *P. aeruginosa in vitro*.⁴⁸ In terms of the responses from relevant host cells,

MgO nanoparticles with a low dosage of less than 200 $\mu\text{g}/\text{mL}$ could enhance proliferation of bone marrow derived mesenchymal stem cells (BMSCs) under *in vitro* sequential seeding culture,⁴⁶ which is beneficial for bone regeneration. MgO nanoparticles coated onto poly(methyl methacrylate) (PMMA) and poly-L-lactic acid (PLLA) showed enhanced osteoblast and fibroblast adhesion under *in vitro* culture.⁴⁸⁻⁴⁹ In addition to these desirable bioactivities, applying a dense MgO layer onto Mg substrates could reduce Mg degradation in physiological environment.⁵⁰⁻⁵¹ Mg and its alloys suffer rapid corrosion in humid air (65% relative humidity) and form white, flaky corrosion products of magnesium hydroxide and magnesium oxide.⁵²⁻⁵⁴ However, the natural oxide layers on the surface of Mg are neither as stable nor as protective as the oxide layers that typically form on the aluminum and titanium alloys.⁵⁵ The natural oxide layers formed on Mg are loose and easy to break away, which could accelerate the degradation of Mg. The thickness of these naturally formed oxide layers on Mg is usually in the nanometer scale.⁵⁶⁻⁵⁷

Anodization and electrophoretic deposition (EPD) techniques have been previously established for creating dense MgO nanostructures on Mg substrates under controllable processing parameters.⁵⁰⁻⁵¹ Both anodization and EPD are cost-effective and versatile for producing protective oxide layers with adjustable thickness and surface morphology on various metallic substrates by adjusting the voltage/current, anodization/deposition time, and electrolyte properties (compositions, concentrations, pH, etc.).^{50-51, 58-59} Other methods such as alkaline treatment and plasma electrolytic oxidation (PEO), could also be used to create a layer of MgO or $\text{Mg}(\text{OH})_2$ on Mg. However, surface oxide layers prepared with alkaline treatment is not compact and dense, and PEO process typically requires high

voltage that could create mini-pores in the oxide layers. In both cases, aggressive ions, proteins, and cells in the physiological environment could attack the material surface and jeopardize the corrosion resistance of Mg-based substrates.⁶⁰⁻⁶³ In contrast, dense and compact oxide layers have been created on Mg in our previous studies using anodization and EPD methods with optimized processing parameters of electrolyte compositions, concentrations and anodization/deposition time.^{50, 59, 64-65} The MgO nanostructures on Mg substrates reduced hydrogen (H₂) gas formation during degradation, and showed no adverse effect on bone marrow derived mesenchymal stem cells (BMSCs) *in vitro* under the indirect contact conditions of direct culture.⁵⁰⁻⁵¹ However, the antimicrobial properties of nanostructured MgO on Mg substrates for medical applications have not been investigated. Therefore, the objectives of this study were to investigate and compare the microstructures, elemental compositions, surface and interfacial properties of the nanostructured MgO on Mg substrates prepared by anodization versus EPD, and determine their antimicrobial properties against *S. aureus* using a method adapted from the Japanese Industrial Standard JIS Z 2801:2000 (as shown in Figure 1-1),⁶⁶ and the correlation between the processing, surface properties and the bactericidal effects of the nanostructured MgO layers on Mg substrates. In this study, commercially pure Mg (99.9%) was used as an underlying substrate for developing nanostructured oxide layers using both anodization and EPD methods, to exclude the variability induced by different alloying elements. For example, Mg-Zn-Ca alloys showed greater inhibitory effects on bacterial growth when compared with commercially pure Mg control,⁶⁷ which would induce additional factors affecting bacterial responses. Therefore, commercially pure Mg instead

of Mg alloys was used as the substrate in this study to focus on the effects of nanostructured MgO surface on bacterial interaction.

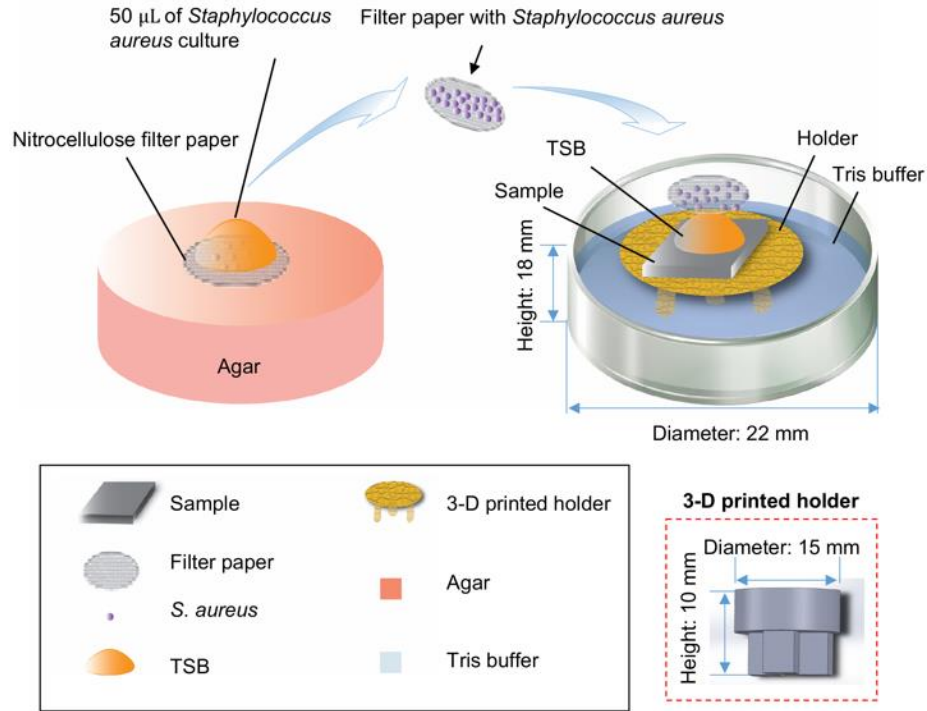


Figure 1-1: Schematic illustration of the methods used to study the antimicrobial properties of the Mg-based samples. The red dash square at the right corner highlights the the three-dimensional printed sample holder and its dimensions. The nitrocellulose filter paper had a diameter to be the same as the width of the samples and fit on top of the square-shaped sample as an inscribed circle to ensure all the bacteria will be in contact with the sample surface.

1.2 Materials and Methods

1.2.1 Anodization and electrophoretic deposition (EPD) process

The methods for creating MgO nanostructures on Mg substrates using anodization⁵⁰ and EPD⁵¹ have been previously established, and adapted for this study as described below with permission from the publishers.⁵⁰⁻⁵¹

1.2.2 Preparation of Mg substrates as electrodes for anodization and EPD

Commercially pure Magnesium sheets (99.9% purity, as-rolled, 1.0 mm thick, Cat# 40604; Alfa Aesar, Ward Hill, MA, USA) were used for this study. The Magnesium sheets were cut into 10 mm x 10 mm squares, connected to the copper wires using copper tapes and embedded in epoxy resin (Cat# ULTRA-3000R-32; Pace Technologies, Tucson, AZ, USA) to ensure that only one surface with a dimension of 10 mm × 10 mm was exposed, as shown in the previous study.⁵⁰ The exposed surface of the embedded Mg was ground with 240, 600, 800 and 1200 grit SiC adhesive paper (Ted Pella Inc. Redding, CA, USA) and polished using the polycrystalline diamond paste of up to 0.25 μm (Physical Test Solutions, Culver City, CA, USA). The well-polished surface of embedded Mg was ultrasonically cleaned in acetone and ethanol for 30 minutes each, before the anodization and EPD processes.

1.2.3 Experimental setup for anodization and EPD

A three-electrode system was used for anodization. The embedded Mg was used as the working electrode (anode), a platinum plate was used as the cathode and Ag/AgCl was used as the reference electrode. The electrodes were connected to a potentiostat (Model 273A; Princeton Applied Research, Oak Ridge, TN, USA) that was controlled by a Powersuite 2.50.0 software (Princeton Applied Research). The distance between the cathode and anode was 1 cm. The working electrode was anodized in a 10 M KOH electrolyte at 1.9 V at room temperature for 2 h. The resulted sample was referred to as 1.9 A, the suffix “A” represents “as-anodized”. As for electrophoretic deposition process, a two-electrode system was used. The embedded Mg was used as the cathode and a platinum

(Pt) plate was used as an anode. The distance between the cathode and anode was 1 cm. The high-power probe sonicator (Model S-4000, Misonix) was used to sonicate 3 mg/mL MgO nanoparticles in anhydrate ethanol in duty cycles of 5 seconds on and 5 seconds off for 5 minutes to avoid agglomeration and ensure a stable homogeneous suspension for the EPD process. The MgO nanoparticles were deposited onto the working electrode of Mg at a voltage of 23 V / cm for 60 seconds at room temperature. The resulted sample was referred to as “EPD”.

1.2.4 Sample annealing after anodization and EPD

The annealing process was the same as described in our previous study.⁵⁰ The samples prepared by anodization or EPD were removed from the epoxy resin using a notcher (No. 100, Whitney Metal Tool Co) and subsequently annealed at 450°C for 6 hours in a tube furnace in an argon atmosphere to convert the Mg(OH)₂ to MgO through a dehydration reaction. During the annealing process, the temperature increased from room temperature to 450°C with a heating rate of 100°C/h to avoid sudden collapse of Mg(OH)₂ crystal structure and was held at 450°C for 6 hours. Afterwards, the tube furnace was turned off to cool down naturally. After annealing, the resulted sample prepared by anodization and EPD was referred to as “1.9 AA” and “A-EPD”, the addition of suffix “A” or prefix “A” represents “annealed”. The anodized samples before annealing was referred to as “1.9 A”, and the samples prepared by EPD before annealing was referred to as “EPD”.

1.2.5 Surface and cross-section characterization

After annealing, the samples were sputter-coated (Model 108, Cressington Scientific Instruments Ltd., Watford, UK) with platinum/palladium at 20 mA with 40 s

sputter time. A scanning electron microscope (SEM; Nova NanoSEM 450, FEI Co., Hillsboro, OR, USA) was used to characterize the surface morphology and cross-sections of the oxide layers on Mg substrates. Energy dispersive X-ray spectroscopy (EDS, X-Max50) and AztecEnergy software (Oxford Instruments, Abingdon, Oxfordshire, UK) was used to analyze the surface elemental composition and distribution. SEM images for the surfaces were taken in the Everhart-Thornley detector (ETD) mode with an acceleration voltage of 20 kV with a working distance of 5 mm and original magnifications of 150x, 10,000x and 40,000x. EDS analysis was performed with an accelerating voltage of 10 kV at an original magnification of 150x. Different acceleration voltages were used for SEM and EDS because more signals from the surface coatings can be detected at a lower acceleration voltage (10 kV), while more signals from the underlying Mg substrates can be detected at a higher acceleration voltage (20 kV). To analyze the cross sections and determine the thickness of the surface-treated Mg after annealing, the samples were cut into half and mounted onto a 90° SEM sample holder, sputter coated under the same conditions as mentioned above, and analyzed using SEM and EDS at an acceleration voltage of 20 kV, a working distance of 5 mm, and an original magnification of 2,000x. The thickness of the MgO layers on Mg substrates was quantified using the ImageJ software.

X-ray diffraction (XRD; Empyrean, PANalytical, Westborough, MA, USA) was used to analyze the phases and crystal structures of the samples. All XRD spectra were acquired using Cu K_{α} radiation (45 kV, 40 mA) at a step size of 0.01° and a dwelling time

of 30 seconds using a PIXcel 1D detector (PANalytical). Phase identification was performed using the HighScore software (PANalytical).

1.2.6 Micro-scratch testing of the nMgO on Mg prepared by anodization and EPD

The interfacial adhesion strength of the prepared samples were evaluated using the Micro-scratch Tester (Nanovea, Irvine, CA) equipped with a sphero-conical stainless steel stylus with an outer diameter (OD) of 1.5 mm. The load on the stainless steel stylus linearly increased from 0 N to 150 N at a normal loading speed of 300 N/min when the stylus was drawn across the surface of coating at a distance of 2 mm. The drawing speed of the stylus was 4 mm/min. After scratching, the coating surface was analyzed under an optical microscope to examine the initial position where the oxide layers delaminated. The normal load and frictional force versus scratch distance were analyzed to determine the critical load (L_f), which is the force at which the initial delamination occurred.

1.2.7 Surface roughness, surface area, and contact angle measurements

The surface topography of 1.9 A, 1.9 AA, EPD and A-EPD samples were characterized using a 3-D laser scanning microscope (VK-X150, Keyence), and the surface roughness (S_q) and surface area (SA) were measured using the MultifileAnalyzer software (VK-H1XME, Keyence) following our previously established method.⁶⁸

The surface wettability of the samples was measured using a contact-angle goniometer (Easydrop; Krüss) in the ambient environment. For the contact angle measurement, 3 μ L of Tryptic Soy Broth (TSB; Fluka Analytical, Sigma-Aldrich) was dropped on the sample surface and the images were taken. The video recordings were saved to the connected computer where the contact angles were analyzed using a drop shape

analyzer (DSA 100, Krüss). The measurements were repeated at three different locations on each sample.

1.2.8 Antimicrobial study with *S. aureus in vitro*

The method used for this *in vitro* antimicrobial study was adapted from the Japanese Industrial Standard JIS Z 2801:2000,⁶⁶ since it has been validated for testing antimicrobial properties of various samples in literature, including surface-treated titanium (Ti) alloys and surface-treated polymer substrates.⁶⁹⁻⁷² As illustrated in Figure 1-1, this *in vitro* method was used to determine the antimicrobial properties of the prepared samples against *S. aureus*. The prepared samples were disinfected under ultraviolet (UV) radiation for 2 hours prior to the bacterial culture. Polished Mg without surface treatment (i.e. without anodization and EPD) and polished titanium (99.99% purity, 1.0 mm thick; Alfa Aesar, USA) were included in the bacterial culture as the controls, and glass was included as a reference. The Mg and titanium controls were ground with 240, 600, 800 and 1200 grit SiC adhesive paper and polished using the polycrystalline diamond paste of up to 0.25 μm . The Mg and titanium controls and glass reference were ultrasonically cleaned in acetone and ethanol for 30 minutes each, followed by disinfection under UV for 2 h. Specific details on the bacterial culture methods were described previously.⁴⁷ Briefly, a portion of frozen stock of *S. aureus* stored at -80°C . was transported to 10 mL of TSB in a 50 mL centrifuge tube using a sterilized loop. The bacteria were cultured in TSB using a shaker incubator (Incusshaker Mini, Benchmark Scientific) at 37°C and 250 rpm for 16 hours. An aliquot of 100 μL of *S. aureus* was added to fresh TSB and cultured for another 4-6 hours. After that, the concentration of bacteria in the working stock was determined using a hemocytometer

(Hausser Bright-Line 3200, Hausser Scientific) and diluted to a concentration of 7.8×10^6 cells/mL in TSB, because this concentration is clinically relevant for orthopedic implant infections.⁷³ To confirm the actual seeding density of *S. aureus*, the working stock was diluted in 10,000 times using Tris(hydroxymethyl)aminomethane buffer (Tris buffer; Acros, Sigma-Aldrich) and 100 μ L of the suspension was plated on the Tryptic soy agar (TSA; Fluka Analytical, Sigma-Aldrich). The agar plates were incubated at 37°C for 24 hours and the colony forming units (CFU) on the agar plates were counted to calculate the actual seeding density. The actual seeding density of *S. aureus* in this study was 6×10^6 CFU/mL, close to the prescribed seeding density. Sterilized nitrocellulose filter papers had a diameter of 1 cm and were placed on a agar plate, and the diluted *S. aureus* of 50 μ L, containing 6×10^6 CFU/mL, was pipette onto the filter papers. TSB was absorbed by the agar and *S. aureus* retained on the filter paper (Figure 1-1). TSB of 50 μ L was pipette onto the center of each sample surface, and the inoculated filter paper was carefully placed on the top of the sample so that the *S. aureus* became in contact with the sample surface. The filter paper with *S. aureus* fit as an inscribed circle on the 1x1 cm square-shaped samples. Each sample with a filter paper on its surface was place on a three-dimensional (3D) printed holder in a well of non-tissue-culture treated plates and incubated at 37°C for 24 hours. Afterward, 1 mL of Tris buffer was added into each well to retain humidity for the 24-hours bacterial incubation. The schematic illustration of the 3D printed sample holder and its dimensions (Diameter: 15 mm, Height: 10 mm) is shown in Figure 1-1. The bacteria only without samples and TSB only without bacteria and samples were incubated as the positive control and blank reference, respectively. After 24 hours, the filter paper on each

sample and the corresponding sample were placed individually into 5 mL of Tris buffer, vortexed for 5 seconds and sonicated for 5 minutes twice to dislodge the adhered bacteria. After that, the Tris buffer containing the bacteria dislodged from the samples or corresponding filter papers was serially diluted and 100 μ L of the diluted and non-diluted suspension was spread onto the Tryptic soy agar plates. The agar plates were incubated in the shaker incubator (without shaking) at 37°C for 24 hours and the colony forming unit (CFU) on each agar plate was counted. The bacterial concentration was determined by measuring the CFUs on agar plates. The bacterial study was run in triplicate for each type of samples.

1.2.9 Bacteria adhesion and morphology after 24-h culture with the samples

After 24 hours of bacterial culture, one sample from each group was washed 3 times with Tris buffer and transferred to a new well plate. Free bacteria that did not attach onto the sample were washed away. After the third wash, the bacteria on the sample were fixed with 10% glutaraldehyde for 1 h. The 10% glutaraldehyde was diluted previously from a 25% glutaraldehyde solution (Sigma Life Sciences, Sigma Aldrich) in Tris buffer. After 1 h, each sample was rinsed 3 times with Tris buffer to remove any glutaraldehyde residue, dehydrated using 30%, 75% and 100% ethanol for 30 minutes each, and then air-dried at room temperature for 24 hours. The dried samples were sputter coated with Pt/Pd using a sputter coater (108 Auto Sputter Coater, Cressington Scientific) at 20 mA for 45 seconds, prior to the SEM imaging. Representative images were taken using the same SEM described above, with a secondary electron detector at an accelerating voltage of 10 kV, a working distance of 5 mm, and original magnifications of 150x and 5,000x. The surface

elemental composition of the samples after bacterial culture was analyzed using EDS at an accelerating voltage of 10 kV and an original magnification of 150x. The phases and crystal structures of the samples after bacterial culture were analyzed using the same XRD as described in section 2.2, with PIXcel 1D detector at a step size of 0.01° and a dwelling time of 30 seconds. Phase identification was performed using the HighScore software.

1.2.10 Statistical analyses

All numerical data in this study were obtained from experiments run in triplicate. The numerical data were examined using one-way analysis of variance (ANOVA) followed by a Turkey test, when the data sets fulfilled the parametric criteria (i.e., data normality was over 0.5). Statistical significance was considered at $p < 0.05$ for Turkey test. For non-parametric data (i.e., data normality was less than 0.5), the data sets were examined using Kruskal-Wallis analyses followed by a Dunn test and adjusted by Hochberg's method. Statistical significance was considered at $p < 0.025$ for Dunn test.

1.3 Results

1.3.1 Surface microstructures and elemental compositions

Figure 1-2 shows the surface characterization for the samples prepared by anodization before annealing (labeled as 1.9 A), by anodization after annealing (labeled as 1.9 AA), by EPD before annealing (labeled as EPD), and by EPD after annealing (labeled as A-EPD). The images from scanning electron microscopy (SEM) in Figure 1-2a at the original magnifications of 150x (first column), 10,000x (second column), 40,000x (inset in the second column) show the representative nano-to-micron surface features for each

sample. The overlay of SEM images and energy dispersive X-ray spectroscopy (EDS) maps at the original magnification of 150x are shown in the third column. The SEM images at the low magnification of 150x confirmed the homogeneous surface morphology of the 1.9 A sample. At the high magnification of 40,000, nanoscale crystal structure was observed in the anodized layer of the 1.9 A sample. After annealing, microcracks appeared on the 1.9 AA sample, with the crack width of $0.193 \pm 0.145 \mu\text{m}$ based on the measurement for the SEM images taken at an original magnification of 10,000x.

The SEM images at the low magnification of 150x confirmed the homogeneous surface morphology of the EPD sample. At the high magnification of 40,000x, nanoscale particles were observed in the coating layer of the EPD sample. After annealing, the SEM images of A-EPD sample at 150x show that the MgO nanoparticles tended to fuse along the polishing line on Mg and the size of the particles became larger when compared with that before annealing (EPD). The high-magnification SEM image shows that the nMgO coating became more compact and dense after the annealing process (A-EPD) when compared with the coating surface before annealing (EPD).

The overlaid SEM images and EDS maps in the third column in Figure 1-2a show homogenous elemental distribution of Mg and O. The EDS results are shown in Figure 1-2b. The atomic ratio of O/Mg for the 1.9 A sample is 1.9, which indicated that the composition of the anodized Mg sample is $\text{Mg}(\text{OH})_2$. The EDS results of the 1.9 AA sample show the atomic ratio of 1.2, indicating $\text{Mg}(\text{OH})_2$ converted to MgO after annealing. The EDS results in Figure 1-2b show the presence of Mg and O elements for

the EPD and A-EPD samples; the sample prepared by EPD had a stoichiometry O/Mg atomic ratio of 0.3 before annealing (EPD) and 1.1 after annealing.

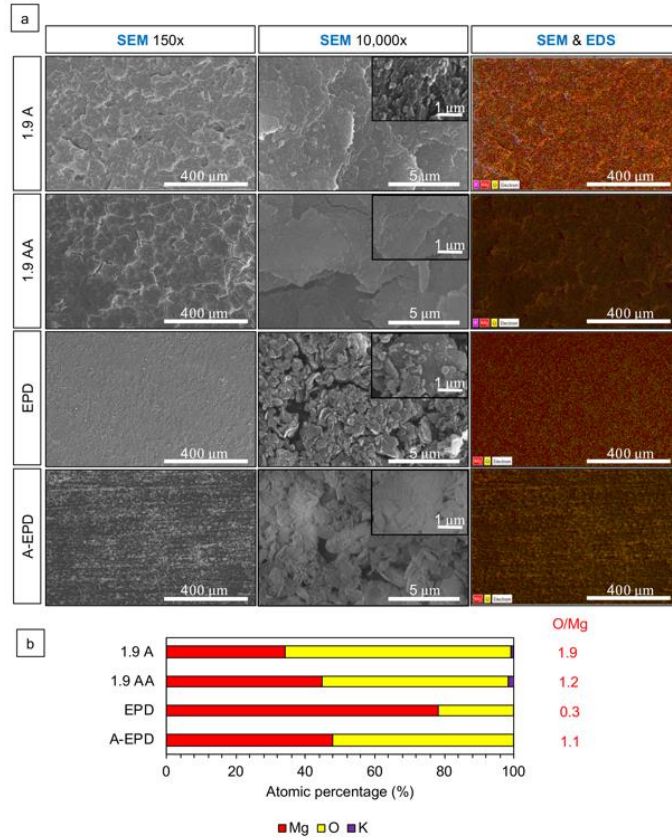


Figure 1-2: Characterization of surface microstructure and composition for the surface-treated Mg samples. (a) SEM images of anodized Mg substrates prepared by anodization at 1.9 V vs. Ag/AgCl in 10 M KOH at room temperature for 2 h before and after annealing (1.9 A and 1.9 AA respectively), and nMgO-coated Mg substrates prepared by EPD in ethanol at a concentration of 3 mg/mL before and after annealing (EPD and A-EPD respectively). SEM images were obtained at the original magnifications of 150x (the first column), 10,000x (the second column), and 40,000x (insets in the second column), showing nano-to-micron scale surface microstructures on each sample. The third column shows the overlaid SEM images and EDS maps at the original magnification of 150x. Scale bar = 400 μm for all SEM images at an original magnification of 150x. Scale bar = 5 μm for all SEM images at an original magnification of 10,000x. Scale bar = 1 μm for all SEM images at an original magnification of 40,000x. (b) The corresponding surface elemental composition (at.%) quantified by EDS area analyses. The EDS analyses were obtained from the SEM images at an original magnification of 150x. The atomic ratio of O/Mg (at.%/at.%) listed next to the EDS graph was calculated based on the corresponding EDS data.

1.3.2 Phase identification in the surface-treated Mg samples and Mg control

The crystalline phases in the surface-treated Mg samples and Mg control were characterized using X-ray diffraction (XRD), as shown in Figure 1-3. The XRD spectra of the 1.9 A sample shows the presence of Mg, MgO and Mg(OH)₂ phases. After annealing, the peak for Mg(OH)₂ disappeared and the 1.9 AA sample shows the presence of Mg and MgO in the XRD spectra, which confirmed the dehydration of Mg(OH)₂. The XRD spectra of the EPD and A-EPD show the presence of Mg and MgO phases with very small peaks of Mg(OH)₂. The XRD spectra of the Mg control shows the presence of Mg peaks.

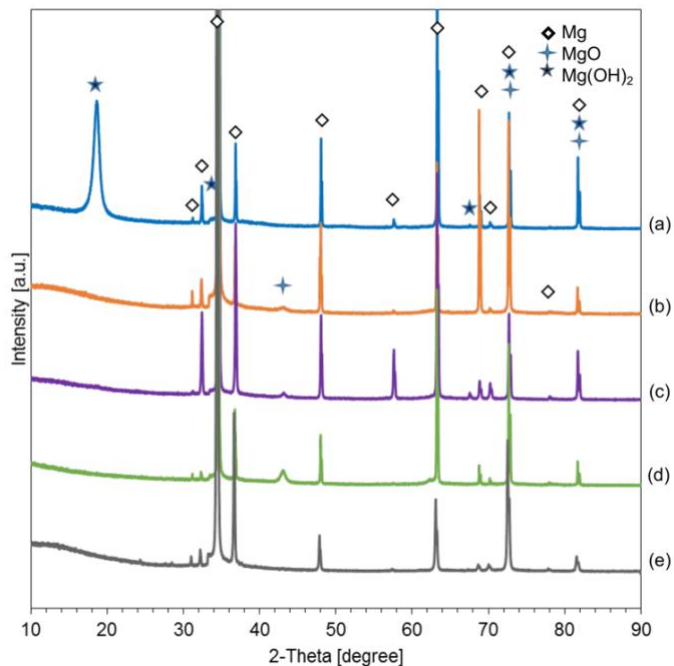


Figure 1-3: X-ray diffraction (XRD) patterns of the surface-treated Mg samples and Mg control. (a) anodized Mg (1.9 A); (b) annealed-anodized Mg (1.9 AA); (c) Mg with electrophoretically deposited MgO nanoparticles (EPD); (d) Mg with electrophoretically deposited MgO nanoparticles and annealed (A-EPD); and (e) Mg control. Phases were identified based on Mg (ICSD pattern 01-071-3765), MgO (ICSD pattern 00-030-0794), and Mg(OH)₂ (ICSD pattern 00-050-1085) standards.

1.3.3 Cross-sectional analysis of the samples prepared by anodization and EPD

Figure 1-4 shows the cross-sectional characterization of the samples of 1.9 A, 1.9 AA, EPD and A-EPD using SEM and EDS at an original magnification of 2,000x and the corresponding EDS maps of elemental distribution for Mg and O. The overlay SEM images and EDS maps were used to identify the interface between the oxide layers and Mg substrates for measuring the oxide layer thickness. The thickness of oxide layers on Mg substrates were $4.078 \pm 0.423 \mu\text{m}$ and $8.764 \pm 1.222 \mu\text{m}$ for 1.9 A and 1.9 AA, respectively. The surface layers for EPD and A-EPD had a thickness of $4.398 \pm 0.869 \mu\text{m}$ and $11.109 \pm 0.397 \mu\text{m}$, respectively.

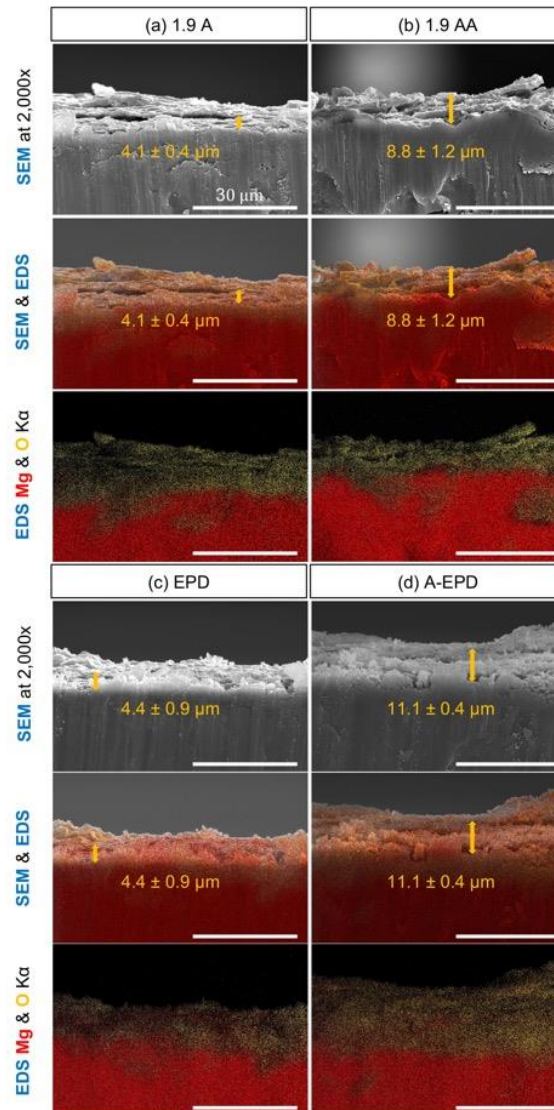


Figure 1-4: Cross-sectional characterization of the surface-treated Mg samples by SEM and EDS. Montage of SEM images, overlaid SEM images and EDS maps of O (yellow), Mg (red) and K (blue), as well as the corresponding overlaid EDS maps (K_{α} line) for elemental distribution of O and Mg. (a) anodized Mg (1.9 A); (b) annealed-anodized Mg (1.9 AA); (c) Mg with electrophoretically deposited MgO nanoparticles (EPD); and (d) Mg with electrophoretically deposited MgO nanoparticles and annealed (A-EPD). SEM images were obtained at an original magnification of 2,000x. Scale bar = 30 μm for all SEM images and EDS maps. The average thickness of the oxide layers on Mg substrates was labeled in the SEM images, overlaid SEM images and EDS maps of O (yellow), Mg (red) and K (blue), as denoted using the double side arrows and values of mean \pm SD.

1.3.4 Interfacial adhesion strength of the surface oxide layers to Mg substrates

Progressive loading from 0 N to 150 N was applied on the surface of samples prepared by anodization (1.9 A and 1.9 AA) over a distance of 2 mm, whereas progressive load from 0 N to 3 N was applied on the surface of samples prepared by EPD (EPD and A-EPD) over a distance of 2 mm, because the interfacial adhesion strengths of the anodized samples (1.9 A and 1.9 AA) are expected to be higher. The loading rate was 5 N/s and the moving speed was 4 mm/min. Figure 1-5 shows the normal load and friction force versus the scratch distance. The critical loads L_f at the failure points of the surface layers during the micro-scratch test are summarized in Table 1-1. The critical load is the smallest load at which a recognizable failure of the coating occurs. As observed from the microscopic images for all the samples, the initial mark on the surface layers appeared at the beginning of the test. The failure load of the top layers of the 1.9 A and 1.9 AA were much higher than that of the EPD and A-EPD samples because no delamination occurred between the surface layers and the underlying Mg substrates until the progressive load reached the maximum load of 150 N, as shown in the microscopic images in Figure 1-5. As the stylus continued to penetrate into the surface layer prepared by EPD before annealing (EPD), failure of the top layer occurred at 0.55 mm with a load of 0.39 N. For the surface layer prepared by EPD after annealing (A-EPD), failure of the top layer occurred at 0.97 mm with a load of 1.63 N.

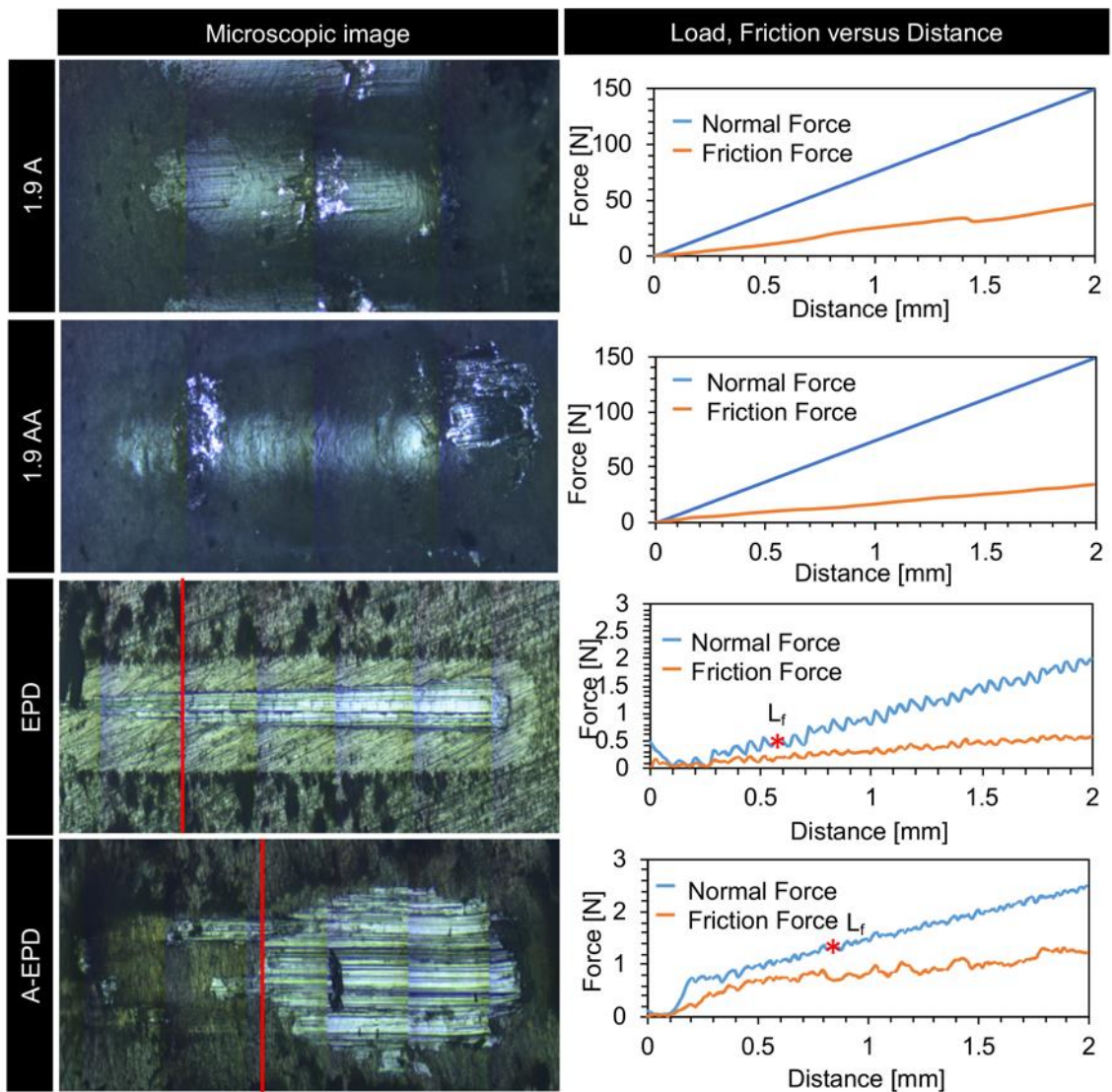


Figure 1-5: Micro-scratch testing for interfacial adhesion strength between the MgO surface layers and Mg substrates. Left column: optical micrographs of the surface after scratch testing. Right column: the results of load, friction force versus distance for the samples of anodized Mg (1.9 A), annealed-anodized Mg (1.9 AA), Mg with electrophoretically deposited MgO nanoparticles (EPD), Mg with electrophoretically deposited MgO nanoparticles and annealed (A-EPD).

Table 1-1: Results of critical load (L_f) from the micro-scratch testing for the samples of 1.9 A, 1.9 AA, EPD, and A-EPD.

Samples	1.9 A	1.9 AA	EPD	A-EPD
L_f [N]	>150	>150	0.17 ± 0.18	1.56 ± 0.07

1.3.5 Surface roughness, surface area, and wettability of the oxide layers on Mg substrates

Figure 1-6 (a, b, c, d) show the 3D surface topography, surface roughness and surface area of the 1.9 A, 1.9 AA, EPD and A-EPD samples. The respective surface roughness (S_q) of the 1.9 A, 1.9 AA, EPD and A-EPD samples were $3.7 \pm 0.1 \mu\text{m}$, $4.3 \pm 0.1 \mu\text{m}$, $1.2 \pm 0.1 \mu\text{m}$ and $1.2 \pm 0.1 \mu\text{m}$. The surface roughness was analyzed using one-way ANOVA because the data sets were parametric. One-way ANOVA confirmed a significantly higher surface roughness of 1.9 AA sample than the 1.9 A sample, but the difference was not considered important because it was so small and around the resolution of the microscope optics. The surface roughness of 1.9 A and 1.9 AA samples were significantly higher than the EPD and A-EPD samples. The respective surface area (SA) of the 1.9 A, 1.9 AA, EPD and A-EPD samples were $6.0 \pm 0.1 \text{ mm}^2$, $7.5 \pm 0.1 \text{ mm}^2$, $2.8 \pm 0.1 \text{ mm}^2$ and $2.6 \pm 0.2 \text{ mm}^2$. The surface area was analyzed using one-way ANOVA because the data sets were parametric. One-way ANOVA confirmed a significantly higher surface area of 1.9 AA sample than the 1.9 A sample. The surface areas of 1.9 A and 1.9 AA samples were significantly higher than the EPD and A-EPD samples.

The surface wettability of each specimen was analyzed using the static contact angle measurements. TSB was used as the liquid droplets on surface because it was used

as culture media for *S. aureus* in the bacterial study. The contact angles of the samples and controls are summarized in Figure 1-6e, including their corresponding microscopic images acquired during the contact angle measurements. The contact angles of the 1.9 A, 1.9 AA, EPD, A-EPD, Mg, Ti controls and glass reference were $50.6^{\circ} \pm 1.3^{\circ}$, $82.9^{\circ} \pm 3.8^{\circ}$, $9.4^{\circ} \pm 3.8^{\circ}$, $35.0^{\circ} \pm 3.8^{\circ}$, $50.3^{\circ} \pm 5.6^{\circ}$, $55.6^{\circ} \pm 3.7^{\circ}$ and $52.0^{\circ} \pm 4.7^{\circ}$, respectively. The contact angle values were analyzed using one-way ANOVA because the data sets were parametric. The statistical analysis confirmed that the contact angles of the 1.9 A and 1.9 AA samples were significantly higher than that of the EPD and A-EPD samples. The contact angle of 1.9 AA sample was significantly higher than the 1.9 A sample. The contact angle of A-EPD sample was significantly higher than the EPD sample. The contact angle of 1.9 AA sample was significantly higher than the Mg, Ti controls and glass reference. The contact angles of the EPD and A-EPD samples were significantly lower than the Mg, Ti controls and glass reference. The contact angles of all the samples were less than 90° , indicating the surfaces were hydrophilic.⁷⁴

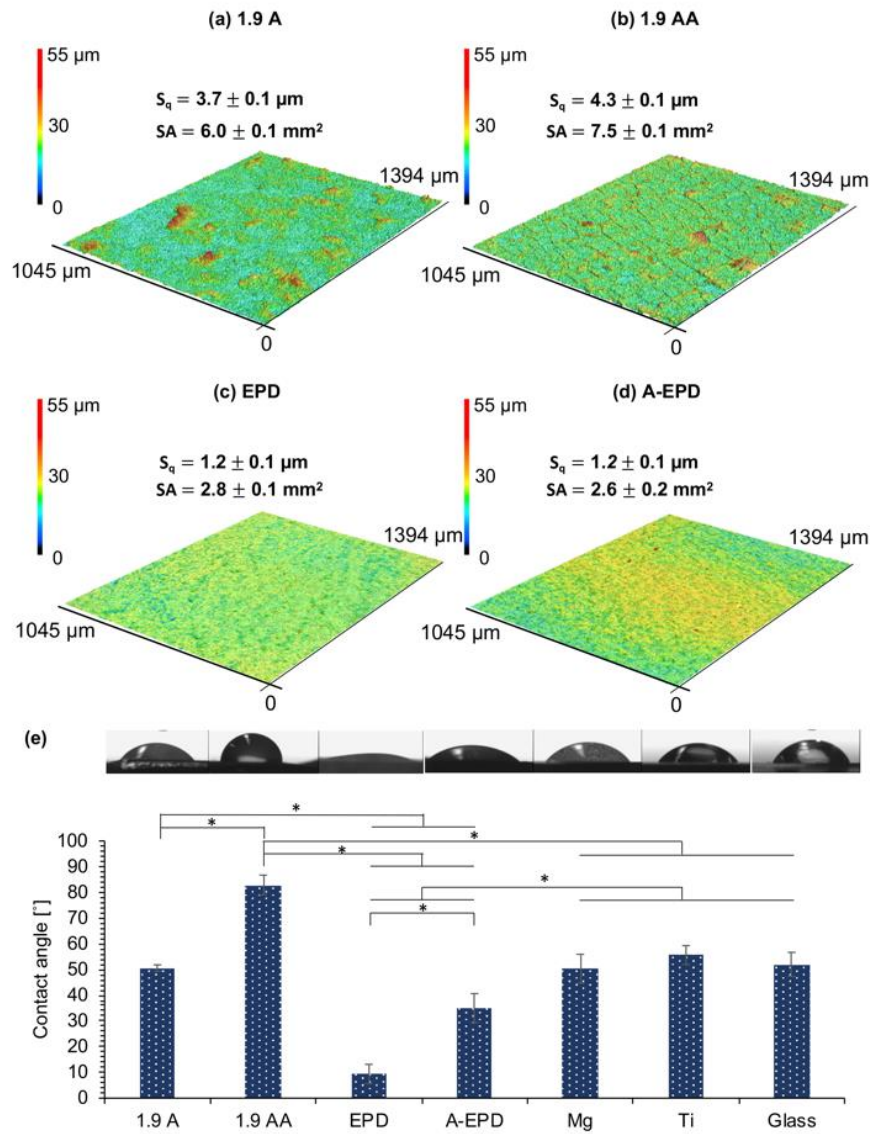


Figure 1-6: Surface topography, surface roughness, surface area and contact angle measurements for the surface-treated Mg samples of 1.9 A, 1.9 AA, EPD, and A-EPD. (a,b,c,d) Surface topography maps from 3D laser scanning, and the calculated surface roughness and surface area for (a)1.9 A, (b) 1.9 AA, (c) EPD, and (d) A-EPD samples. The scanning area was $1045 \mu\text{m} \times 1394 \mu\text{m}$. (e) contact angle measurements for 1.9 A, 1.9 AA, EPD, and A-EPD samples, controls of Mg and Ti, and glass references. TSB droplets were used for the contact angle measurements on all samples. The corresponding droplet micrographs were shown on the top of the contact angle data. Values are mean \pm standard deviation; $n=3$. * $p < 0.05$.

1.3.6 Viability of *S. aureus* after 24 hours of culture with the samples

Bacterial viability was quantified on both the sample surfaces and the filter papers that covered the sample surfaces, by counting the colony forming units (CFU) on the agar plates, as shown in Figure 1-7. No viable *S. aureus* was detected on 1.9 A, 1.9 AA, EPD and their corresponding filter papers, and very few bacteria were found on A-EPD and the corresponding filter paper after 24 hours of culture.

For the bacterial viability on the sample surfaces, ANOVA confirmed that the CFU of *S. aureus* cultured with the 1.9 A and 1.9 AA samples were significantly lower when compared with that cultured with Ti control and glass reference. The CFU of *S. aureus* cultured with the EPD sample was significantly lower when compared with that cultured with Mg, Ti controls and glass reference. The CFU of *S. aureus* cultured with the A-EPD sample was significantly higher when compared with that cultured with the EPD sample, but was significantly lower when compared with that of Mg, Ti controls and glass reference. ANOVA also confirmed a significantly lower CFU of *S. aureus* for Mg control when compared with the Ti control.

For the viability of bacteria from the filter paper that covered the sample surfaces, ANOVA confirmed a significantly lower CFU of *S. aureus* on the filter paper cultured with the 1.9 A and 1.9 AA samples when compared with that cultured with the A-EPD sample, Mg, Ti controls and glass reference. The CFU of *S. aureus* on the filter paper cultured with the EPD sample was significantly lower when compared with that of Mg, Ti controls and glass reference. The CFU of *S. aureus* on the filter paper cultured with the A-EPD sample was significantly higher when compared with that of the EPD sample, but was significantly

lower when compared with that of Mg, Ti controls and glass reference. ANOVA also confirmed a significantly lower CFU of *S. aureus* on the filter paper for the Mg control when compared with the Ti control and glass reference.

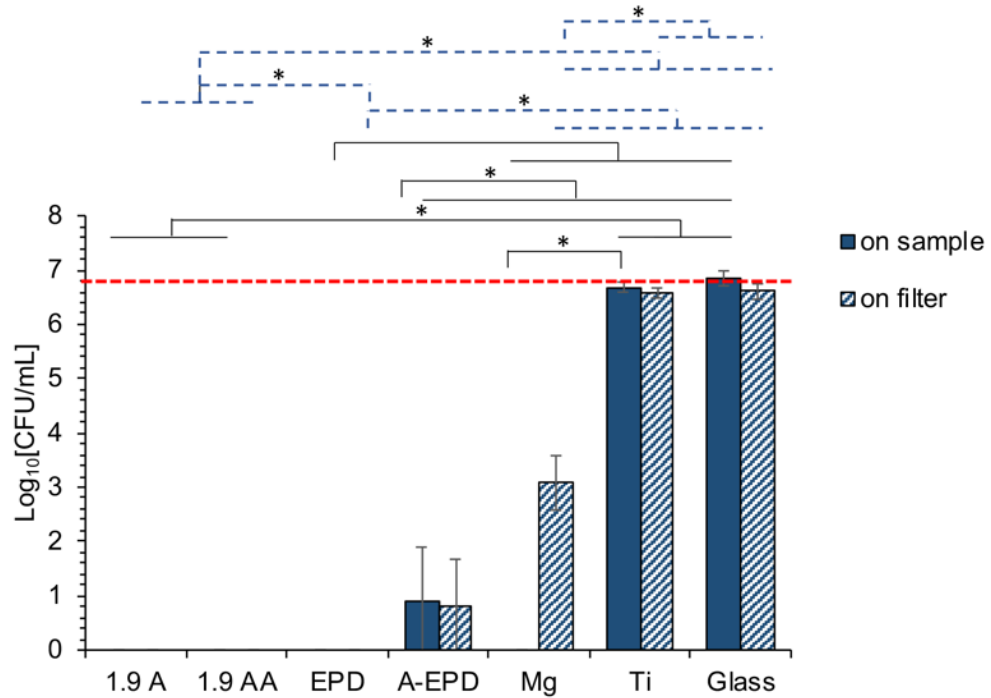


Figure 1-7: Bacterial density after being cultured in TSB with the surface-treated Mg samples of 1.9 A, 1.9 AA, EPD, and A-EPD, as well as the controls of Mg and Ti, and the glass references for 24 hours, as quantified from colony forming unit (CFU). Bacteria were seeded at an actual concentration of 6×10^6 CFU/mL, as indicated by the red dashed line. Values are mean \pm standard deviation; n=9. *p < 0.05. Black solid line indicated the statistical analysis results for the bacterial density on the sample surfaces. Blue dashed line indicated the statistical analysis results for the bacterial density on the filters covered the sample surfaces.

1.3.7 Adhesion and morphology of *S. aureus* after 24 hours of culture with the samples

SEM images were taken after 24 hours of culture with the samples, controls and references with *S. aureus*, as shown in Figure 1-8. No *S. aureus* was found on the surfaces of the 1.9 A, 1.9 AA, EPD and A-EPD samples. Few *S. aureus* was observed on their corresponding filter papers, and the morphology of *S. aureus* on the filter papers that cultured with the 1.9 A, 1.9 AA, EPD and A-EPD samples was distorted with observable damage in the cell wall and cell membrane, in contrast to the typical round morphology of *S. aureus* as seen in the Ti control and glass reference. The bacteria on the surfaces of Ti control and glass reference aggregated with an appearance of biofilm, which was also found on their corresponding filter papers. No bacteria were found on the surface of the Mg control, but some *S. aureus* aggregated on the filter paper that cultured with the Mg control.

The SEM images at an original magnification of 150x and 40,000x (insets) in Figure 1-8a also show the surface morphology of the samples and controls at the end of 24-h culture. At low magnification of 150x, corrosion-induced microcracks propagated along the surfaces of the 1.9 A, 1.9 AA and A-EPD samples, with crack widths of $1.502 \pm 0.641 \mu\text{m}$, $2.312 \pm 1.139 \mu\text{m}$, and $0.406 \pm 0.062 \mu\text{m}$, respectively, based on the measurements on their responding SEM images at the original magnifications of 150x. The surface morphology of the EPD sample was very similar to that of the Mg control, indicates that some MgO coating might have delaminated from the Mg substrate during the bacterial culture. At the high magnification of 40,000x, distinct nano-scale features were observed

on the 1.9 A, 1.9 AA, EPD and A-EPD samples, and corrosion-induced micro-cracks penetrated through the EPD sample. The nanostructures of platelet-like morphology were observed on the Mg control at the magnification of 40,000x (inset) and considered to be the MgO/Mg(OH)₂ degradation products.

Figure 1-8b summarizes the elemental composition (in at.%) quantified from the EDS analyses at an original magnification of 150x. Mg, O, C, and P were found on the surfaces of 1.9 A, 1.9 AA and A-EPD samples after culture with *S. aureus* in TSB. Mg, O, C, P and trace amount of Cl were found on the surfaces of the samples of EPD after culture with *S. aureus* in TSB. Specifically, the surfaces of the 1.9 AA, EPD and A-EPD samples had a higher weight percent of C and O when compared with the Mg control. In contrast to the surface of the Mg control where only Mg, O and C elements appeared, the surfaces of 1.9 A, 1.9 AA, EPD and A-EPD show small amounts of P, indicating phosphorus-containing minerals deposition.

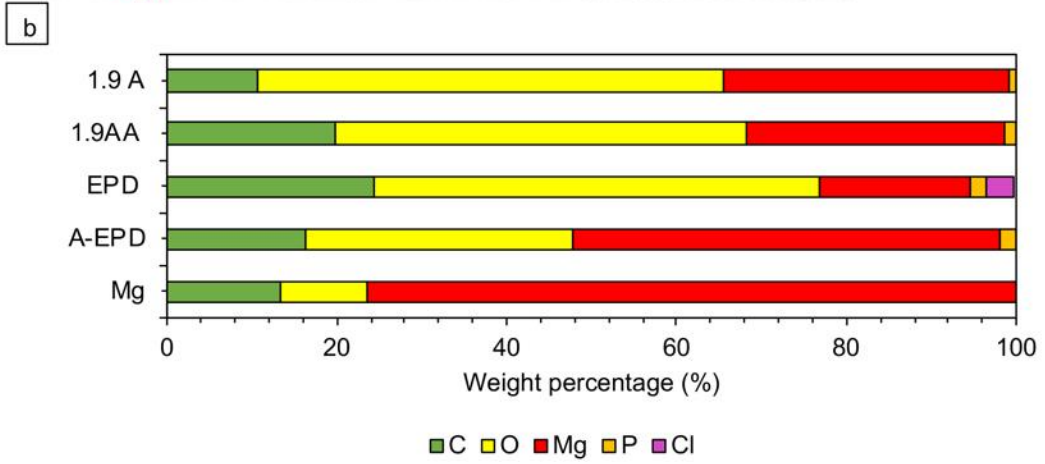
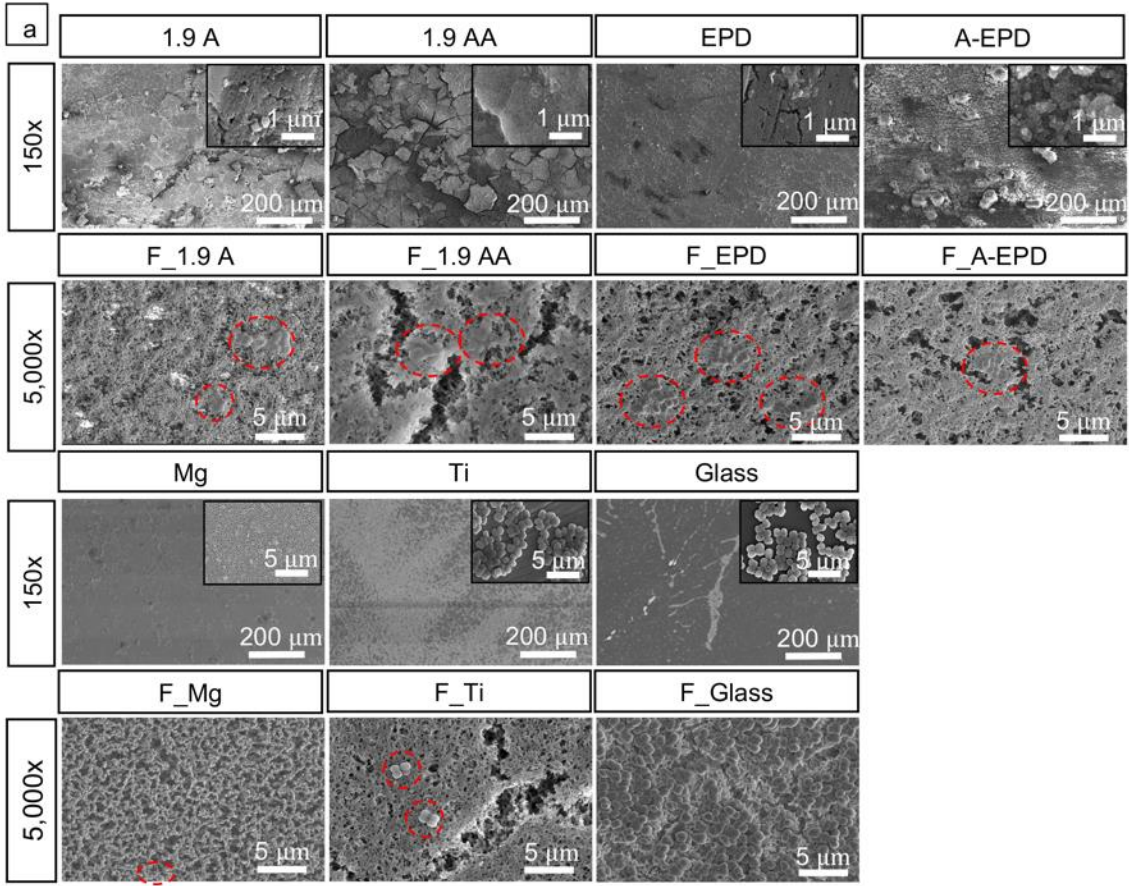


Figure 1-8: Characterization of surface microstructure and composition after 24-h of bacterial culture. (a) SEM images of the 1.9 A, 1.9 AA, EPD, A-EPD, Mg, Ti, Glass and the respective nitrocellular filter papers (with F as prefix in abbreviation) on each sample after bacterial culture. The abbreviations of F_1.9 A, F_1.9 AA, F_EPD, F_A-EPD, F_Mg, F_Ti, F_Glass refer to the filters on the corresponding samples. SEM images of the samples were obtained at an original magnification of 150x and 40,000x (the inset SEM images), showing nano-to-micron scale surface features for each sample after bacterial culture. SEM images of the respective nitrocellular filter papers were obtained at an original magnification of 5,000x. Scale bar = 200 μm for all SEM images at an original magnification of 150x. Scale bar = 5 μm for all SEM images at an original magnification of 5,000x. Scale bar = 1 μm for all SEM images at an original magnification of 40,000x. The red dashed circles on the SEM images highlight the adhered *S. aureus* on the surfaces of different samples. (b) Surface elemental compositions (at%) of the 1.9 A, 1.9 AA, EPD, A-EPD, and Mg samples were quantified by EDS area analyses and plotted in the bar graph. The EDS analyses were performed on the SEM images at an original magnification of 150x.

Figure 1-9 shows the XRD spectra for the 1.9 A, 1.9 AA, EPD, A-EPD samples and Mg control after 24-h culture with *S. aureus* in TSB. The phases were identified based on the standards in the Inorganic Crystal Structure Database (ICSD); specifically, 01-071-3765 for Mg, 00-030-0794 for MgO, 00-050-1085 for Mg(OH)₂ and 01-086-2348 for MgCO₃. The XRD spectra confirmed the newly formed compound MgCO₃ and the presence of MgO and Mg(OH)₂ on the surfaces of 1.9 A, 1.9 AA, EPD, and A-EPD samples and Mg control, which was in agreement with the EDS analyses. The nanostructured degradation products on Mg control were most likely to be MgO/Mg(OH)₂ considering the platelet-like morphology as shown in the SEM images in Figure 1-8, detection of MgO, Mg(OH)₂ and MgCO₃ phases in the XRD spectra in Figure 1-9, and other reports in literature.^{50, 75-76} In this study, the Mg peaks are much more intense than the other peaks because the surface coating layers were only around a few micrometers, in which the conventional XRD detected the signals from both the coatings and the substrates, producing relatively weak signals from the thin surface layers and intense signals from the Mg substrates. Similarly, for the thin degradation layers after bacterial culture, the peaks for phosphorus-containing compound may be too small to be detected, but it was actually in the degradation layers, since the presence of P was detected in the EDS results.

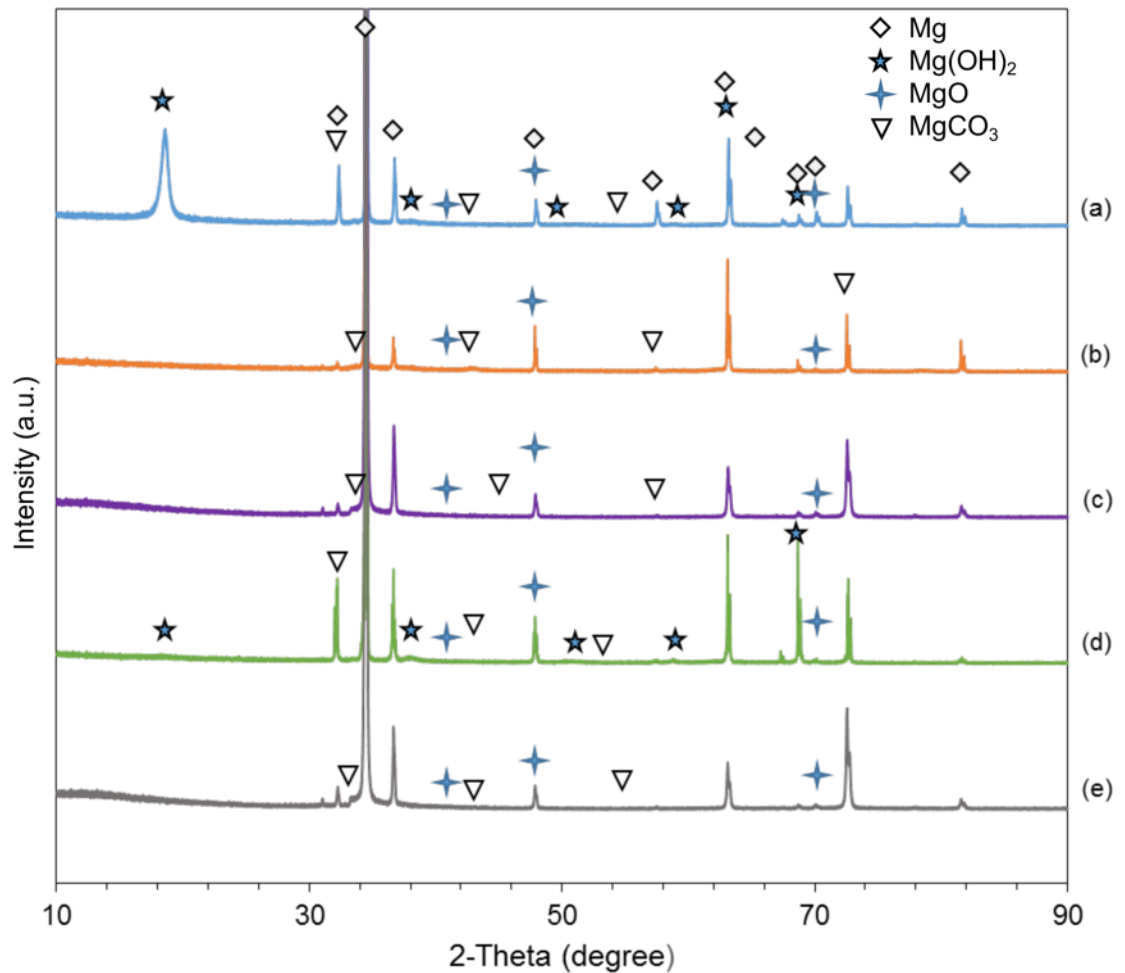


Figure 1-9: X-ray diffraction patterns of the surface-treated Mg samples and Mg control after 24-h bacterial culture. (a) anodized Mg (1.9 A); (b) annealed-anodized Mg (1.9 AA); (c) Mg with electrophoretically deposited MgO nanoparticles (EPD); (d) Mg with electrophoretically deposited MgO nanoparticles and annealed (A-EPD); and (e) Mg. Phases were identified based on Mg (ICSD pattern 01-071-3765), MgO (ICSD pattern 00-030-0794), Mg(OH)₂ (ICSD pattern 00-050-1085), and MgCO₃ (ICSD pattern 01-086-2348) standards.

1.4 Discussion

1.4.1 Comparison of nanostructured MgO on Mg prepared by anodization and EPD

Different surface treatment techniques could produce surface layers of various thickness on Mg substrates with different microstructures, surface properties (i.e., surface

roughness, surface area and surface wettability), and interfacial adhesion strength. Thus, it is essential to compare the oxide layers on Mg substrates prepared using anodization versus EPD, for determining the relationships between the processing conditions and the corresponding microstructure, oxide layer thickness, surface properties, and interfacial adhesion strength.

Anodization involves electrochemical reactions to create oxide layers on the surfaces of the working electrodes under certain applied current and voltage.⁵⁰ In contrast, during the EPD process, the charged particles suspended in the electrolyte accumulate on the working electrode under the applied electric field, without chemical reactions. Therefore, the characteristics of oxide layers formed on Mg by anodization or EPD would be different. As shown in Figure 1-2a, a homogenous, compact Mg(OH)₂ layer formed on Mg via anodization, while small pores between particulates were visible in the MgO layer produced by EPD. The surface roughness of the 1.9 AA samples in this study ($S_q = 4.3 \pm 0.1 \mu\text{m}$), was deemed to be close to the samples in a previous report ($S_q = 3.0 \pm 0.5 \mu\text{m}$),⁵⁰ considering the standard deviation and the resolution of the microscope optics. In comparison with the oxide layers produced by EPD, the surface roughness of oxide layers produced by anodization was significantly higher, likely because of finer Mg(OH)₂/MgO nanostructures of the 1.9 A and 1.9 AA samples, as shown in the SEM images in Figure 1-2. Rougher surfaces of 1.9 A and 1.9 AA samples exhibited significantly larger surface area than EPD and A-EPD samples. According to the Wenzel model of liquid on solid surfaces, chemically hydrophilic surface should become more hydrophilic if surface roughness increased.⁷⁷ This contradicted our findings on the surface roughness and

wettability, likely because of the differences in surface microstructure and elemental composition produced via these two different surface treatment techniques.

After anodization, annealing at 450°C in argon (Ar) dehydrated the Mg(OH)₂ phase and converted the Mg(OH)₂ phase into MgO phase, as shown in the XRD spectra in Figure 1-3. For the specimens prepared by anodization, the change of Mg/O atomic ratio from 1:1.9 before annealing to 1:1.2 after annealing in Figure 1-2b EDS analyses, also supported the chemical conversion of the oxide layers from Mg(OH)₂ to MgO through dehydration.⁷⁵ The conversion from Mg(OH)₂ to MgO during the annealing process resulted in microstructural shrinkage and thus formation of micro-cracks throughout the oxide layer, mainly because decomposition of Mg(OH)₂ resulted in pseudomorphous transformation of each single platelet and the newly formed MgO had a smaller size.⁷⁸ In contrast, for the EPD samples, XRD confirmed the oxide layers were mainly composed of MgO, with a small amount of Mg(OH)₂. The atomic ratio between the Mg and O was 1:0.3 before annealing, indicating the oxide layer on Mg contained some pores, which allowed the detection of more signals from the underlying Mg substrate. However, the annealing process fused and consolidated the MgO nanoparticles to a dense and compact oxide layer on Mg substrate (Figure 1-2), which resulted in an atomic ratio between the Mg and O to be 1:1.1, close to 1:1. Even though no significant difference in surface roughness was detected between EPD and A-EPD samples, the oxide layer produced by EPD became less hydrophilic after annealing. Moreover, the annealing process increased the thickness of the oxide layers for the specimens prepared by anodization and EPD; specifically, from 4.078 ± 0.423 μm for 1.9 A to 8.764 ± 1.222 μm for 1.9 AA, and from 4.398 ± 0.869 μm for EPD

to $11.109 \pm 0.397 \mu\text{m}$ for A-EPD. Cipriano et al.⁵⁰ and Cortez Alcaraz et al.⁵¹ reported the thickness for 1.9 A, 1.9 AA and A-EPD samples were $2.34 \pm 0.53 \mu\text{m}$, $21.8 \pm 8.9 \mu\text{m}$, $10.1 \pm 0.3 \mu\text{m}$, respectively. The thickness of the oxide layers in this study was considered to be similar to the previous reports within the range of standard deviation.⁵⁰⁻⁵¹ In some case, it was reported that the protection provided by the coating layer was proportional to the coating thickness.⁵⁹ In other case, the corrosion resistance provided by the MgO layers on Mg strongly depended on the combination of surface morphology, surface roughness, surface area, surface wettability and thickness of MgO.⁷⁹⁻⁸⁰ Our previous results showed that MgO layers prepared by both anodization and EPD affected the degradation mode and rate of Mg after 9-day immersion in revised simulated body fluid (r-SBF) and Dulbecco's modified Eagle's medium (DMEM); that is, such oxide layers resulted in more homogenous degradation mode and reduced initial H₂ gas release when compared with non-coated Mg controls.⁵⁰⁻⁵¹

In addition to the surface properties and thickness of the oxide layers, the interfacial adhesion strength between the oxide layer and the underlying Mg substrates is an important parameter to consider for medical implant applications, because any delamination of the surface layers during *in vivo* implantation could release particulate debris and thus cause adverse effects on the surrounding tissue and implant performance.⁸¹ Clearly, the anodization process could provide superior interfacial adhesion strength between the MgO layers and the underlying Mg substrates due to the presence of chemical bonding at the interface.⁸² In this study, the oxide layers created by anodization did not show delamination on the surface even after micro-scratch testing at a critical load L_f higher than

150 N. The critical load from the micro-scratch testing indicates the cohesive (bonding within the coating layers) and adhesive (bonding of a coating to the substrate) strength of a coating.⁸³ The higher the critical load the stronger the interfacial adhesion strength. For the MgO layers on Mg created via anodization, the applied voltage should be lower than the value at which water dissociates, to achieve a compact layer onto Mg. When the anodization voltage is higher than the voltage for water decomposition, oxygen evolution occurs instead of thickening the oxide layers.¹⁹ When the anodization voltage is higher than the dielectric break-down voltage, usually up to 300 V,⁸⁴ or higher up to 500 V,⁸⁵ the process is called PEO or micro arc oxidation (MAO), where a plasma is generated while the oxide layer grows. The PEO/MAO process would produce craters with sizes of a few microns due to the electric currents locally breaking through the growing layer.¹⁹ Therefore, it is interesting to compare the interfacial adhesion strength of the oxide layers prepared by different processes, such as MAO/PEO, anodization and EPD. Durdu et al. developed oxide coatings on Mg using micro arc oxidation (MAO) at different current densities, with the critical load ranging from 58 to 84 N when the coating thicknesses ranged from 25 to 40 μm .⁸⁶ Aktug et al. reported a critical load of 98 N and 109 N for the plasma electrolytic oxide (PEO) coatings on AZ31 Mg alloy in the solution of KOH and two different concentration of sodium metasilicate pentahydrate ($\text{Na}_2\text{SiO}_3 \cdot 5\text{H}_2\text{O}$) electrolytes with the coating thickness of 73.3 and 67.6 μm . Mandelli et al. found a critical load from 15 N to 22 N for the anodic oxides or oxide/saline composite coatings with or without addition of nanoparticles (TiO_2 , ZrO_2 and Al_2O_3) on AM60B Mg alloy prepared by micro-arc anodic oxidation (MAO) with the thickness of 5 to 18 μm .⁸⁷ Overall, the

anodized oxide layers on Mg prepared in this study showed a significantly higher interfacial adhesion strength when compared with other reports in literatures.⁸⁶⁻⁸⁸ However, under an external shear force, the oxide layers on Mg prepared by EPD would be damaged more easily than the samples prepared by anodization, because the interfacial adhesion strength of the EPD samples were at least 100 times less than the anodized samples.

1.4.2 Antimicrobial properties of nanostructured MgO on Mg prepared by anodization and EPD

The bacterial culture was carried out using a method modified from the JIS Z 2801 standard to simulate the situation of an infection that could occur in the primary surgery.⁶⁹ In the bacterial culture, we increased the volume of bacterial suspension to 50 μL instead of 20 μL or 36 μL described in the standard and literature,^{69, 71} because 50 μL was the maximum volume that the sample of 10 mm x 10 mm can hold on the top surface. Moreover, we added 1 mL of Tris buffer into each well of culture plates to retain moisture in the well during 24-h incubation. The bacteria density adhered on the samples and their corresponding filter papers was analyzed by counting the CFUs after 24-h bacterial culture. The method of plating and counting CFUs is well-accepted in microbiology for determining the bacterial viability.

Mg has been previously reported to reduce the growth of *S. aureus* when compared with the bacterial control and 316 stainless steel intramedullary pins (316LLS) *in vitro*.⁸⁹ In this study, no viable *S. aureus* was found on the surface of Mg. However, *S. aureus* on the filter paper on Mg still remained viable at a level of 10^3 CFU/mL, which was 0.02% of bacterial seeding density. In contrast, the anodized Mg with a nanostructured MgO layer

on the surface or the Mg coated with MgO nanoparticles by EPD, killed all *S. aureus* on the sample surfaces and on the filter papers on the samples at the end of 24-h culture *in vitro*, indicating a greater potency against bacterial adhesion than non-treated metallic Mg surface. Despite the difference in surface morphology and surface roughness of the nanostructured oxide layers prepared by anodization and EPD, they showed similar inhibitory effect on bacterial growth, probably because they were all hydrophilic and shared similar chemical compositions. Moreover, although the thicknesses of the nanostructured MgO layers on Mg prepared by anodization and EPD were different, they all showed similar bactericidal effects against *S. aureus*.

The kinetic studies on the antibacterial effects of the MgO microparticles and nanoparticles against *E. coli* and *S. epidermidis* have been reported previously.⁹⁰⁻⁹¹ For example, the death rate constant of the *E. coli* increased linearly in the 0- 80 minutes of incubation with 1.25 mg/mL to 20 mg/mL of MgO microparticles at the temperature of 37°C.⁹⁰ When *S. epidermidis* was exposed to 0.2 mg/mL MgO nanoparticles, the bacterial growth was inhibited when compared with the bacteria-only control based on their optical density (OD) readings, and the growth kinetics of *S. epidermidis* showed that the bacterial growth was delayed for a few hours initially and afterwards partially inhibited when compared with the bacteria-only control in the 0-12 hours of incubation.**Error! Hyperlink reference not valid.** However, the antibacterial kinetics of MgO nanoparticles or coatings against *S. aureus* has not been reported yet. For the future studies, we recommend further kinetics analysis of the antibacterial effect of the nMgO-coated Mg in the 0-24 hours of incubation time or longer if there were viable bacteria remaining.

1.4.3 Factors affecting the viability and morphology of *S. aureus*

The factors influencing bacterial adhesion on implant surfaces include surface chemistry, surface charge, surface roughness, surface area, and hydrophilicity.⁹² In this study, we mainly investigated the correlation between the surface properties of the biomaterials, such as, surface chemistry, surface roughness/area, hydrophilicity, and their antimicrobial properties. MgO nanoparticles have shown antibacterial effects against both gram-positive bacteria, i.e., *S. aureus*, *S. epidermidis* and methicillin-resistant *Staphylococcus aureus* (MRSA) and gram-negative bacteria, i.e., *E. coli* and *P. aeruginosa*.⁴⁶⁻⁴⁷ However, based on the previous study on *S. epidermidis*, a gram-positive bacterium, the increases of broth pH up to 10 or Mg²⁺ concentrations up to 50 mM were not the main factors contributing to antimicrobial properties of MgO nanoparticles.⁴⁷

One proposed mechanism could be the contact between MgO and the bacteria caused damage to the cell wall/membrane, leading to leakage of the internal minerals, proteins and genetic materials.^{46-47, 93} For the gram-positive bacteria, the positively charged MgO nanoparticles may interact with the negatively charged phosphate groups, or trapped in the peptidoglycan layer of the bacteria, which may inhibit their growth.⁴⁷

The oxidative stress and the produced intracellular reactive oxygen species (ROS) were also considered to be critical for the antibacterial activities of nanomaterials. Recently, Das et al. proved that the antibacterial effects of nanostructured MgO was ROS dependent based on the peroxide (H₂O₂) detection.⁹⁴ Some bacteria such as *S. aureus* that undergo aerobic respiration also generate superoxide dismutase (SOD) to neutralize the ROS. If more ROS were produced and not timely neutralized by the SOD, the excess ROS

could cause damage to the bacteria.⁹⁵⁻⁹⁷ The ROS generation is dependent on physicochemical properties of the nanomaterials, i.e., particle size, shape, surface area, chemical composition, degree of agglomerations, and the testing systems, i.e., bacterial types.⁹⁸⁻⁹⁹ Among the physicochemical properties, the particle size, surface area and chemical composition are the key factors for the production of ROS.⁹⁸ The decrease of particle size will lead to an increase of surface area, because particle size and surface area are related. As the surface area increases, the number of active sites at which ROS generation can take place would increase.⁹⁸ In this study, the surface area of the nanostructured MgO layer produced using anodization is larger than that produced using the EPD method, as shown in Figure 1-6. Therefore, we speculated that the nanostructured MgO layer produced using anodization could generate higher amount of ROS than the EPD method. Moreover, when the MgO nanoparticles inhibit the growth of the bacteria, it may disrupt the quorum sensing among the bacteria because of the reduction in the number of bacteria in the culture suspension.⁴⁷ Previous studies in the literature^{47, 100-102} revealed that quorum sensing could affect bacterial properties such as virulence factors and the ability of bacteria to communicate to each other, inhibiting their activities and functions. Therefore, in our *in vitro* culture model of this study, the close contact of the bacteria with the nanostructured MgO might strengthen the interactions between nanostructured MgO and the bacterial wall/membrane, or increase the local ROS generated by the nanostructured MgO, thus killing the nearby bacteria within 24 hours.

Surface roughness of biomaterials is another relevant factor that affects bacterial adhesion. Rougher surfaces at the micrometer scale normally promote bacterial adhesion

due to the increased surface area that provides more sites for bacterial colonization.⁹² In our previous study, the surface roughness of Mg control was $0.113 \pm 0.006 \mu\text{m}$,⁵⁰ which was significantly lower than the oxide layers produced by anodization and EPD. In this study, the rougher oxide surfaces produced via anodization and EPD showed better inhibitory effects on the growth of *S. aureus* when compared with the smoother non-treated surface of Mg control. This could be due to the synergic effect of surface chemistry, surface roughness and area, and hydrophilicity. The higher surface roughness and larger surface area of the oxide layers formed via anodization and EPD could lead to the increased presence of MgO nanostructures on the surface for disrupting bacterial activities.

Apart from surface chemistry and surface roughness of the implants, surface hydrophilicity also plays a significant role in biomaterial-bacterium interactions.⁷⁴ Thermodynamic theory suggested that the adhesion of *S. aureus* and *S. epidermidis* favored hydrophobicity of the biomaterial surface, which is considered to be the main driving force for general bacterial adhesion. Mackintosh et al. found that the adhesion of *S. epidermidis* after cultured with polyethylene terephthalate (PET) in phosphate-buffered saline for 24 hours was lower on the PET samples with hydrophilic modification when compared with the unmodified control and the other modified surfaces.¹⁰³ However, when the samples were incubated in serum *in vitro*, the hydrophilic, hydrophobic and control surfaces all showed low bacteria adhesion.¹⁰³ One of the main reasons for the difference among these studies is that the protein absorption on biomaterials could alter their surface properties. Bare biomaterials would be coated with proteins from blood and interstitial fluids within nanoseconds when implanted.⁴² Surface hydrophilicity could influence the bonding

strength, conformation and orientation of proteins adhered to the surfaces, and composition of the macromolecular layer formed on the surfaces via selective adhesion from the biological fluid.¹⁰⁴⁻¹⁰⁵ Therefore, the surface properties of biomaterials that affect protein adhesion and conformation could thus influence bacterial adhesion. In this study, the samples prepared by anodization and EPD before and after annealing, are all hydrophilic, coupled with their surface chemistry, roughness and nanostructures, could contribute to the observed antibacterial effect *in vitro*.

We believe that MgO nanostructures created on Mg-based metals should have bactericidal or inhibitory effect against many types of pathogenic microbes, such as gram-positive bacteria (*S. aureus*, *S. epidermidis* and *MRSA*), gram-negative bacteria (*E. coli* and *P. aeruginosa*), and infectious yeasts [drug-sensitive *Candida albicans* (*C. albicans*), fluconazole resistant *Candida albicans* (*C. albicans FR*), drug-sensitive *Candida glabrata* (*C. glabrata*) and echinocandin resistant *Candida glabrata* (*C. glabrata ER*)], on the basis that MgO nanoparticles had a broad antimicrobial spectrum against all these microbes.⁴⁶⁻⁴⁷ In the future studies, it is still necessary to test all these microbes with the nanostructured MgO on Mg substrates to determine the full-spectrum antimicrobial properties, because microbial interactions with the nano-MgO surface on Mg substrates may differ from MgO nanoparticles even though they both share the same chemistry of MgO.

1.4.4 Mg with nanostructured MgO surface layer for biomedical applications

The cytocompatibility and degradation performance of nanostructured MgO on Mg substrates prepared by anodization or EPD have been separately reported in our previous studies.⁵⁰⁻⁵¹ The specimens from both anodization and EPD have shown lower H₂ gas

release than the polished bare Mg, and no adverse effects on BMSCs under indirect contact conditions of *in vitro* direct culture.⁵⁰⁻⁵¹ The significance of this study was to elucidate the relationships between the two different processing methods and the resulted differences in surface properties for the first time. Specifically, we investigated and compared the surface properties including microstructures, surface roughness and area, surface wettability, and interfacial adhesion strength of the surface oxide layers on the Mg substrates prepared by anodization versus EPD. Moreover, in this study, we discussed the correlation between the surface properties and the bactericidal effects of the prepared samples and first reported the synergic effects of surface chemistry of nanostructured MgO, surface roughness and surface area, and hydrophilicity of the prepared samples on reducing bacterial adhesion and growth. This study confirmed the critical hypothesis regarding bactericidal properties of the nanostructured oxide layers on pure Mg. The killing effect of the surface-treated Mg by anodization and EPD against *S. aureus* is very promising for preventing severe infections and associated complications in medical implants, especially in the cases of trauma surgeries for open wound. Moreover, the nanostructured MgO on Mg prepared using the anodization method showed much stronger interfacial adhesion strength than the EPD method, thus more favorable for medical implant applications.

Remarkable progress has been made in the developments of Mg-based biomaterials and clinical translation in recent years, especially Mg-RE alloys. The clinical application of MgYREZr screw has first been reported in Germany for treatments of mild hallux valgus, demonstrating better biocompatibility and osteoconductive properties when compared with Ti screws.²³ More recently, MgYREZr screw was used in the fixation of

distal fibular fractures and intra-articular fractures in clinical case studies, and the results have shown complete fracture healing and free range of motion in the patients.²⁴⁻²⁵ To further optimize the collective properties of Mg-based implants including degradation properties, biocompatibility, bioactivity, and antimicrobial properties, our methodology for developing nanostructured oxide layers could be applied on the Mg-RE alloys or any other kinds of Mg alloys.

The collective properties of the surface-treated Mg by anodization and EPD in cytocompatibility, degradation performance, and antimicrobial activities are promising for biomedical implant applications. The mechanisms for the bactericidal properties of the developed MgO nanostructures on Mg were mainly discussed based on literatures. Further experiments will be needed to determine the specific contributions of the proposed mechanisms, such as bacterial membrane damage, ROS generation, and quorum sensing disruption caused by MgO surface chemistry, surface roughness and surface area, and wettability. Moreover, the performance of the nanostructured MgO on Mg requires further studies *in vivo*, because the different conditions *in vivo* such as high shear stress in different anatomical sites could influence bacterial behaviors, e.g., the rates of horizontal gene transfer and mutations.⁴² Therefore, it is necessary to perform *in vivo* studies in a functional animal model with infection for the nanostructured MgO on Mg-based metals toward clinical translation.

1.5 Conclusions

This article reported the surface morphology, elemental composition, crystalline phases, surface roughness, surface area, surface wettability, interfacial adhesion strength

between the surface oxide layers and underlying Mg substrates, and antimicrobial properties of nanostructured MgO on Mg prepared by respective anodization and EPD processes, that is, 1.9 A, 1.9 AA, EPD and A-EPD samples. The anodized Mg samples of 1.9 A and 1.9 AA showed superior interfacial adhesion strength between the MgO surface layers and the underlying Mg substrates than the samples prepared by EPD and A-EPD processes. The strong interfacial adhesion of the nanostructured MgO surface layer to the underlying Mg substrate could lead to better performance in clinical applications, including improved biocompatibility, corrosion resistance and antibacterial activity, for the 1.9 A and 1.9 AA samples, during *in vivo* implantation. The *in vitro* bacterial study of the surface-treated Mg against *S. aureus* showed impressive bactericidal effects, indicating a great potential in reducing device-associated infections in many clinical areas. The mechanisms of bactericidal effects could be related to the surface chemistry coupled with the surface roughness, surface area and hydrophilicity, which enhanced the functions of the ROS generated by the MgO nanostructures, and the interactions between MgO nanostructures and bacterial wall/membrane. Further studies are needed to elucidate the exact mechanisms. In the future, it is necessary to perform *in vivo* studies in an infected animal model for validation of nanostructured MgO on Mg-based metals for reducing infection while promoting healing.

Chapter 2 *In Vitro* Degradation, Cytocompatibility, and Antimicrobial Properties of
Nanostructured Oxides on Magnesium Alloys

Abstract

This article reported the optimal parameters of anodization to create homogeneous nanostructured oxide layers on magnesium (Mg)-2 wt% zinc (Zn)-0.5 wt% calcium (Ca) (designated as ZC21), Mg-4 wt% Zn-1 wt% strontium (Sr) (designated as ZSr41), and pure Mg pins. The microstructure, crystallized phases, surface roughness/area and electrochemical corrosion behavior were studied. The surface-treated ZC21 prepared at 1.9 V, surface-treated ZSr41 prepared at 1.8 V and surface-treated pure Mg prepared at 1.8 V showed significantly lower corrosion current densities in revised simulated body fluid (r-SBF), and reduced adhesion of MRSA on their surfaces *in vitro*. The soluble degradation products released from the surface-treated ZC21, ZSr41 and pure Mg did not affect the cells under indirect contact, but showed reduced cell spreading and adhesion at the cell-biomaterial interfaces when compared with Ti with same geometry and glass with flat surface, probably because of the change of surface topography and compositions at the dynamic interfaces. This in-depth systematic study has demonstrated the potential of anodized ZC21, ZSr41 and Mg pins for biomedical applications, and should be further studied *in vivo* toward clinical translations.

2.1 Introduction

Conventional inert metallic materials such as titanium, stainless steel and cobalt alloys for fracture fixation devices has caused several complications, i.e., stress-shielding induced weakening of bone and secondary removal of the implants.¹⁸ In 2010, it was found that a total of 180,000 additional surgeries were performed to remove permanent fixation devices in Germany, making it the fourth most commonly performed surgical procedures following fracture fixation, arthroscopies and intervertebral disk interventions in orthopedic surgery.¹⁰⁶ Recent advances in biodegradable Magnesium (Mg) implants demonstrated the potential to revolutionize the treatments of bone fractures and heart diseases due to its excellent biodegradability, biocompatibility and mechanical properties. Mg is the fourth most abundant element in human body and involved in hundreds of biochemical reactions and serves as a key element in the construction of bone and soft tissue.¹⁰⁷ The excessive Mg ions released from the degradation of Mg-based biomaterials can be transported via the circulatory system and excreted by way of urine and feces, without causing any adverse effects.¹⁰⁸ It was found that the hydroxide ions (OH⁻) that cause the alkaline condition adjacent to the Mg screws implanted into the femoral shaft of rabbits could be quickly neutralized according to the in-situ measurement using a micro-pH sensor.¹⁰⁹ However, the hydrogen (H₂) gas released from the degradation of Mg-based biomaterials could form gas bubbles in the peri-implant tissue if the degradation rate of the Mg-based implant is fast, which may cause health risks in patients.¹¹⁰⁻¹¹¹ Therefore, it is necessary to control the degradation rate of Mg-based implants to reduce H₂ accumulation. Moreover, for orthopedic applications, implant infections still are a significant clinical

problem, with current treatment limited to surgical debridement, device removal and long-term systematic antibiotic regimens. However, the long-term antibiotic treatment can lead to the development of opportunistic infections and antibiotic resistance.¹¹²⁻¹¹³

Adding alloying elements into pure Mg or surface treatments are two possible ways to improve the overall performance of Mg-based biomaterials for orthopedic applications. The most common alloying elements utilized in Mg-based biomaterials are calcium (Ca), zinc (Zn), manganese (Mn), tin (Sn) and silver (Ag).¹¹⁴ Recent developments of Mg-Zn-Ca alloy has shown that the addition of Zn and Ca could improve the mechanical strength and corrosion resistance because of grain refinements and solid solution strengthening.¹¹⁵ Zn is one of the most essential elements in human body and beneficial for improving the corrosion potential and reduce the degradation rate of Mg.^{16, 116-117} The addition of 1 – 4 wt% Zn in the Mg matrix significantly increased the mechanical properties, i.e., ultimate tensile strength and elongation.¹¹⁸ Excessive addition of Zn in the Mg matrix could lead to severe micro-galvanic corrosion of Mg alloys.¹⁶ The overall performance of Mg-Zn alloys with low Zn content can be further modified by adding the Ca element. Ca is the most abundant elements in the human body and present in the hydroxyapatite in the skeleton in the form of Ca^{2+} . However, The MgCa alloy with a concentration of Ca higher than 1.34 wt% could generate Mg_2Ca to induce micro-galvanic couples that could accelerate corrosion.¹¹⁹ In our previous study, the as-cast the Mg-2 wt% Zn- 0.5 wt% Ca (named ZC21) alloy showed the best overall performance among four Mg-xZn-0.5 wt% Ca (x = 0.5 wt%, 1.0 wt%, 2.0 wt% and 4.0 wt%) alloys, including slower degradation rate and improved cytocompatibility in direct exposure culture with BMSCs *in vitro*.¹¹⁵ Moreover,

the ZC21 alloy has shown significantly higher BMSC adhesion and better antimicrobial properties *in vitro*, and slower degradation in a mouse femoral defect model when compared with the Mg-4 wt% Zn-1 wt% strontium (named ZSr41) alloy and Mg control.⁶⁷ Similar to that of Ca, the proper addition of strontium (Sr) could further improve the corrosion resistance and mechanical properties of Mg-Zn alloys. Sr is a natural element in bones and can promote the osteoid formation and bone growth.¹²⁰ The processing, microstructure, composition, mechanical properties, *in vitro* degradation properties, cytocompatibility and inflammatory response of the Mg-4 wt% Zn-xSr (x = 0.15, 0.5, 1, 1.5 wt%) were studied previously.¹²¹⁻¹²⁴ Mg-4 wt% Zn-1 wt% Sr (named ZSr41) had the optimal overall performance among the four different Mg-Zn-Sr alloys. Furthermore, in our previous study, the ZSr41 intramedullary pins showed a significant net bone growth through intramedullary implantation in the proximal tibia of rat for 47 days.¹⁴ However, the ZSr41 intramedullary pins showed a significantly higher degradation rate than the Mg control when implanted in the rat tibia.¹⁴ As alloying of Mg is challenging because of low solubilities of many elements and the contents and types of some alloying elements in Mg should be strictly controlled to ensure biosafety in human body,¹²⁵ surface treatments for Mg alloys become a very attractive way to improve their corrosion resistance and cellular interactions.

The corrosion resistance, cytocompatibility and antimicrobial properties of the ZC21 and ZSr41 alloys could be further improved by creating a nanostructured MgO layer on their surfaces. MgO nanoparticles with a lower concentration of less than 200 $\mu\text{g/mL}$ could enhance the proliferation of BMSCs *in vitro*.⁴⁶ In addition, applying a dense MgO

layer onto the Mg alloys could reduce the degradation rate in the physiological environment.⁴⁸⁻⁴⁹ Our previous study found that applying a dense nanostructured MgO layer on pure Mg substrate using anodization inhibited the growth of *Staphylococcus aureus* (*S. aureus*) and reduced H₂ during the 9-day immersion study in both revised simulated body fluid (r-SBF) and Dulbecco's modified Eagle's medium (DMEM) *in vitro*.^{50, 126} Additionally, the soluble degradation products released from the anodized Mg did not have adverse effects on the adhesion and morphology of the surrounding bone marrow derived mesenchymal stem cells (BMSCs) in direct culture *in vitro*.⁵⁰ However, no report was found so far for developing nanostructured MgO layers onto ZC21 and ZSr41 alloy pins using anodization.

The objectives of this study was to engineer nanostructured MgO layers on ZC21, ZSr41 and Mg pins using anodization and determine the effects of processing parameters on their surface microstructure and properties, corrosion properties, and *in vitro* degradation and biological properties. Specifically, first, we adapted the previously established anodization process and studied the effect of the applied voltages on their surface characteristics. Second, we investigated the *in vitro* degradation of the anodized ZC21, ZSr41 and Mg using electrochemical methods. Third, we comprehensively studied the degradation, cytocompatibility with BMSCs and antimicrobial properties against methicillin-resistant *Staphylococcus aureus* (MRSA) of the anodized ZC21, ZSr41 and Mg pins *in vitro*. To our knowledge, this is the first in-depth systematic study to report and compare the degradation properties, cytocompatibility and antibacterial properties of the anodized ZC21, ZSr41 and pure Mg *in vitro*.

2.2 Materials and Methods

2.2.1 Anodization of the ZC21, ZSr41 and Mg pins

2.2.1.1 Preparation of ZC21, ZSr41 and Mg pins

The ZC21 alloy with a nominal composition of 2.0 wt.% Zn and 0.5 wt.% Ca in the Mg matrix and the ZSr41 with a nominal composition of 4.0 wt.% Zn and 1 wt.% Sr in the Mg matrix were prepared based on the methods as described in our previous publications.^{14, 67} Briefly, the ZC21 and ZSr41 alloy intramedullary pins were produced via melting, casting, extrusion and drawing. A crucible made of stainless steel was preheated in an electrical-resistance furnace (Shenyang General Furnace Manufacturing Co., Ltd) from room temperature to 400-500°C, under an argon (Ar) gas-protected environment to avoid oxidation. The commercially pure Mg ingots (99.94 wt.%; Boyu, Shenyang, China) were then melted in the preheated stainless steel crucible at 700-730°C. In terms of ZC21 alloy, bulk pure Zn (99.5 wt.%; Boyu, Shenyang, China) and Mg-15Ca alloy (Boyu, Shenyang, China) were added to the molten Mg, stirred and heated at a temperature of 750°C for 20 mins in the electrical-resistance furnace. For ZSr41 alloy, bulk pure Zn (99.5 wt.%; Boyu, Shenyang, China) and Mg-20 wt.% Sr alloy (Boyu, Shenyang, China) were added to the molten Mg, stirred and heated at a temperature of 750°C for 30 mins in the electrical-resistance furnace. The molten mixture was then degassed with hexachloroethane and deslagged, casted at 720°C in a cone-shaped cast iron mold, and cooled down in the air. The as-cast ZC21 and ZSr41 alloy ingots were machined to rods with a diameter of 40 mm and homogenized at 450°C for 6 h. The rods with a diameter of 40 mm was then hot-extruded with an extrusion ration of 10:1 using a four-column

hydraulic press (300 tons; Shandong Machinery Factory) to produce ZC21 rods with a diameter of 4 mm. Finally, the 4 mm ZC21 and ZSr41 rods were drawn into a wires with a diameter of 1 mm through multiple passes, heat treatment was applied at 300°C between each drawing pass. Pure Mg wires (99.94 wt.%; Boyu, Shenyang, China) with a diameter of 1 mm was produced using the same source of Mg and the same metallurgical processes (melting, casting, extrusion and drawing) with same processing parameters as for producing the ZC21 and ZSr41 alloy wires.

The pure Mg wires was used as a control in this study. As-drawn titanium (Ti)-6 wt.% aluminum (Al)-4 wt.% vanadium (V) alloy wires with the same diameter of 1 mm was used as a non-degradable control in the *in vitro* bacteria and cell culture studies, and *in vivo* studies. Before the surface treatment, *in vitro* and *in vivo* studies, the ZC21 alloy, ZSr41 alloy, Mg and Ti wires were cut into pins with length of 7 mm to fit into the femoral defects created in the animal model. The ZC21, ZSr41, Mg and Ti pins were ground using 600, 800 and 1200 grit SiC paper (Ted Pella, USA), and ultrasonically cleaned in 100% acetone (Sigma-Aldrich, USA) and 100% ethanol (200 proof; Koptec) for 15 mins, respectively, using sonication bath (Symphony, VWR), and air dried before the anodization process.

2.2.1.2 Experimental set-up for anodization

A three-electrode system was used for anodization. The ZC21/ZSr41/Mg intramedullary pin was used as a working electrode (anode), a platinum plate was used as a cathode and Ag/AgCl was used as a reference electrode. The electrodes were connected to a potentiostat (Model 273A; Princeton Applied Research, Oak Ridge, TN, USA) that

was controlled by a Powersuite 2.50.0 software (Princeton Applied Research). The distance between the cathode and anode is 1 cm. The working electrode (ZC21/ZSr41/Mg pins) was anodized in 10 M KOH electrolyte at selected voltages at room temperature for 2 h. Prior to anodization, the electrochemical process of ZC21, ZSr41 and Mg pins in 10 M KOH electrolyte and the potential was determined using a linear sweep voltammogram with potentials from -1 to 2.2 V vs. Ag/AgCl for ZC21, -1.8 to 1.9 V Ag/AgCl for ZSr41, and -1.3 to 1.9 V vs. Ag/AgCl for Mg pins at a scan rate of 5 mV/s.

2.2.1.3 Annealing process of the anodized ZC21, ZSr41 and Mg pins

The annealing process was followed the same procedure described in our previous study⁵⁰. The prepared samples by anodization were annealed at 450 °C for 6 hours using a tube furnace in an argon-gas protected environment, to convert the Mg(OH)₂ to MgO through a dehydration reaction. During the annealing process, the temperature increases from room temperature to 450 °C with a heating rate of 50°C /h to avoid sudden collapse of the Mg(OH)₂ crystalline structure. Afterwards, the tube furnace was left to cool down naturally.

2.2.2 Surface characterization of the anodized and annealed-anodized ZC21, ZSr41 and Mg pins

After annealing, the samples were sputter-coated (Model 108, Cressington Scientific Instruments Ltd., Watford, UK) with platinum/palladium at 20 mA with 40 s sputter time. A scanning electron microscope (SEM; Nova NanoSEM 450, FEI Co., Hillsboro, OR, USA) was used to characterize the surface morphology and cross-sections of the oxide layers on Mg substrates. Energy dispersive X-ray spectroscopy (EDS, X-

Max50) and AztecEnergy software (Oxford Instruments, Abingdon, Oxfordshire, UK) was used to analyze the surface elemental composition and distribution. SEM images for the surfaces were taken in the Everhart-Thornley detector (ETD) mode with an acceleration voltage of 20 kV with a working distance of 5 mm and original magnifications of 50,000x. EDS analysis was performed with an accelerating voltage of 10 kV at an original magnification of 50,000x. Different acceleration voltages were used for SEM and EDS because more signals from the surface coatings can be detected at a lower acceleration voltage (10 kV), while more signals from the underlying Mg substrates can be detected at a higher acceleration voltage (20 kV).

2.2.3 Potentiodynamic polarization scans for the annealed-anodized ZC21, ZSr41 and Mg pins

The initial corrosion properties of the annealed anodized ZC21, ZSr41 and Mg pins were determined using electrochemical test. *In vitro* cytocompatibility of the annealed anodized ZC21, ZSr41 and Mg pins. The working electrodes were the annealed anodized ZC21, ZSr41 and Mg pins, and their corresponding non-treated ZC21, ZSr21 and Mg pin controls. The counter electrode was the platinum plate and the reference electrode was Ag/AgCl. The electrolyte was r-SBF at pH of 7.4. The potentiodynamic polarization (PDP) scan started immediately when the working electrode immersed in the r-SBF. The potential was swept from -3.5 to 0.5 V vs. Ag/AgCl at a scan rate of 20 mV s⁻¹. The potential range from -3.5 to 0.5 V vs. Ag/AgCl was selected because the corrosion potential of Mg is around this range. The corrosion potential and corrosion current density were calculated

from the PDP curves according to ASTM G102-89 standard and based on previous publication in details.¹²⁷

2.2.4 Direct culture of BMSC with the anodized ZC21, ZSr41 and Mg pins

The cytocompatibility of the annealed anodized ZC21, ZSr41 and Mg pins cultured with BMSCs was evaluated using direct culture method, which was established previously for evaluating Mg-based biomaterials *in vitro*.^{115,50} The BMSCs were harvested from euthanized two-week-old female Sprague-Dawley rat by following the protocol approved by the University of California at Riverside (UCR) Institutional Animal care and Use Committee (IACUC). The details on BMSC extraction, isolation and culture was described in our previous publications.⁵⁰ Briefly, bone marrow from the femora and tibia of rats was flushed out using DMEM (Sigma-Aldrich, St. Louis, MO, USA) supplemented with 10% fetal bovine serum (FBS; HyClone, Logan, UT, USA) and 1% penicillin/streptomycin (P/S; Invitrogen, Grand Island, NY, USA), which was referred to as DMEM. The collected cells was filter through a 70- μ m nylon strainer to remove cell aggregates and tissue debris, and to collect BMSCs. The filtered BMSCs were cultured in DMEM under standard cell culture condition (i.e., 37°C, 5%/95% CO₂/air, humidified, sterile environment) to reach 90 to 95% confluency.

The samples were disinfected under ultraviolet (UV) radiation for 2h, weighed, photographed and placed in standard 24-well tissue culture treated plates, and rinsed with 2 mL of DMEM to calibrate the osmotic pressure. BMSCs were detached using trypsin (Invitrogen, Grand Island, NY, USA) and seeded directly onto the surfaces of the samples at a seeding density of 10,000 cells cm⁻², incubating in 2 mL of DMEM under standard cell

culture conditions for 24 h. The samples including annealed anodized ZC21, ZSr41 and Mg, and their corresponding non-treated degradable ZC21, ZSr41 and Mg controls, and non-degradable Ti control. Glass slides was used as reference. A positive control consists of BMSCs in DMEM without any samples, was designated as “BMSC” group. A blank reference consisted of DMEM without BMSCs and samples was designated as “DMEM” group.

At 24 h, the post-culture media in all wells were collected and used for measuring pH and ionic concentration (i.e., $[Mg^{2+}]$, $[Zn^{2+}]$, $[Sr^{2+}]$ and $[Ca^{2+}]$) to investigate the *in vitro* degradation of the samples under 24-h BMSC culture in DMEM. The pH of the collected media was measured right after collection using a calibrated pH meter (Model SB70P, VWR). The ionic concentrations in the collected media was measured using inductively coupled plasma optical emission spectrometry (ICP-OES; Optima 8000, PerkinElmer, Waltham, MA, USA). Prior to the ICP-OES measurements, the collected media was diluted to 1: 100 solutions in DI water for measuring the concentration of $[Mg^{2+}]$ and $[Ca^{2+}]$. The collected media was diluted to 1: 5 solutions in DI water for measuring the concentration of $[Zn^{2+}]$ and $[Sr^{2+}]$.

The samples and wells were washed with phosphate buffered saline (PBS) to remove non-adherent cells. The adherent cells were fixed with 4% paraformaldehyde (Electron Microscopy Sciences, 15714-S) for 20 min. The fixed cells were stained with Alexa Fluor® 488-phaoidin (Life Technologies) for F-actin and 4',6-diamidino-2-phenylindole (DAPI; Life Technologies) for the nuclei of the cells. In the direct culture method, the cells adhered on the surfaces of the samples were defined as direct

contact, whereas the cells adhered on the tissue culture plate surrounding the samples were defined as indirect contact. The cells under direct contact and indirect contact conditions were all imaged using fluorescence microscope (Nikon Eclipse Ti-S) at 10 random locations. The number of cells under direct and indirect contact conditions were counted using ImageJ. The cell adhesion density were calculated as the number of cells per unit area.

2.2.5 Bacterial study of MRSA with the anodized ZC21, ZSr41 and Mg pins *in vitro*

Prior to the bacterial culture, the prepared samples were disinfected under UV for 2 hours, while the non-treated Mg control, titanium and glass were sonicated in 100% acetone and ethanol for 30 mins, respectively, followed by disinfection under UV for 2 hours. The samples were then weighed, photographed and placed in standard 24-well non-tissue culture treated plates,

MRSA were culture in sterile tryptic soy broth (TSB; Sigma Aldrich, 22092) and stored at -80°C. A sterile loop was used to transfer a portion of the frozen bacterial stock to 5 mL of TSB. MRSA were cultured in TSB using a shaker incubator (Incushaker Mini, Benchmark Scientific) at 37 °C and 250 rpm for 16 h. An aliquot of 100 µL of MRSA was added to fresh TSB and cultured for another 4-6 h. The as-grown bacteria was washed 3 times with Tris buffer to remove any residual TSB and resuspended in Tris buffer. Then, the bacteria were counted using a hemocytometer (Hausser Bright-Line 3200, Hausser Scientific) and diluted to a concentration of 7.8×10^6 cells/mL in r-SBF supplemented with 10% FBS because this concentration is clinical relevant for medical implant infections.^{47, 73, 128} Subsequently, 2 mL of MRSA in r-SBF supplemented with 10% FBS

was added to each well of 24-well non-tissue culture plates (Corning, Falcon® 351143) that contained the samples. The samples including annealed anodized ZC21, ZSr41 and Mg, and their corresponding non-treated degradable ZC21, ZSr41 and Mg controls, and non-degradable Ti control. Glass slides was used as reference. A positive control consists of MRSA in r-SBF supplemented with 10% FBS without any samples, was designated as “MRSA” group. A blank reference consisted of r-SBF supplemented with 10% FBS without MRSA and samples was designated as “r-SBF” group.

At 24 h, the post-culture bacterial suspension in all wells were collected and used for measuring the bacterial concentration, pH and ionic concentration (i.e., $[Mg^{2+}]$, $[Zn^{2+}]$, $[Sr^{2+}]$ and $[Ca^{2+}]$). To determine the bacterial concentration in the collected bacterial suspension, the bacterial suspension was serially diluted using a proper dilution factor that give a reasonably countable number of CFUs. The bacterial suspension was diluted with Tris buffer and 100 μ L of the diluted suspension was evenly spread onto the agar plates. The agar plates were inverted and incubated at 37°C for 16 to 18 h. The number of bacterial colonies formed on the agar plates were counted, and multiplied the dilution factor the obtain the bacterial density in CFUs mL⁻¹.

The pH and ionic concentrations of the collected bacterial suspension were used to investigate the *in vitro* degradation of the samples under 24-h bacterial culture in r-SBF supplemented with 10% FBS. The pH of the collected bacterial suspension was measured right after collection using a calibrated pH meter (Model SB70P, VWR). The ionic concentrations in the collected media was measured using inductively coupled plasma optical emission spectrometry (ICP-OES; Optima 8000, PerkinElmer, Waltham, MA,

USA). Prior to the ICP-OES measurements, the collected bacterial suspension was diluted to 1: 100 solutions in DI water for measuring the concentration of $[Mg^{2+}]$ and $[Ca^{2+}]$. The collected media was diluted to 1: 10 solutions in DI water for measuring the concentration of $[Sr^{2+}]$.

The morphology of bacteria adhered on surfaces of samples was analyzed using SEM/EDS. The samples in each well were washed with Tris buffer 3 times to remove any non-adherent bacteria. The bacteria adhered on the sample surfaces were fixed with 10% glutaraldehyde (Sigma Aldrich) for 1 h and rinsed 3 times with Tris buffer. The bacteria adhered on the sample surfaces were then dehydrated with 30%, 75% and 100% ethanol for 30 mins each and dried in air at room temperature for 24 h. The dried samples were sputter coated with platinum/palladium (Pt/Pd) for 60 s at 20 mA prior to the SEM/EDS analysis. Representative images were taken using a secondary electron detector at an accelerating voltage of 10 kV, a working distance of 5 mm, with magnifications of 10,000x. To measure the density of bacterial adhered on the sample surfaces, the samples were placed individually into 2 mL of Tris buffer in microcentrifuge tubes. The microcentrifuge tubes were sonicated in a sonication bath for 5 mins and vortexed for 5 s twice to dislodge the adhered bacteria into the Tris-buffer. The Tris buffer containing the bacteria dislodged from the samples were serially diluted and 100 μ L of the diluted and non-diluted suspensions was spread onto the tryptic soy agar plates. The agar plates were inverted and incubated in the incubator at 37°C for 16 to 18 h. The bacterial colonies formed on each agar plates were counted, and multiplied the dilution factor to obtain the bacterial density in CFUs mL^{-1} . The bacterial study was run in triplicate.

2.2.6 Statistical analysis

All numerical data in this study for each experiments were run triplicate. When the normality of the data sets was larger than 0.05 and the data sets was parametric, the numerical data were analyzed using one-way analysis of variance (ANOVA) followed by a Turkey test. Statistical significance was considered at $p < 0.05$ for the Turkey test. When the normality of the data sets was less than 0.05 and the data sets was non-parametric, the numerical data were analyzed using the Kruskal-Wallis method following by the dunn test. Statistical significance was considered at $p < 0.025$ for the dunn test.

2.3 Results

2.3.1 Anodic polarization behaviors for ZC21, ZSr41 and Mg pins

Prior to the anodization process, a linear sweep voltammogram was conducted to select the potential of different Mg alloys (i.e., ZC21, ZSr41 and Mg) at which it begins to be oxidized in the 10 M KOH solution. Figure 2-1a, b, c shows the anodic polarization curve of ZC21, ZSr41 alloys and Mg in the 10 M KOH solution at a scan rate of 10 mV/s. When the potential swept from the negative to the positive value, the anodic polarization process of all the Mg alloys underwent four electrochemical process, which are active dissolution (region A) where the Mg was oxidized to produce Mg^{2+} , passivation (region B) where the Mg^{2+} reacted with OH^- in the electrolyte and form $Mg(OH)_2$ on the electrode surface that thickened with the anodization time and hinder the oxidation rate, secondary oxidation (region C) where the Mg was converted to MgO layer on the electrode surface, and trans-passive processes (region D) where the oxygen evolution occurs on the working electrode that will reduce the anodization efficiency. In this case, the potential in our study

was controlled in the secondary oxidation (region C) to ensure the production of MgO, that is, 1.0 V to 1.9 V for ZC21 alloy, 1.0 V to 1.8 V for ZSr41 alloy and 1.6V to 1.8 V for pure Mg. Therefore, in this study, three different applied potentials were selected in the potential range of the secondary oxidation (region C) for potentiostatic anodization. Specifically, the potentiostatic anodization was carried out at 1.4 V, 1.7 V and 1.9 V vs. Ag/AgCl for ZC21 alloy, 1.4, 1.6, 1.8 V vs. Ag/AgCl for ZSr41 alloy and 1.6 V, 1.7 V, and 1.8 V vs. Ag/AgCl for pure Mg.

2.3.2 Microstructural characterization and surface properties of the anodized ZC21, ZSr41 and Mg pins

The surface morphology of the anodized ZC21, ZSr41 alloy and pure Mg pins prepared at different applied potentials before and after the annealing process is shown in Figure 2-1d, e and f, respectively. The SEM images at high magnification (50,000x) shows that platelet-like nanostructure formed on the surfaces of ZC21 alloy and pure Mg when a lower potential in the secondary oxidation range was applied, i.e. 1.4 V for ZC21 and 1.6 V for Mg. The SEM images for the annealed anodized ZSr41 alloy showed that the applied potentials generated platelet-like nanostructure on the surfaces of ZSr41 alloy with as little change as 200 mV (i.e., 0.2 V) in the applied potentials. When the applied potentials increased, i.e., 1.7 V for ZC21 alloy and 1.7 V for pure Mg, the SEM images show that another dense nano-scale features was generated on previously formed platelet-like nanostructure. As the applied potential further increased to the upper boundary of secondary oxidation region, compact and dense layer consisted of nanoparticles were deposited on the surfaces of ZC21 alloy and pure Mg. In this study, the surface morphology

of anodized Mg, ZC21 and ZSr41 remain unchanged after the annealing process, indicating the MgO layers were thermally stable.

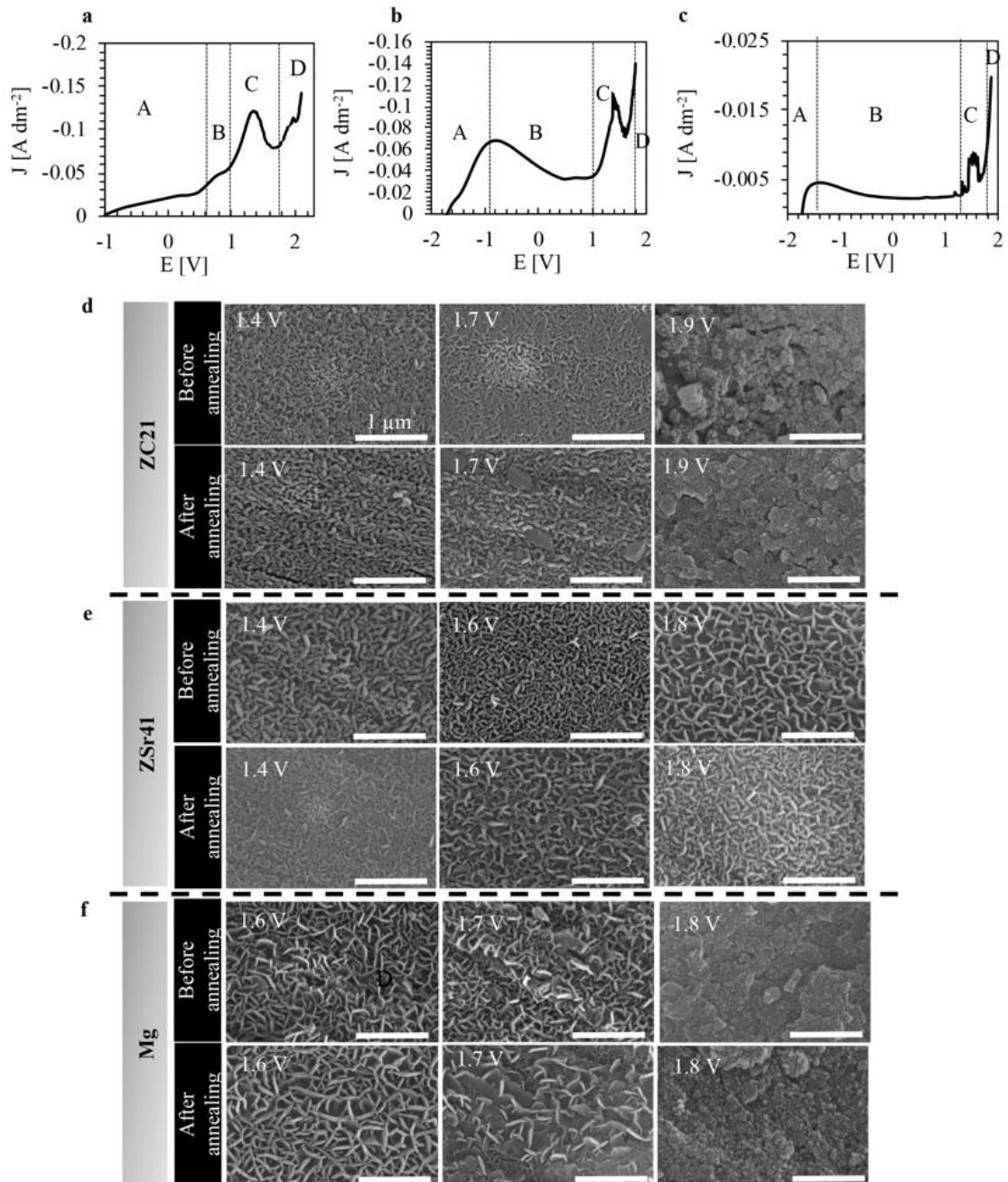


Figure 2-1: Anodic polarization curves and SEM images of ZC21, ZSr41 and Mg. (a-c) Anodic polarization curves of (a) ZC21, (b) ZSr41, and (c) Mg in 10 M KOH at a scan rate of 5 mV s^{-1} at room temperature. A, B, C, D labels for different regions represent four electrochemical process of (A) active dissolution, (B) passivation, (C) secondary oxidation, and (D) transpassive oxidation. (d-f) SEM images of (d) ZC21 anodized at 1.4 V, 1.7 V, 1.9 V before and after annealing, (e) ZSr41 anodized at 1.4 V, 1.6 V, 1.8 V before and after annealing, and (f) Mg anodized at 1.6 V, 1.7 V, 1.8 V before and after annealing. The original magnification is 50,000x and the scale bar = $1 \mu\text{m}$.

2.3.3 Corrosion properties from electrochemical testing of the anodized ZC21,

ZSr41 and Mg pins

In this study, the *in vitro* degradation behavior of the annealed-anodized ZC21, ZSr41 alloys and pure Mg prepared at the selected potentials and their corresponding non-treated ZC21, ZSr41 alloys and pure Mg controls was evaluated via electrochemical test in r-SBF. The electrochemical testing results for the annealed-anodized ZC21, ZSr41 alloys and pure Mg are shown in Figure 2-2, representing the initial *in vitro* degradation behavior of the samples. Figure 2-2a1, b1, c1 shows the representative polarization curves of the annealed-anodized Mg, ZC21, ZSr41 and their corresponding controls (Mg, ZC21, ZSr41) at a scan rate of 10 mV/s. The cathodic curve and the anodic curve within the polarization curve represents hydrogen evolution from the water reduction and the dissolution of the Mg, respectively. The corrosion current density (J_{corr}) and the corrosion potential (E_{corr}) for each sample type obtained from Tafel extrapolation of the polarization curves are shown in Figure 2-2a2, b2, c2 and Figure 2-2a3, b3, c3, respectively. The more negative the E_{corr} , the higher the possibility for the metallic materials to be oxidized. The higher the J_{corr} , the higher the corrosion rate of the metallic materials. In terms of the ZC21 alloy, J_{corr} of the annealed-anodized ZC21 alloy samples produced at 1.4 V, 1.7 V and 1.9 V vs. Ag/AgCl was significantly lower than that of the non-treated ZC21 control. Though significant difference in J_{corr} was detected among the annealed-anodized ZC21 samples, the annealed-anodized ZC21 produced at 1.9 V vs. Ag/AgCl showed the lowest J_{corr} value in average. No significant difference in E_{corr} was detected for among the annealed-anodized ZC21 alloys and non-treated ZC21 control. In terms of ZSr41 alloy, J_{corr} of the annealed-

anodized ZSr41 produced at 1.4 V, 1.6 V and 1.8 V vs. Ag/AgCl was significantly lower than that of the non-treated ZSr41 control. Though no significant difference in J_{corr} was detected among the annealed-anodized ZSr41 alloy samples, the annealed-anodized ZSr41 produced at 1.8 V vs. Ag/AgCl shows the lowest J_{corr} value in average. No significant difference in E_{corr} was detected among the annealed-anodized ZSr41 alloys and non-treated ZSr41 control. In terms of pure Mg, no significant difference in J_{corr} and E_{corr} was detected among the annealed-anodized pure Mg and non-treated pure Mg control. The annealed-anodized Mg produced at 1.8 V vs. Ag/AgCl shows the lowest J_{corr} value in average.

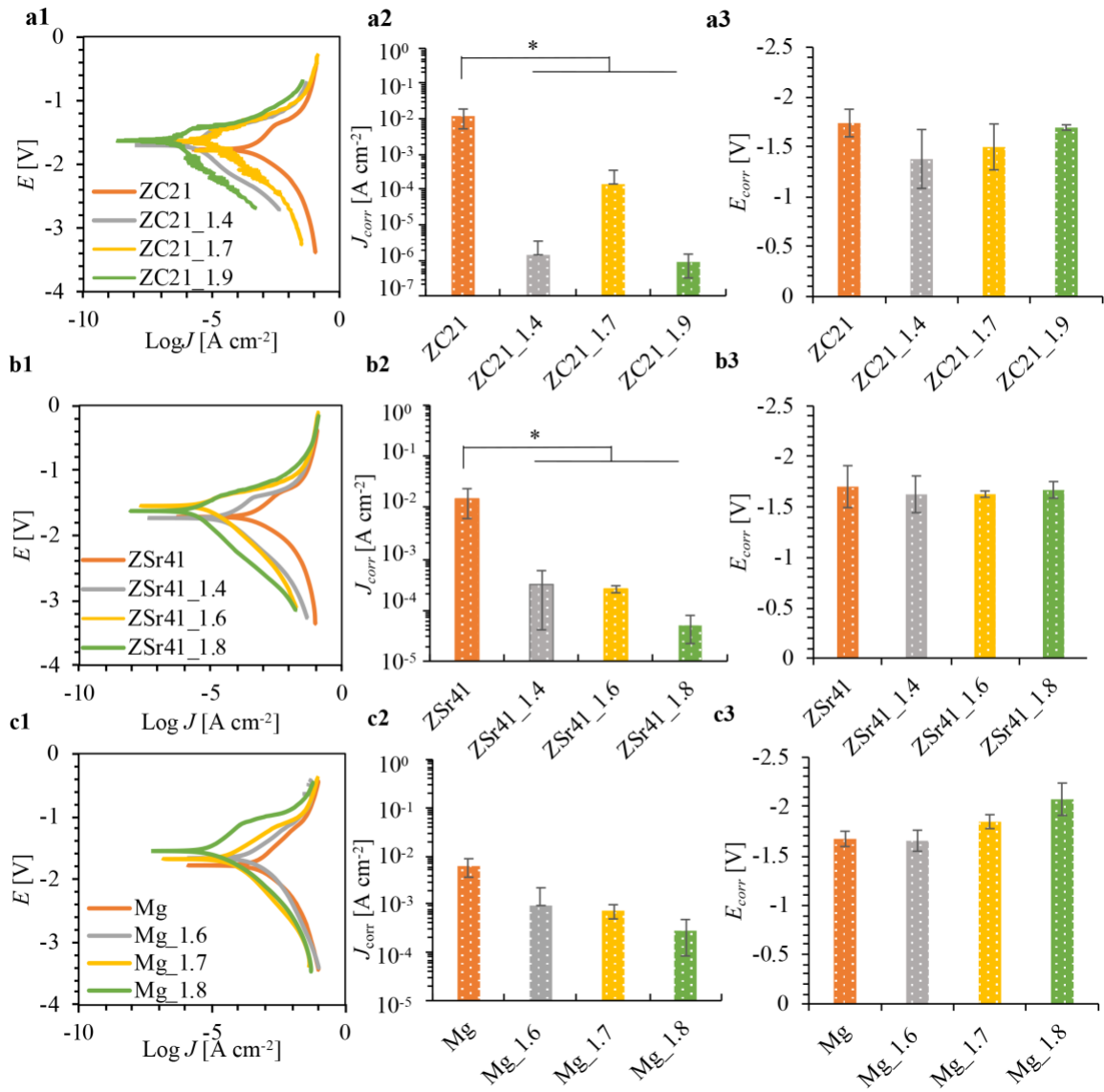


Figure 2-2: Representative potential dynamic polarization (PDP) curves of annealed-anodized ZC21, ZSr41 and Mg in r-SBF electrolyte, and their corresponding corrosion current density J_{corr} and corrosion potential E_{corr} . (a1) PDP curves of ZC21, (a2) J_{corr} of ZC21, and (a3) E_{corr} of ZC21. (b1) PDP curves of ZSr41, (b2) J_{corr} of ZSr41, and (b3) E_{corr} of ZSr41. (c1) PDP curves of Mg, (c2) J_{corr} of Mg, and (c3) E_{corr} of Mg. Values are mean \pm SD, $n=3$, $*p<0.05$.

2.3.4 Cytocompatibility of the anodized ZC21, ZSr41 and Mg pins with BMSCs in direct culture and post-culture media analysis

Figure 2-3 summarizes the representative fluorescence images and the quantitative analysis of the annealed-anodized ZC21, ZSr41 alloy samples and pure Mg, and their corresponding non-treated ZC21, ZSr41 alloys and Mg controls in 24-h direct culture with BMSCs in DMEM under direct contact condition. In Figure 2-3a, it shows that BMSC could sparsely attached on the pins. Fewer cells was found on the surface of Ti control. It is observable that few viable cells were attached on the annealed-anodized ZC21 and ZSr41, Mg and their corresponding non-treated ZC21, ZSr41 alloys and Mg controls. The quantitative analysis of BMSCs under the direct contact condition is shown in Figure 1b. Kruskal-Wallis method was used for statistical analysis because the data sets were non-parametric. No significant difference in the BMSC adhesion density under direct contact was detected among all samples, controls and references.

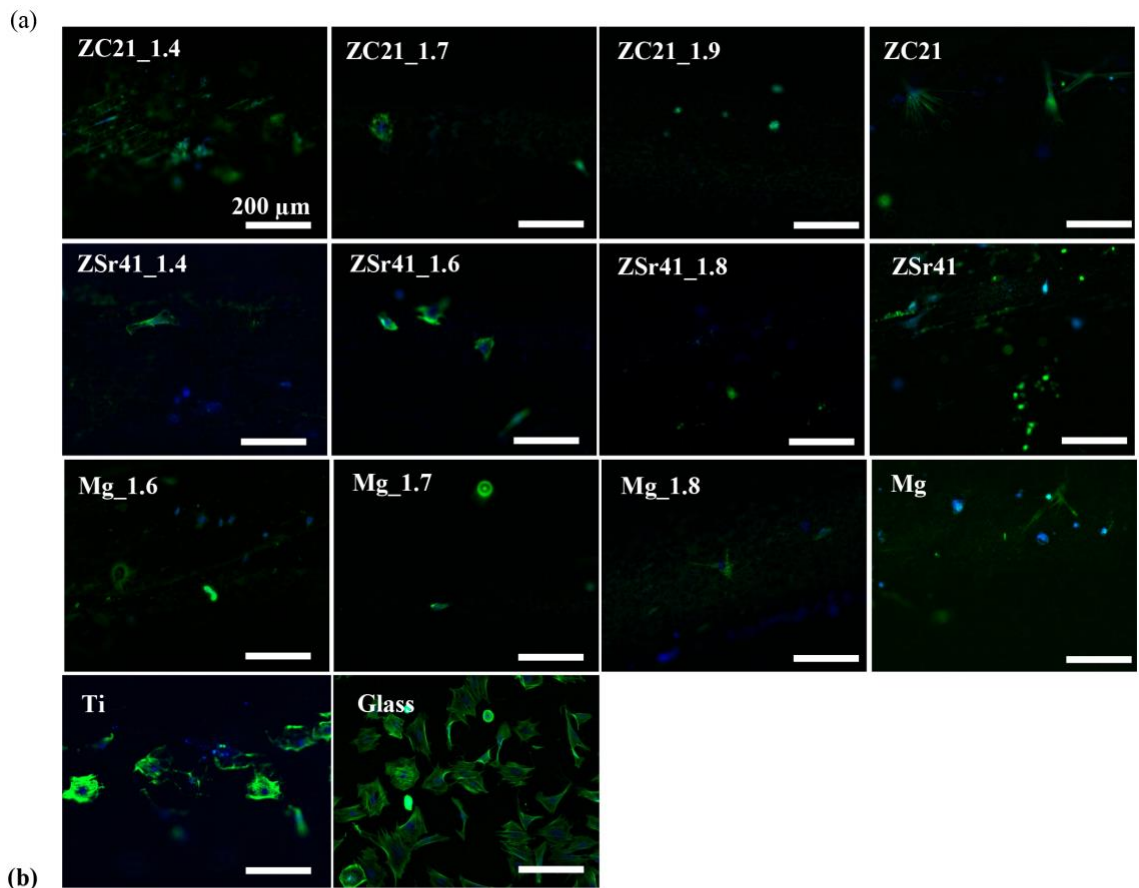


Figure 2-3: BMSC adhesion of the annealed-anodized ZC21, ZSr41 and Mg, and the controls of ZC21, ZSr41, Mg, and Ti, as well as glass reference under direct contact after 24 h of direct culture. (a) Representative fluorescence images of the adhered BMSCs on the sample surfaces (direct contact with the samples) at 24 h. (b) Adhesion density of BMSCs on the sample surface (direct contact with the sample). Values are mean \pm SD, $n=3$, $*p<0.05$.

Figure 2-4 summarizes the representative fluorescence images and the quantitative analysis of the annealed-anodized ZC21, ZSr41 alloy samples and pure Mg, and their corresponding non-treated ZC21, ZSr41 alloys and Mg controls in 24-h direct culture with BMSCs in DMEM under indirect contact condition. In Figure 2-4a, all the groups showed attached and viable BMSCs on the well plate, the morphology of the BMSCs attached on the well plates surround the annealed anodized ZC21, ZSr41 alloy and Mg, and their corresponding non-treated ZC21, ZSr41 and Mg controls are as isotropic spreading as that on the well plates surrounding the Ti control and glass reference. The quantitative analysis of BMSCs under indirect contact condition was shown in Figure 2-4b. One-way ANOVA was used for statistical analysis because the data sets were parametric. The BMSC adhesion density under indirect contact was significantly lower for the annealed-anodized Mg prepared at 1.8 V vs. Ag/AgCl than the glass reference. No significant difference in BMSC adhesion density under indirect contact was detected among all other groups.

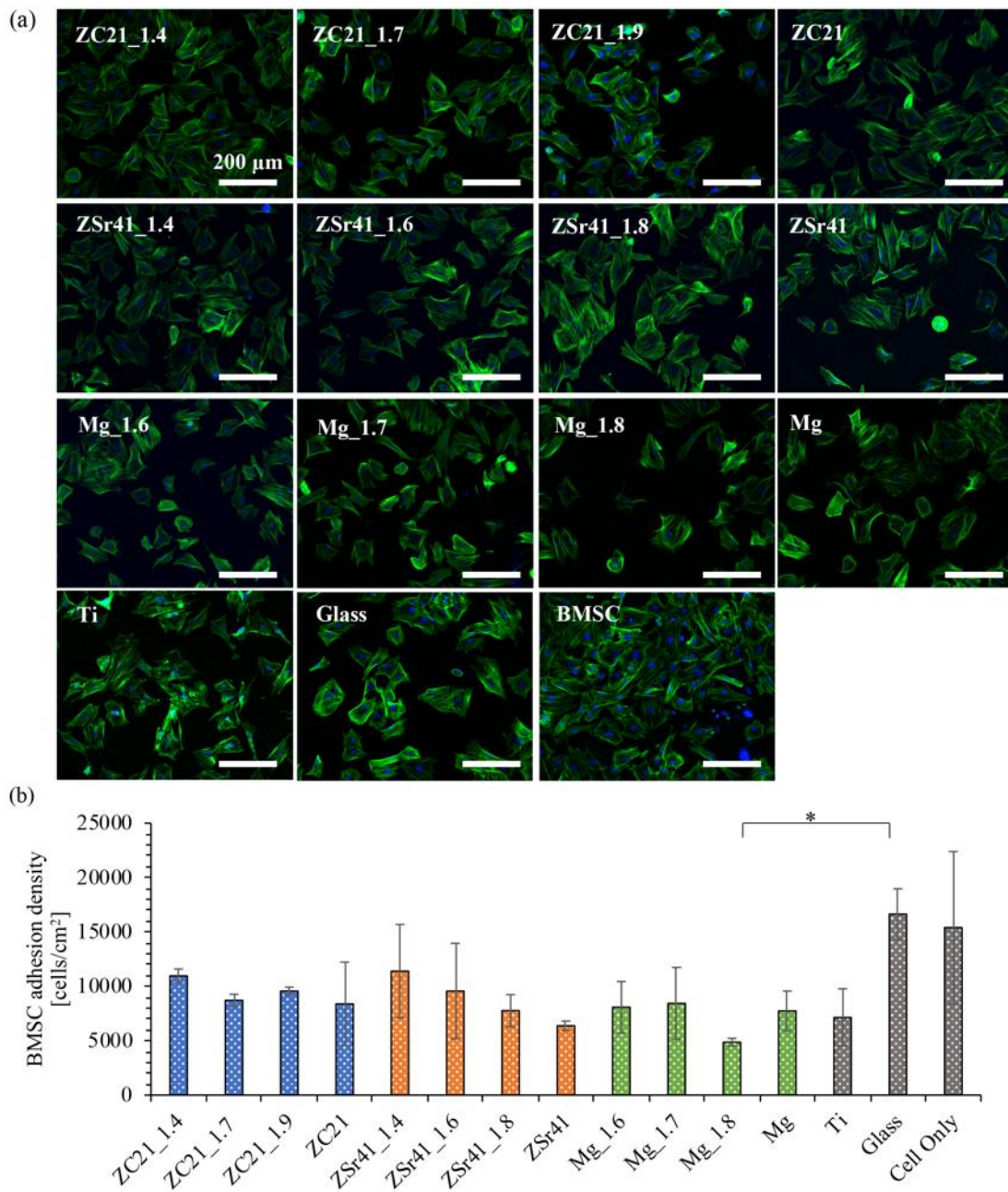


Figure 2-4: BMSC adhesion of the annealed-anodized ZC21, ZSr41 and Mg, and the controls of ZC21, ZSr41, Mg and Ti, as well as glass reference under indirect contact after 24 h of direct culture. (a) Representative fluorescence images of the adhered BMSCs on the culture plate surrounding each corresponding sample (indirect contact with the sample) at 24 h. (b) Adhesion density of BMSCs on the culture plate surrounding each corresponding sample (indirect contact with the sample). Values are mean \pm SD, $n=3$, $*p<0.05$.

Figure 2-5 shows the pH, $[Mg^{2+}]$, $[Ca^{2+}]$, $[Sr^{2+}]$ and $[Zn^{2+}]$ of the collected media after BMSCs were cultured with the annealed-anodized ZC21, ZSr41 alloys and Mg their corresponding non-treated ZC21, ZSr41 alloys and Mg controls, Ti control, glass reference, cell-only and media-only references at 24 h. One-way ANOVA was used for the statistical analysis of the pH because the data sets were parametric. The pH of the collected media cultured with annealed-anodized Mg prepared at 1.6 V are significantly higher than that cultured with the glass and Media-only references. The pH in the collected media cultured with annealed-anodized Mg prepared at 1.7 V are significantly higher than that cultured with the Media-only reference. No significant differences of the pH in the collected media was detected among other groups. One-way ANOVA was used for the statistical analysis of the $[Mg^{2+}]$ because the data sets were parametric. ANOVA confirmed a significantly higher $[Mg^{2+}]$ in the collected media after 24-h direct culture with the ZC21_1.9 sample when compared with the Ti control and Media-only reference. Kruskal-Wallis method was used for the statistical analysis of the $[Mg^{2+}]$ because the data sets were non-parametric. No significant differences in the $[Ca^{2+}]$ in the collected media was found among all groups of samples, controls and references. One-way ANOVA was used for the statistical analysis of the $[Sr^{2+}]$ because the data sets were parametric. The $[Sr^{2+}]$ in the collected media cultured with ZSr41_1.4, ZSr41_1.6, ZSr41_1.8 were significantly higher than that of the ZC21_1.4, ZC21_1.7, ZC21_1.9, ZC21, ZSr41, Mg_1.6, Mg_1.7, Mg_1.8, Mg, Ti, Glass, Cell-only and Media_only. Among the groups of annealed-anodized ZSr41 alloy samples, ANOVA confirmed a significant higher $[Sr^{2+}]$ in the collected media cultured with the ZSr41_1.4 and ZSr41_1.6 samples when compared with the ZSr41_1.8 sample.

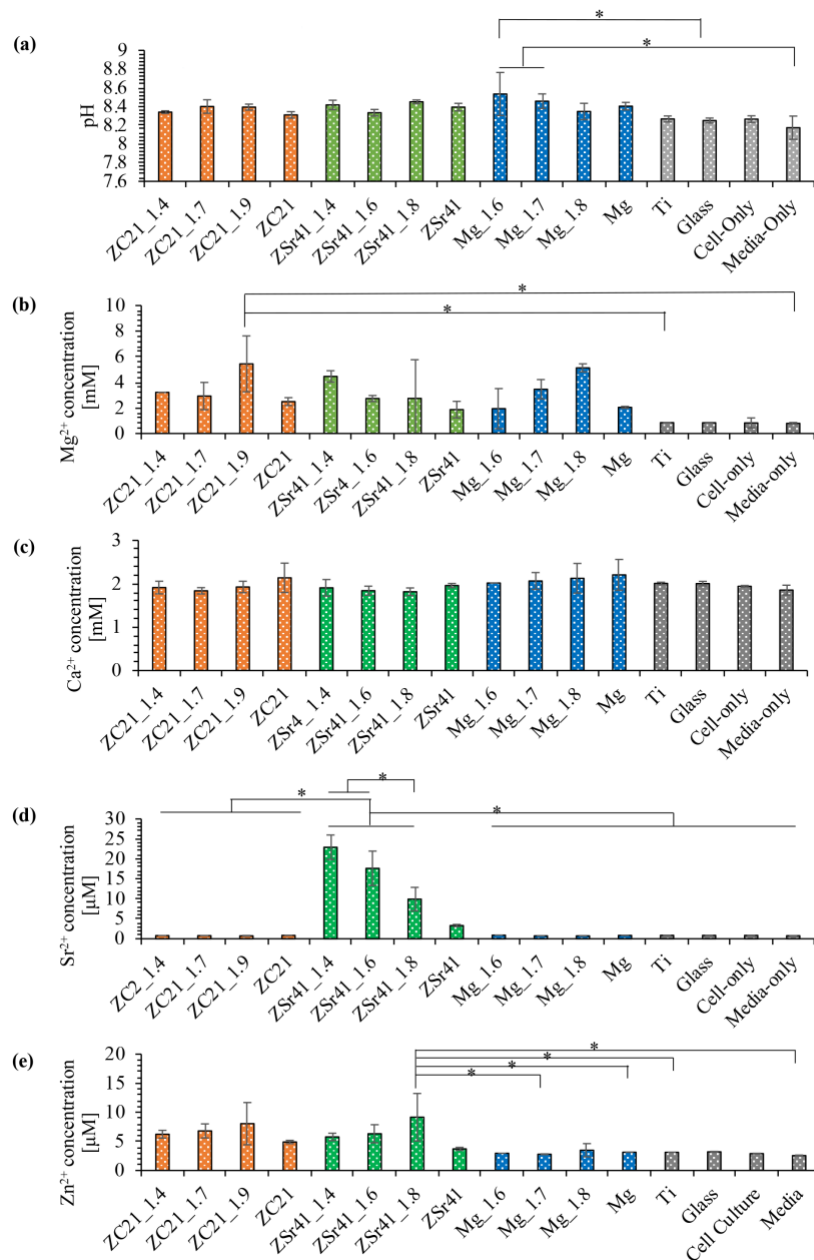


Figure 2-5: Analysis of solubilized degradation products in the culture media of the annealed-anodized ZC21, ZSr41 and Mg, the controls of ZC21, ZSr41, Mg and Ti, and glass reference, as well as the cell-only positive control and blank DMEM (media-only). (a) pH of media, (b) Mg²⁺ concentration in the culture media, (b) Ca²⁺ concentration in the culture media, (d) Sr²⁺ concentration in the culture media, (e) Zn²⁺ concentration in the culture media. Values are mean \pm SD, n = 3 for all groups, * p < 0.05.

2.3.5 Antibacterial properties of the anodized ZC21, ZSr41 and Mg pins cultured with MRSA and post-culture media analysis

Bacterial viability was quantified through CFU grown on the agar plates, as shown in Figure 2-6. Figure 2-6a and b shows the representative images of MRSA colonies grew on agar plates. Figure 2-6a represents the bacteria dislodged from the sample surfaces and Figure 2-6b represents the bacteria from the suspension cultured with the sample. Figure 2-6b shows the bacteria density in the suspension and on the sample surfaces. The actual seeding density in this study were 6.8×10^6 CFU/ml, as indicated by the red dashed line. One-way ANOVA was used for the statistical analysis of the bacterial density adhered on the sample surfaces and in the suspension, because both data sets were parametric.

For the bacteria density in the suspension, no significant differences were found among all groups of samples. However, the bacteria density in the suspension cultured with the Ti, glass and MRSA-only groups still higher in average than the annealed-anodized ZC21, ZSr41 alloy, and Mg samples and their corresponding non-treated ZC21, ZSr41 and Mg controls. For the bacteria density on the sample surfaces, ANOVA confirmed that the CFUs of MRSA cultured with the ZC21_1.7, ZC21_1.9 and ZC21 samples were significantly lower when compared with those cultured with the Mg_1.6, Mg_1.7 samples and Glass reference. The CFUs of MRSA cultured with the ZC21_1.9 sample was were significantly lower when compared with the Ti control. The CFUs of MRSA cultured with the Mg_1.8 sample was were significantly lower when compared with the Mg_1.6 sample. No significant difference in the bacteria density on the sample surfaces were detected among other groups of samples.

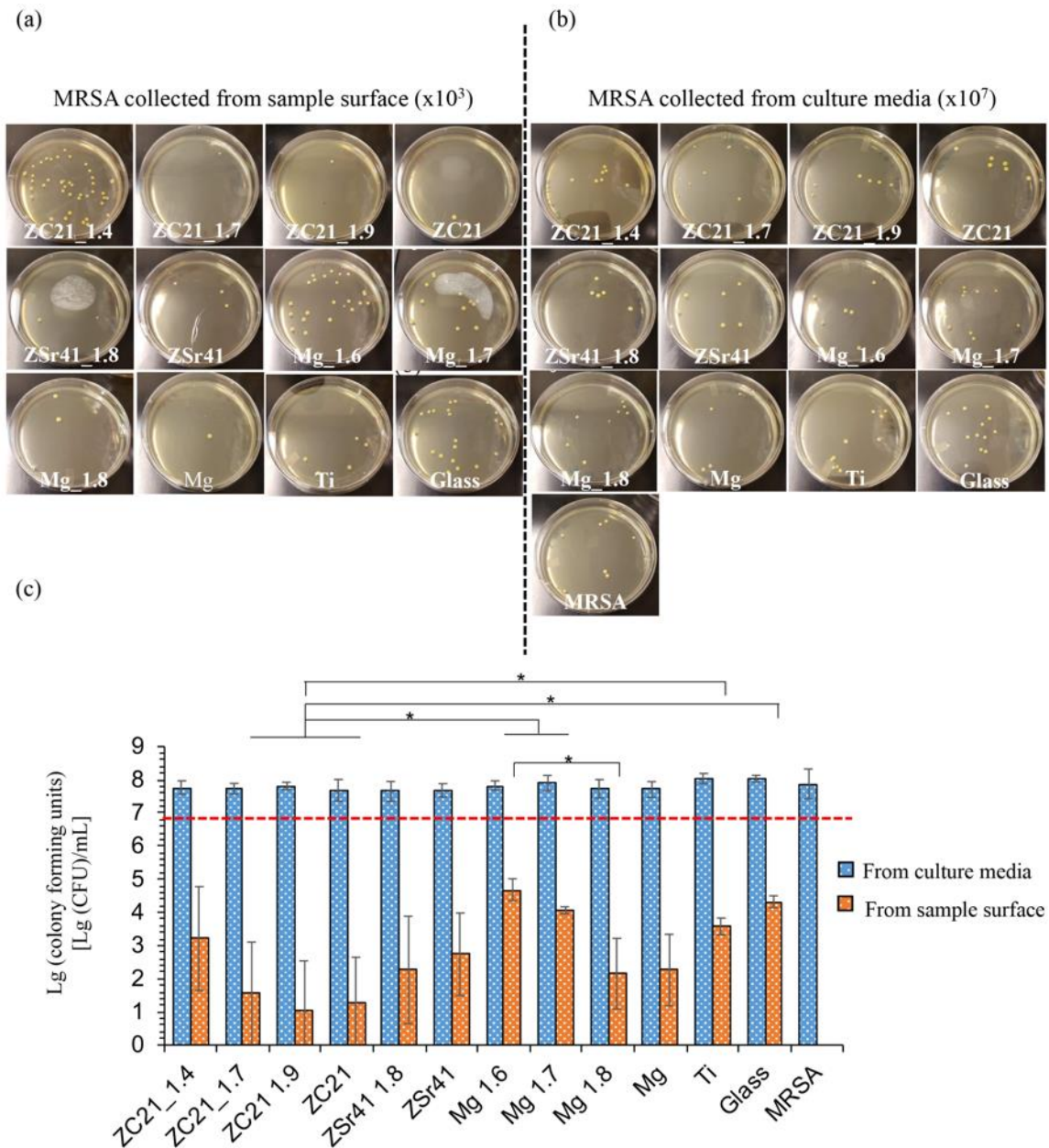


Figure 2-6: CFUs of MRSA after 24-h culture with the annealed-anodized ZC21, ZSr41, and Mg, the controls of ZC21, ZSr41, Mg, Ti, and glass reference, and the MRSA-only positive control, in r-SBF supplemented with 10% FBS. (a,b) Representative images of agar plates for MRSA (a) collected from the sample surfaces and (b) collected from the culture media. (c) The quantified CFUs of MRSA collected from the sample surfaces (orange) and from the culture media (blue). The seeding concentration of MRSA was 6.8×10^6 CFU/mL, as indicated by the red dashed line. Values are mean \pm SD, n=3, * p <0.05.

SEM images, the overlay of SEM images and EDS maps and the EDS maps of elemental distribution of carbon (C), calcium (Ca), phosphorous (P) and oxygen(O), were taken after 24-h bacterial culture with samples, controls and references, as shown in Figure 2-7. The bacteria on the surfaces of ZC21_1.4, non-treated ZSr41 alloy, Ti and Glass were aggregated with an appearance of biofilm. In contrast, very few single bacteria were found on the surfaces of ZC21_1.9, ZC21, ZSr41_1.8 and Mg_1.8 samples. Moreover, the bacteria on the surfaces of ZC21_1.4, ZC21_1.7, ZSr41, Mg_1.6, Mg_1.7, Mg, Ti, and glass show typical spherical-shape morphology, but was distorted, irregular or even lysed on the surfaces of ZC21_1.9, ZC21, ZSr41_1.8 and Mg_1.8 samples.

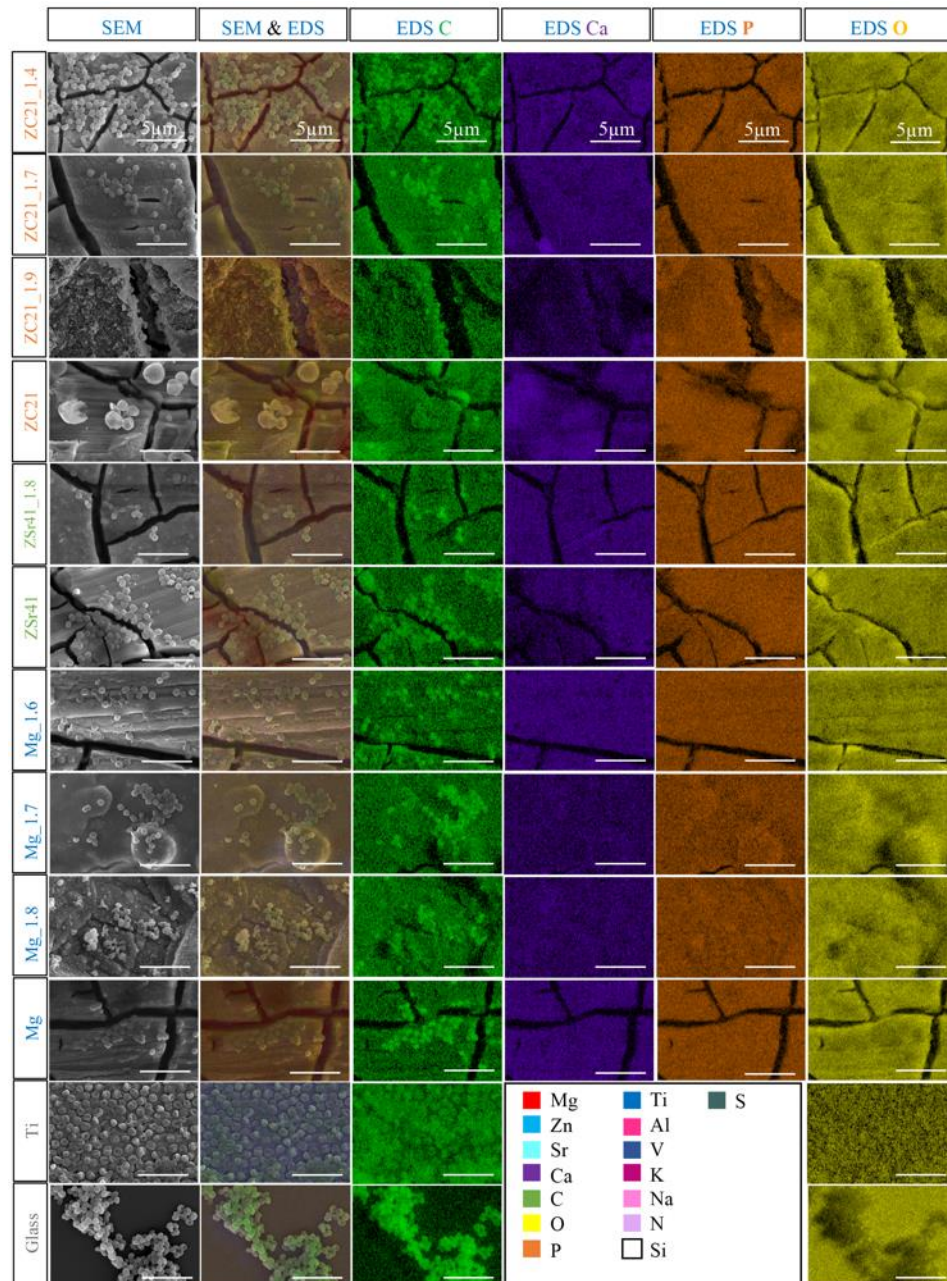


Figure 2-7: SEM images and EDS maps for annealed-anodized ZC21, ZSr41 and Mg, the controls of ZC21, ZSr41, Mg and Ti, and glass reference after 24-h bacterial culture. SEM images (SEM column) show the surface microstructure and bacterial morphologies. The overlaid SEM and EDS maps (SEM + EDS column) show overview for the distribution of all key elements of interest. Separate EDS maps for carbon (C), calcium (Ca), phosphorous (P), and oxygen (O) are also included in the respective columns. Scale bar = 5 μm with an original magnification of 10,000x.

Figure 2-8 summarizes the elemental composition (in wt %) for the annealed anodized ZC21, ZSr41 alloys and Mg, and their corresponding non-treated ZC21, ZSr41 and Mg controls, Ti controls, Glass reference after 24 h of bacterial culture, quantified through EDS analyses at the original magnification of 10,000x. A Zn content was detected on the surfaces of ZC21 alloy and ZSr41 alloy, respectively. With the increase of applied potentials for the ZC21 alloy, the detected Zn content in the annealed anodized ZC21 alloys decreased. The detected Zn content in the annealed anodized ZC21 and ZSr41 alloys were lower than those in their corresponding non-treated ZC21 and ZSr41 alloy controls. All Mg-based samples shows the composition of Mg, C, O, Ca and P. The elements of C comes from the bacteria and the colocalization of Ca, P and O indicated the degradation of Mg possibly attracted Ca-containing mineral deposition. In terms of ZC21 alloys, the element of Ca could also come from the intermetallic compounds. In contrast, the Ti and Glass did not show the deposition of Ca and P. Lastly, , the Ti and Glass show sodium (Na) and Potassium (K) because of salt deposition from the culture media.

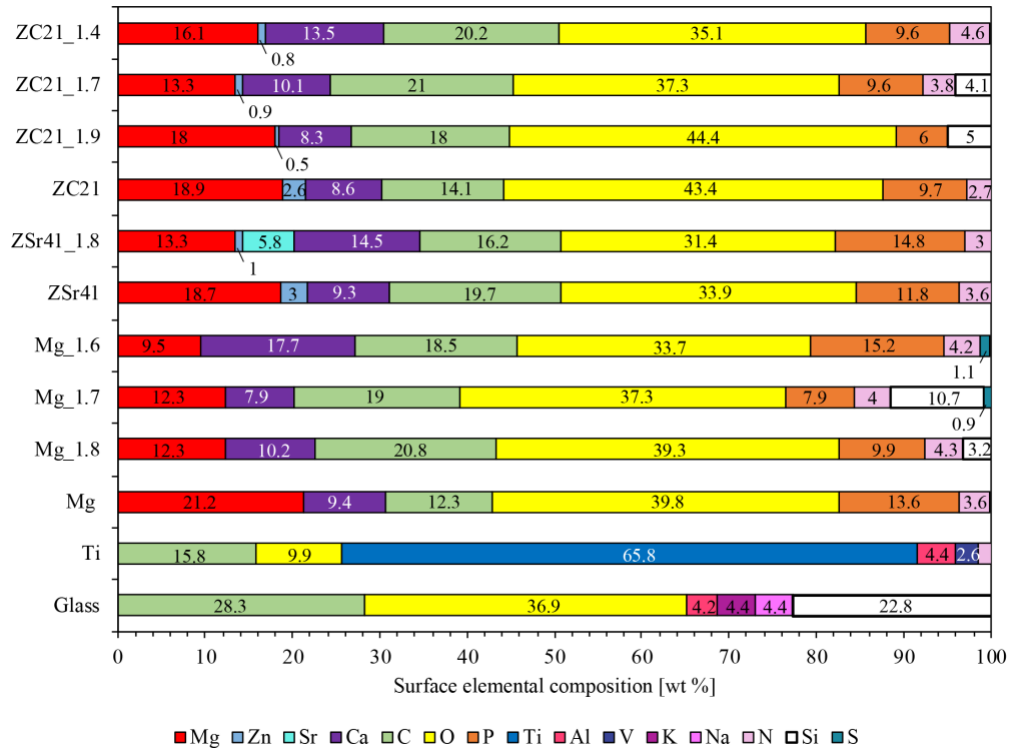


Figure 2-8: The quantitative elemental compositions for the annealed-anodized ZC21, ZSr41, and Mg, the controls of ZC21, ZSr41, Mg and Ti, and glass reference after 24-h bacterial culture.

The pH and ionic concentrations (i.e., $[Mg^{2+}]$, $[Ca^{2+}]$, $[Sr^{2+}]$) in the collected media after 24-h bacterial cultured with the annealed anodized ZC21, ZSr41 alloys and Mg, and their corresponding non-treated ZC21, ZSr41 and Mg controls, Ti controls, Glass reference, MRSA-only and r-SBF-only were analyzed, as shown in Figure 2-9. One-way ANOVA was used for the statistical analysis of pH and ionic concentrations because the data set were non-parametric. ANOVA confirmed a significantly higher pH in the collected media cultured with ZC21_1.9 when compared with the Glass reference. The $[Mg^{2+}]$ in the collected media cultured with the ZC21_1.4, ZC21_1.7, ZC21_1.9, ZSr41_1.8, Mg_1.6, Mg_1.7, Mg_1.8 and Mg samples were significantly higher than those of the Ti, Glass and

MRSA-only and r-SBF-only groups. The $[\text{Mg}^{2+}]$ in the collected media cultured with the ZC21_1.9 sample was significantly higher than the ZC21 sample. Lastly, the $[\text{Mg}^{2+}]$ in the collected media cultured with the ZSr41_1.8 sample was significantly higher than the Mg sample. In terms of $[\text{Ca}^{2+}]$, ANOVA confirmed a significant lower $[\text{Ca}^{2+}]$ in the collected media cultured with ZC21_1.9 sample when compared with the Glass reference. No significant differences in $[\text{Ca}^{2+}]$ in the collected media was found among other groups of samples. For $[\text{Sr}^{2+}]$ in the collected media, ANOVA confirmed a significantly increase $[\text{Sr}^{2+}]$ of the ZSr41_1.8 and ZSr41 samples among all groups of samples.

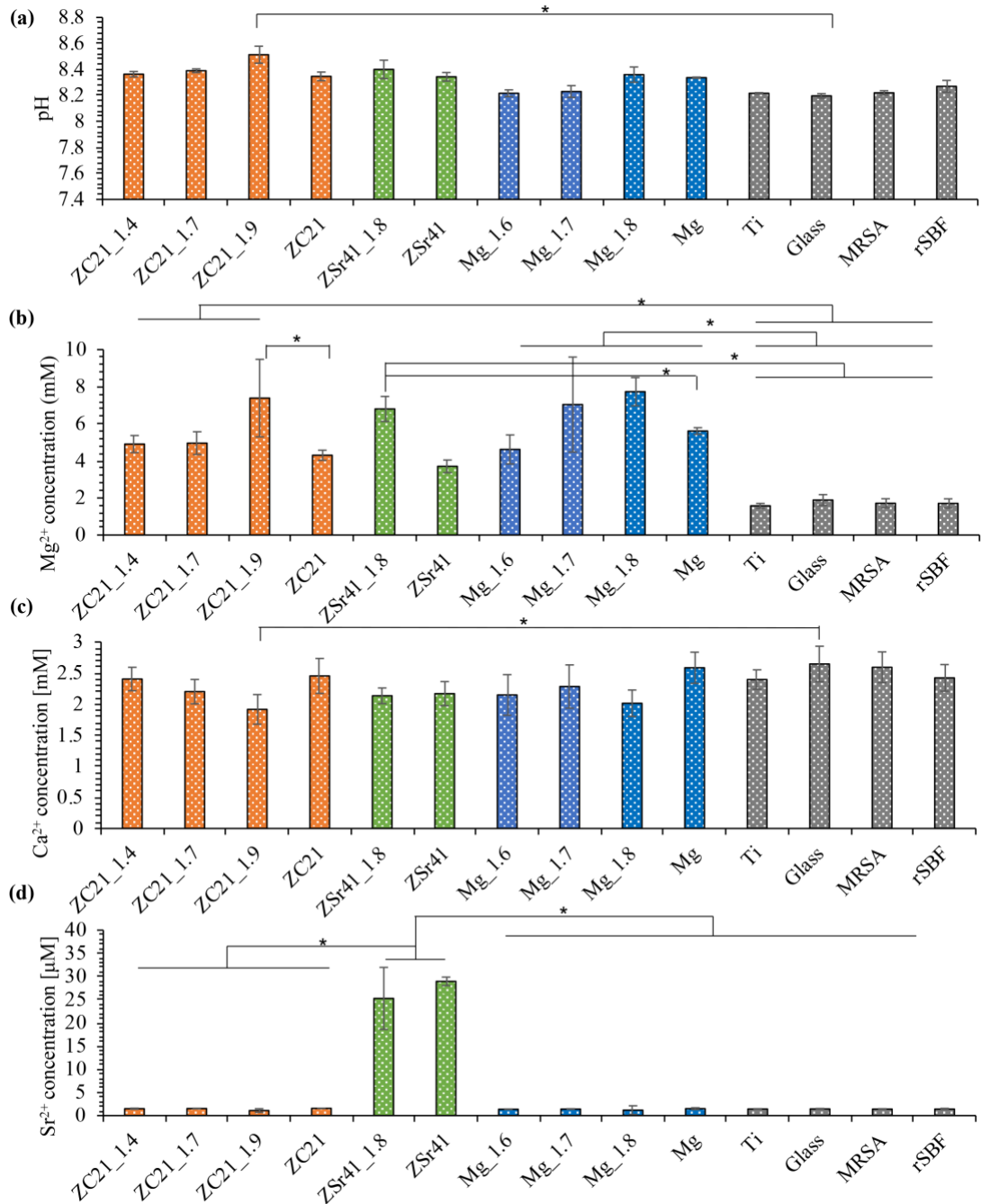


Figure 2-9: Analysis of solubilized degradation products in culture media of the annealed-anodized ZC21, ZSr41 and Mg, the controls of ZC21, ZSr41, Mg and Ti, and glass reference, as well as the MRSA-only positive control, and blank r-SBF reference. (a) pH of media, (b) Mg²⁺ ion concentration, (c) Ca²⁺ ion concentration, and (d) Sr²⁺ ion concentration. Values are mean \pm SD, n = 3 at all groups, * $p < 0.05$.

2.4 Discussion

In this study, nanostructured MgO layers were created onto ZC21, ZSr41 and Mg pins through anodization and annealing. We investigated the microstructure and corrosion properties of the annealed anodized Mg-based biomaterials, reported the BMSC response through 24-h direct culture with the samples; studied the antimicrobial properties of the annealed anodized Mg-based biomaterials against MRSA; analyzed the effects of solubilized degradation products on cell/bacterial adhesion and morphology, and compared the in vitro degradation properties of the annealed anodized Mg-based biomaterials in different cultured media with BMSCs or MRSA.

2.4.1 Effects of anodization parameters on nanostructured MgO layers onto ZC21, ZSr41 alloys and pure Mg

The anodic polarization curves of the Mg-based alloys and pure Mg control in 10 M KOH were similar to the anodic polarization curve for Mg-Zn-Ca alloy rod (5.5 – 6.5 wt% Zn, 1.0-1.5 wt % Ca and Mg balance) in 6 M KOH reported by Lei et al, consisting of four electrochemical processes, i.e., active dissolution (region A), passivation (region B), secondary oxidation (region C) and trans-passive process (region D). The different behavior. However, in our previous study, the anodic polarization curve of the pure Mg substrate in 10 M KOH only consisted of active dissolution (region A), passivation (region B) and trans-passive process (region D), probably because of the different geometry and composition of the Mg-based metals we used in this study.

The surface morphology of the anodized and annealed anodized Mg-based metals in this study prepared at lower potentials (i.e., 1.4 V for ZC21 and 1.6 V for Mg) resembled

the pure Mg substrates anodized at 1.8 V for 2 h in 10 M KOH by Cipriano et al. and the Mg-Zn-Ca alloy anodized at 1.0 V for 2 h in 6 M KOH by Lei et al, which showed nano-scale homogeneous platelet-like morphology at high magnifications (40,000x). As the applied potentials were more positive (i.e., 1.7 V for ZC21 and 1.7 V for Mg), a secondary dense nano-scale features were generated on the as-anodized and annealed-anodized ZC21 and Mg pins. When the applied potentials reached the boundary of the secondary oxidation region (i.e., 1.9 V for ZC21 and 1.8 V for Mg), homogenous dense nano-scale crystallized features, which was very similar to the secondary dense nano-scale features mentioned above, were formed on the surfaces of the as-anodized and annealed-anodized ZC21 and Mg pins. The three applied potentials for ZC21 and Mg pins produced three various surface morphology of nanostructure MgO layers on their surfaces without any observable cracks propagation or defects through the film of the samples. For ZSr41 alloy, nano-scale homogeneous platelet-like morphology was form on the surfaces of as-anodized and annealed-anodized ZSr41 alloy pins at all selected potentials.

Electrochemical test has been widely used for determining the initial degradation properties of metals. The corrosion potential (E_{corr}) and corrosion current density (J_{corr}) indicate the possibility for metals to be oxidized and the initial corrosion rate of metals, respectively. The corrosion current densities of ZC21, ZSr41 alloys and pure Mg pins were around 10^{-2} A cm⁻², which were in agreements with previous study.⁶⁷ The significantly smaller J_{corr} of the annealed-anodized ZC21, ZSr41 and Mg pins when compared with their corresponding non-treated ZC21, ZSr41 and Mg controls indicated a slower initial corrosion rate in r-SBF. Though no significant differences in J_{corr} were found among each

groups of annealed-anodized Mg-based metals, the average J_{corr} of ZC21_1.9 sample, ZSr41_1.8 sample and Mg_1.8 that anodized at the upper end of the secondary oxidation region were lower when compared with those anodized at lower or intermediate potentials, indicating a lower average corrosion rate for these samples.

2.4.2 *In vitro* cytocompatibility of anodized Mg alloys in direct culture with BMSCs

The difference in adhesion density of BMSCs under direct contact among the annealed-anodized Mg-based metals and their corresponding non-treated controls was negligible because no statistically significant difference was found. As expected, Glass reference showed higher BMSC adhesion density and a greater cell spreading area than the Ti and the Mg-based metals, because the glass slide used in this study has a flatter surfaces which may benefit the cell adhesion and glass has been widely used as a positive control in cell cultures and is favorable for cell adhesion.^{51, 123-124} The objective of the BMSC study was to compared the cytocompatibility of the Mg-based metals and to screen the most promising candidate for each group of Mg-based metals toward *in vivo* studies and pre-clinical trials in the future. The adhesion and morphology of the BMSCs on the surfaces of Mg-based metals was very similar to what has been observed on the non-treated ZC21, ZSr41 and Mg pins at the same seeing density in direct culture reported by Zhang et al.⁶⁷ The less BMSC adhesion and spreading on the Mg-based metals when compared with the higher degree isotropic spreading of BMSCs on Ti with same geometry, indicating the change in the surface morphology, newly formed degradation compounds at the cell-biomaterials interface, and dynamic change in the soluble ions releasing from the Mg-based metals at the interfaces play critical roles in affecting the BMSCs under direct contact.

For the adhesion and morphology of BMSC under indirect contact, the difference among all groups of samples was negligible because no statistically significant difference was found, suggesting that the release of soluble ions such as OH^- , Mg^{2+} , Ca^{2+} , Sr^{2+} and Zn^{2+} from the Mg-based metals did not affect the surrounding BMSCs. In previous study, BMSC adhesion and morphology were not affected when the cell cultured in DMEM with the pH adjusted to pH 9.0 or supplemented with 27.6 mM of $[\text{Mg}^{2+}]$.¹¹⁵ In the BMSC study, the highest pH in the culture media was below 8.6 and the highest $[\text{Mg}^{2+}]$ in the culture media was below 8 mM, which are unlikely to cause adverse effects on the surrounding BMSCs. The therapeutic daily dosages of $[\text{Zn}^{2+}]$, $[\text{Ca}^{2+}]$ and $[\text{Sr}^{2+}]$ are 0.9 mM,¹²⁹ 250-750 mM¹³⁰⁻¹³¹ and 5.9 mM,¹³² respectively. The lethal dosage (LD50) of $[\text{Zn}^{2+}]$ and $[\text{Sr}^{2+}]$ are 3.7 mM¹³³ and 33.9 mM,¹³⁴ respectively. And it was found that the cytotoxicity of $[\text{Zn}^{2+}]$ and $[\text{Ca}^{2+}]$ when cultured with HeLa and L-929 cell lines were 60 μM for $[\text{Zn}^{2+}]$ and 30 mM for $[\text{Ca}^{2+}]$.¹³⁵ Therefore, the $[\text{Zn}^{2+}]$, $[\text{Ca}^{2+}]$ and $[\text{Sr}^{2+}]$ in the culture media were well below the cytotoxicity level, therapeutic daily dosages and lethal dosage. In contrast, all ion concentrations (i.e., $[\text{OH}^-]$, $[\text{Mg}^{2+}]$, $[\text{Zn}^{2+}]$, $[\text{Ca}^{2+}]$ and $[\text{Sr}^{2+}]$) could be higher at the surface of Mg-based metals because dynamic degradation reactions, thus could cause adverse effect on BMSCs under direct contact.

2.4.3 *In vitro* antimicrobial properties of anodized Mg alloys against MRSA

In combination of the CFUs and the SEM/EDS of the bacteria adhered on the surfaces of non-treated ZC21, ZSr41 and Mg, MRSA adhesion was reduced on the surface of non-treated ZC21 when compared with the non-treated ZSr41 and Mg, which was in agreement with the previous studies that showed significantly reduced MRSA adhesion on

same samples.⁶⁷ Lin et al. reported bactericidal effects of nanostructured MgO layers on pure Mg substrates created via anodization against *S. aureus* using a method adapted from the Japanese Industrial Standard JIS Z 2801:2000, as the bacteria had close contact with the surfaces of samples.¹²⁶ This is the first time we investigated the antimicrobial properties of annealed-anodized Mg-based metal pins against MRSA using direct cultured method, and analyzed the effects of soluble ions released from the Mg-based metals on the adhesion and morphology of MRSA. Our previous study⁴⁷ demonstrated that the growth of *Staphylococcus epidermidis* (*S. epidermidis*) was not affected when they were cultured in the broths with pH adjusted from 7 – 10 and the [Mg²⁺] adjusted up to 50 mM.⁴⁷ Wetteland et al. reported that the pH ranged from 7 – 10 and [Mg²⁺] ranged from 1 – 50 mM did not affect the growth of *Escherichia coli* (*E. coli*) and *S. epidermidis*.⁴⁶ However no literature has reported the effects of pH and [Mg²⁺] in the culture media on the growth of MRSA.

In this study, the nanostructure MgO layer on Mg-based metals could dissociate, resulting in releasing more OH⁻ ions and Mg²⁺ ions, increasing the pH of the culture media. The annealed-anodized ZC21, ZSr41 and Mg produced at higher applied potentials (i.e., ZC21_1.9, ZSr41_1.8 and Mg_1.8) had higher average pH and [Mg²⁺] in their culture media after 24-h bacterial culture when compared with non-treated ZC21, ZSr41 and Mg controls. The pH and [Mg²⁺] in the culture media of the annealed-anodized ZC21, ZSr41 and Mg produced at lower or intermediate applied potentials (i.e., ZC21_1.4, ZC21_1.9, Mg_1.6 and Mg_1.7) showed comparable pH values and [Mg²⁺] to the non-treated ZC21, ZSr41 and Mg controls, which probably because of the thinner nanostructured MgO layers on their surfaces and the buffering effect of the culture media and metabolic activities of

the bacteria. Moreover, the CFUs measurements (Figure 2-6) in combined with the SEM/EDS images (Figure 2-7) showed reduced adhesion of MRSA on the surfaces of ZC21_1.9 and Mg_1.8 among their corresponding annealed-anodized ZC21 and Mg samples; and reduced adhesion of MRSA on the surfaces of ZSr41_1.8 when compared with the non-treated ZSr41 sample. We speculated that the elevated global $[Mg^{2+}]$ in the culture media of the annealed-anodized ZC21, ZSr41 and Mg samples produced at higher applied potentials could inhibit the growth of MRSA. Moreover, the nanostructure MgO layers on ZC21_1.9, ZSr41_1.8 and Mg_1.8 disrupted the morphology of MRSA more obviously than other samples, further suggesting the higher level of local pH and $[Mg^{2+}]$ on the surfaces plays an important role in affecting the adhesion of MRSA. Another proposed antimicrobial mechanism could be the difference in the nanostructure of MgO on the annealed anodized Mg-based metals prepared at different applied potentials. The dense and compact nanostructured MgO layers of the ZC21_1.9 and Mg_1.8 sample may have a larger surface area than the platelet-like nanostructured MgO layers of the ZC21_1.4, ZC21_1.7, Mg_1.6 and Mg_1.7 samples, which could provide more sites for disrupting bacterial activities. More importantly, no biofilm formation or bacterial colonies was found on the surfaces of ZC21_1.9, ZSr41_1.8 and Mg_1.8, suggesting their great potential in preventing severe infections and associated complications for medical implants.

2.4.4 Anodization of Mg alloys for biomedical applications

To improve the overall performance of Mg-based biomaterials, either adding alloying elements or surface treatments for pure Mg has been investigated in our previous studies.^{50, 67} The degradation properties, cytocompatibility and antimicrobial properties of

the nanostructured MgO on pure Mg substrates produced via anodization has been reported previously.^{50, 126} And the degradation properties, cytocompatibility and antibacterial properties of the ZC21 and ZSr41 alloys has been studied.⁶⁷ Lei et al. investigated the corrosion properties of the nanostructured MgO on MgZnCa alloys.¹³⁶⁻¹³⁷ The significance of this study is that we carried out an in-depth systematic research to investigate the degradation, cytocompatibility and antimicrobial properties *in vitro* of the nanostructured MgO onto ZC21 and ZSr41 alloys, by coupling the benefits of adding alloying elements with surface treatments for Mg-based biomaterials. Moreover, in this study, we studied the correlation between processing parameters and surface properties, the effects of the surface properties and soluble degradation products on the cell/bacterial response at the interfaces of the prepared samples. The surface-treated ZC21, ZSr41 and Mg pins had significant lower initial degradation rates when compared with their corresponding non-treated ZC21, ZSr41 and Mg pin controls. The soluble degradation products released from the surface-treated ZC21, ZSr41 and Mg pins does not have adverse effects on the surrounding BMSCs. The surface-treated ZC21, ZSr41 and Mg pins anodized at 1.9 V, 1.8 V and 1.8 V, respectively, had fewer adhesion of MRSA and observable cell/membrane damage of MRSA on their surfaces when compared with those anodized at lower or intermediate potentials. Additionally, the surface-treated ZC21 alloys anodized at 1.9 V had the lowest initial degradation rate and bacterial adhesion density on its surface in average among all groups of sample.

The collective properties of the surface-treated ZC21, ZSr41 and Mg pins indicate that the alloying elements in pure Mg coupling with surface treatment could further

improve the overall performance of Mg-based biomaterials. The surface-treated ZC21, ZSr41 and Mg pins anodized at 1.9 V, 1.8 V and 1.8 V, respectively, are promising for medical implant applications. In the future, we will conduct *in vivo* studies to verify the biosafety, degradation properties, osseointegration and antibacterial properties of the samples toward clinical translations.

2.5 Conclusions

In this study, we created distinct nanostructured MgO layers onto Mg-Zn-Ca alloy and Mg-Zn-Sr alloy and pure Mg through anodization and annealing, reported the corrosion properties, cytocompatibility of the samples in direct culture with BMSC in DMEM, and investigated the antimicrobial properties of the samples against MRSA. The ZC21 and Mg anodized at potentials (i.e., 1.9 V for ZC21 and 1.8 V for Mg) that reached the upper end of the secondary oxidation region generated homogenous dense nanostructured MgO layer, whereas the surface microstructures were all plate-like nanofeatures for ZSr41 anodized at all selected applied potentials. The corrosion rates obtained from electrochemical tests were lower for the annealed-anodized Mg-based metals when compared with the non-treated ZC21, ZSr41 and Mg controls. The difference in BMSC cultured with the Mg-based metals under direct and indirect contact were negligible, the soluble degradation products released from the Mg-based metals were below the cytotoxicity levels. ZC21_1.9, ZSr41_1.8 and Mg_1.8 samples showed inhibitory effects on the growth of MRSA, which are promising to prevent severe infections for biomedical applications. Therefore, collectively considering the corrosion properties, BMSC responses, and bacterial response, ZC21_1.9, ZSr41_1.8 and Mg_1.8

intramedullary pins are recommended for further *in vivo* studies in infection animal models towards clinical translations.

Chapter 3 *In Vitro* Degradation, Cytocompatibility, and Antimicrobial Properties of
Micro and Nano-micro Hydroxyapatite Loaded with Gentamicin Coated Magnesium

Abstract

This article reported the surface microstructures, elemental compositions, *in vitro* cytocompatibility, antimicrobial properties and degradation properties of micro hydroxyapatite (mHA) and nano-micro hydroxyapatite (nmHA) loaded with gentamicin coated Mg. The surface microstructure of the mHA coated Mg samples were homogeneous, while visible minicracks and agglomerates were formed of the nmHA coated Mg samples . No significant difference in the BMSC adhesion density under direct contact was found among all HA coated Mg samples and Mg control. Under indirect contact, the mHA coated Mg samples had higher BMSC adhesion density when compared with the nmHA coated Mg samples. Moreover, the antimicrobial properties of the mHA coated Mg against *S. aureus* from the culture media was enhanced when increased content of gentamicin was loaded into the mHA coating layers, specifically, the mHA+3G sample showed the best antimicrobial effects against *S. aureus* from the culture media. The 12-week immersion study shows that the degradation rate among the mHA coated Mg samples and the nmHA sample, and Mg control were similar, without any significant differences.

3.1 Introduction

Bone fractures are very common diseases that requires orthopedic fixations using biomedical implants.¹³⁸ Magnesium (Mg) is a promising candidate for orthopedic implants because of its good combination of mechanical properties and biological responses.¹³⁹⁻¹⁴² Specifically, Mg is biodegradable in physiological environment and the by-products released by Mg are non-toxic and can be excreted through the kidney. The released Mg²⁺ can enhance osteoblast response and promote osteointegration.^{139, 141-142} For temporary orthopedic implant applications, the elastic modulus and mechanical strength of Mg is similar to the human cortical bone, which can reduce the stress-shielding effect.²¹ Additionally, secondary surgery for implant removal may not be required, which can reduce the morbidity and costs for patients.¹⁴³⁻¹⁴⁴ However, the fast degradation of Mg still raises safety concerns because it may lose mechanical integrity before the complete healing of the tissue, and the fast release of hydrogen gas will form gas pocket at the surgical site that could cause tissue separation and delay bone healing.^{116, 145} Therefore, proper control of the degradation process on Mg is imperative. Moreover, the risk of infections after internal fixation is between 0.4% to 16.1% according to the type of fractures (i.e., closed or varying degree of open infections).¹⁴⁶⁻¹⁴⁷ The biomaterials-associated infections could delay the bone healing process or even result in implants failure, which can increase the morbidity, as well as creating great financial burden for the patients.¹⁴⁸

Hydroxyapatite chemical and structural similarity to the mineral component of natural bone.¹⁴⁹ Hydroxyapatite has been used as a coating for metallic implant because of its good osteoconductive and moderate osteoinductive capabilities.¹⁵⁰ Hydroxyapatite

coated Mg has shown slower degradation rate¹⁵⁰⁻¹⁶² and improve the cell attachment and proliferation when cultured with different cell lines, i.e., osteoblasts,^{150-151, 154, 162} human osteosarcoma cells,¹⁵⁹ and fibroblasts.¹⁶¹ Moreover, hydroxyapatite coated Mg has been studied *in vivo*, such as implantation in the tibias of rabbits,¹⁶³ frontal bone of rats,¹⁶⁴⁻¹⁶⁵ and subcutaneously into one side of the back of mice.¹⁶⁰ The *in vivo* studies showed desirable biodegradation and biocompatibility. Based on our previous study,¹⁶⁶ micro-sized hydroxyapatite (mHA) coated Mg slowed the degradation rate when compared with the nano-sized hydroxyapatite (nHA) coated Mg and non-coated Mg. However, mHA coated Mg showed higher bacteria adhesion density when compared with the nHA coated Mg. Incorporating antibiotics in the HA coatings is one of the effective methods to further reduce implant infections. Gentamicin is a widely used broad-spectrum aminoglycoside antibiotic against bacterial infections though inhibiting the protein synthesis of bacteria.¹⁶⁷ Therefore, we first proposed to create mHA loaded with gentamicin on Mg. Second, we proposed to develop a composite coating (named as nmHA) with a bottom mHA layer and a top nHA layer loaded with gentamicin on Mg, to achieve the synergic effects of mHA and nHA.

The objective of this study is to investigate the degradation properties, cytocompatibility and antimicrobial properties of the mHA and nmHA coated Mg incorporated with gentamicin for load-bearing applications. The mHA and nmHA coatings with different percentages of gentamicin were deposited on Mg using a patented transonic particles acceleration deposition (TPA) process.¹⁶⁸

3.2 Materials and Methods

3.2.1 Prepare mHA and nmHA coatings loaded with gentamicin on Mg using patented transonic particles acceleration (TPA) process

Pure Mg miniscrews (99.9% purity, Goodfellow Corporation, Coraopolis, PA) with a diameter of 1.6 mm and a length of 6 mm were cleaned ultrasonically in ethanol for 10 mins prior to the HA coating process. The mHA (Himed, Old Bethpage, NY) particles was deposited on the surface of Mg miniscrews using the patented transonic particle acceleration (TPA) deposition process at high pressure, followed by depositing nHA particles(Himed, Old Bethpage, NY) loaded with different contents of gentamicin (10 wt.%, 20 wt.% and 30 wt.%) using the same method. The resulted samples was referred to as nmHA, nmHA+1G, nmHA+2G and nmHA+3G, the “1”, “2” and “3” designates “10 wt.%”, “20 wt.%” and “30 wt.%”, respectively and “G” designates “gentamicin”. The TPA technique is a method used at N2 Biomedical (formerly Spire Biomedical Inc.) for depositing ceramic particles onto various surfaces and has been previously used for creating hydroxyapatite layers on Mg substrates under precisely controllable processing conditions ¹⁶⁶. Specifically, a high pressure gas (400 psi) was introduced into a nozzle and accelerate in the throat region of the nozzle. A process gas was blow through a gas control module to a powder-metering device that contained the nHA or mHA particles, which was accelerated to sub-sonic speed during the TPA process and deposited onto the Mg substrates at room temperature at a pressure of 400 psi. In terms of the mHA coated Mg, a single layer of mHA with different contents of gentamicin (10 wt.%, 20 wt.% and 30 wt.%) was deposited on Mg, the resulted sample was referred to as mHA, mHA+1G,

mHA+2G and mHA+3G. The “1”, “2” and “3” designates “10 wt.%”, “20 wt.%” and “30 wt.%”, respectively and “G” designates “gentamicin”. Non-coated Mg was also included as a control..

3.2.2 Surface characterization

Prior to surface characterization, all samples were sputter-coated with platinum/palladium (Pt/Pd) using the sputter coating instrument (Cressington; Sputter Coater 108 Auto) at 20 mA for 60 second. The surface microstructures were characterized using a scanning electron microscopy (SEM; Nova NanoSEM 450, FEI Co.) at an accelerating voltage of 15 kV. The SEM images were taken at the magnifications of 50x, 500x, and 5000x. The surface elemental composition of the samples was analyzed using energy dispersive x-ray spectroscopy (EDS; Aztec, Oxford instrument) at an accelerating voltage of 15 kV at a magnification of 500x.

3.2.3 *In vitro* direct culture with bone marrow derived mesenchymal stem cells

(BMSCs)

The bone marrow derived mesenchymal stem cells (BMSCs) were extracted from the femur and tibia of juvenile Sprague Dawley rats following the established protocol,¹⁶⁹ which was approved by the Institutional Animal Care and Use Committee (IACUC) at the University of California, Riverside. The methods for BMSC harvesting were carried out in accordance with the recommendations in the Guide for the Care and Use of Laboratory Animal of the National Institutes of Health (NIH). BMSCs were cultured in Dulbecco’s modified Eagle medium (DMEM; Corning) supplemented with 10 vol. % fetal bovine serum (FBS; Hyclone) and 1 vol. % penicillin/streptomycin (P/S; Hyclone). DMEM refers

to DMEM with 10% FBS and 1% P/S. BMSCs at the second passages were used for *in vitro* experiments with samples and Mg control. The titanium (Ti) and poly(methyl methacrylate) (PMMA) miniscrews, and glass reference were included in the cell study. The initial mass of each sample was recorded, and disinfected under ultraviolet (UV) radiation for 2 h before cell culture. The Ti and glass reference were ultrasonically cleaned in acetone and ethanol for 30 mins each to remove any residues on the surfaces.

The samples were placed in standard 48-well cell culture treated plates and rinsed with 1 mL PBS and then 1 mL DMEM for each well to calibrate the osmotic pressure. The BMSCs were seeded directly onto the samples in each well at a seeding density of 10000 cells/cm², incubated for 24 hours in 1 mL of DMEM under standard cell culture conditions (sterile, 5% CO₂/95% air, humidified environment). Non-degradable titanium (Ti) was used as a control and glass was used a reference. A positive control consisted of BMSCs only cultured with 3 mL DMEM in the 12-well culture plate without any samples, was define as 'BMSCs'. A blank reference contained DMEM without BMSCs and samples was defined as 'DMEM' group.

After 24 hours of cell culture, the media were collected from each well for pH and ionic concentration analyses. BMSCs on the surface of samples (direct contact) and on the well plates surrounding the respective samples (indirect contact) were fixed in 4% paraformaldehyde (10% neutral buffered formalin; VMR, Radnor, PA, USA) for 20 minutes, stained with Alex Fluor 488 Phalloidin (Life Technologies, Carlsbad, CA) for another 20 minutes to visualize F-actin, and finally stained with 4', 6-diamidino-2-phenylindole (DAPI; Invitrogen) for 5minutes to visualize cell nuclei. After fixation and

staining, BMSCs were observed and imaged using a fluorescence microscope (Eclipse Ti with NIS 241 software, Nikon, Melville, NY, USA) for analyses of cell morphology and cell adhesion density. Five images were taken on random areas of each sample for direct contact, and five images were taken on random areas of each well plate for indirect contact. The number of cells in each image was quantified using ImageJ. The cell adhesion density under direct contact and indirect contact conditions was calculated as the number of cells per unit area. Each type of sample was run in triplicate in this *in vitro* cell study for repeatability and statistical analyses.

3.2.4 *In vitro* bacteria study with Staphylococcus aureus (*S. aureus*)

The bacterial study was carried out following the established protocol ¹⁷⁰. Frozen stocks of *S. aureus* (ATCC 25923) were retrieved and cultured in Tryptic Soy Broth (TSB; Fluka Analytical, Sigma-Aldrich) for 16 h in a shaker incubator (Incu-shaker Mini, Benchmark Scientific) at 37 °C and 250 rpm. After 16 h, an aliquot of 100µL of the bacterial culture was added into 5 mL of fresh TSB, and this bacterial culture was incubated for additional 4–6 hours at 37 °C and 250 rpm. After that, the concentrations of bacteria were diluted and determined using a hemocytometer (Hausser Bright-Line 3200, Hausser Scientific). The bacteria was centrifuged and washed with revised simulated body fluid (r-SBF) three times to remove any residual TSB. The bacteria was then diluted to a theoretical concentration of 6.8×10^6 cells/ml in r-SBF with 10 vol.% FBS, which is a relevant concentration for orthopedic infections ¹⁷¹. The samples were cultured in the 96 well non-tissue culture treatment polystyrene plate (Corning, Falcon, 351143) with the addition of 0.232 ml of *S. aureus* in r-SBF with 10 vol.% FBS. The non-degradable Ti and PMMA

controls with diameter of 7.5 mm and heights of 1 mm were included in this study and cultured in the 48 well non-tissue culture treatment polystyrene plate with the addition of 0.757 ml of *S. aureus* in r-SBF with 10 vol.% FBS. The groups of glass reference, *S. aureus* alone (without samples) and r-SBF alone (without samples and bacteria) were cultured in the 12 well non-tissue culture treatment polystyrene plate with the addition of 3 ml of *S. aureus* in r-SBF with 10 vol.% FBS. All groups were incubated for 24 h in a shaker incubator at 37°C and 120 rpm. After 24 h, the bacteria in the media were collected for analysis of suspended bacterial concentration, pH and ionic concentrations. In order to quantify the bacteria adhered on the sample surfaces, two samples in each groups were put into the r-SBF, sonicated in a sonication bath for 10 mins, vortexed for 15 s every 5 mins. The detached bacteria in the r-SBF, and the suspended bacteria in the cultured media, were diluted and quantified by measuring the colony forming units (CFU) plated on Tryptic Soy Agar (Sigma Aldrich) plates. The agar plates were inverted with the agar on the top side and incubated for 16-18 h. The number of colonies form on the agar were counted and multiply by the dilution factor to get the bacterial viability values.

After 24 h of culture, the pH, Mg²⁺ and Ca²⁺ concentration of the post-cultured media were analyzed. The pH of the cultured media was analyzed using a pre-calibrated pH meter. The Mg²⁺, Ca²⁺ concentration of the post-culture media collected from each well after the bacteria study were quantified using the inductive coupled plasma-optical emission spectrometry. The collected media from each well was diluted with DI water by a dilution factor of 1:100 to obtain a total volume of 5 mL for ICP measurement. Mg²⁺ and Ca²⁺ concentrations were calculated based on a calibration curve generated using Mg²⁺

standards (PerkinElmer) serially diluted to a concentration of 0.5, 1, 2, and 5 mg/L and Ca^{2+} standards (PerkinElmer) serially diluted to a concentration of 0.05, 0.5, and 5 mg/L, respectively.

3.2.5 Immersion study in r-SBF *in vitro*

The degradation performance of the HA coated Mg miniscrews were investigated via immersion study in revised simulated body fluid (r-SBF) under standard cell culture conditions (sterile environment, controlled humidity, 5% CO_2 , 37 °C). Non-coated Mg was used as a degradable control in this study. The prescribe time point for the immersion study is 1 day, 3 days, 5 days, 7 days and 2 weeks, 4 weeks, 6 weeks, 8 weeks, 10 weeks and 12 week. Before the immersion study at each prescribed time point, all samples were weighed and disinfected under ultraviolet (UV) radiation for 2 hours. All groups of sample were incubated in 0.232 mL of r-SBF. The group that contains 0.232 mL of r-SBF alone without samples was used as a blank reference. For each time interval between the prescribed time points, the immersion solution was collected from each well for post-culture media analysis, i.e., pH and ionic concentrations. Each well was then replenished with 0.232 mL of fresh r-SBF. The pH of the post-culture r-SBF was analyzed using a pre-calibrated pH meter (SB70Pm, SympHony, VWR). The Mg^{2+} , Ca^{2+} ion concentration of the post-culture media were quantified using the inductive coupled plasma-optical emission spectrometry (ICP-OES; Optima 8000, PerkinElmer, Waltham, MA, USA). Before the ICP measurement, the collected media from each well was diluted with DI water using the dilution factor of 1:100 to obtain a total volume of 5 mL. Mg^{2+} and Ca^{2+} ion concentrations were calculated based on a calibration curve generated using Mg^{2+}

standards (PerkinElmer) serially diluted to a concentration of 0.5, 1, 2, and 5 mg/L and Ca^{2+} standards (PerkinElmer) serially diluted to a concentration of 0.05, 0.5, and 5 mg/L, respectively. All the samples were dried at least for 24 hour and photographed using the Amscope at each interval to observed the corrosion at the macroscale on the surface of the substrates. Each sample was weighed to get the initial mass (M_0) and final mass (M_f), which were used to calculate the ratio of the final/initial dry mass (M_f/M_0). Each sample was run triplicate for the immersion study.

After 12 weeks of immersion, all the samples were dried and placed on a conductive copper tape and sputter coated for SEM imaging and EDS analyses, as described previously. The phases and crystal structures of the degradation products on samples and Mg control were analyzed using the X-ray diffraction (XRD; Empyrean, PANalytical) at 45KV and 40mA with 2θ angles from 10° to 80° at a step size of 0.002° . Specifically, the diffraction peaks of degradation products were identified based on the international center for diffraction data (ICDD) database using HighScore software (PANalytical).

3.2.6 Statistical analysis

All the experiments were run in triplicate. The data sets were analyzed using one-way analysis of variance (ANOVA) followed by the Tukey test, when the data sets fulfil the parametric criteria (i.e., data normality was over 0.05). Under the condition of non-parametric data (i.e., data normality was less than 0.05), the data sets were analyzed using the Kruskal-Wallis followed by the Dunn test and adjusted by Hochberg's method. Statistical significance was considered at $p < 0.025$ for Dunn test. Statistical significance was considered at $p < 0.05$ for the Turkey test.

3.3 Results

3.3.1 Surface characterization of HA coated Mg miniscrews after TPA process

Figure 3-1 shows the surface characterization of the nmHA, mHA, nmHA+1G, mHA+1G, nmHA+2G, mHA+2G, nmHA+3G, and mHA+3G samples. The SEM images at low magnification (50x) show that the nmHA, nmHA+1G, nmHA+2G, nmHA+3G samples had agglomerates on their surfaces. In contrast, the surfaces of the mHA, mHA+1G, mHA+2G and mHA+3G samples were homogeneous, with few small visible agglomerates on the surfaces of the mHA+2G and mHA+3G samples. The SEM images at the magnifications of 500x and 5000x show cracks propagating through the surfaces of the mHA, mHA+1G, mHA+2G and mHA+3G samples. The SEM images at the magnification of 5000x shows that the nmHA, nmHA+1G, nmHA+2G and nmHA+3G samples had smaller particle size when compared with the mHA, mHA+1G, mHA+2G and mHA+3G samples. The EDS analyses (Figure 3-1b) confirmed the presence of Mg, Ca, P and O in the nmHA, mHA, mHA+1G, mHA+2G and mHA+3G, which are the composing elements of hydroxyapatite [$\text{Ca}_5(\text{PO}_4)_3(\text{OH})$].

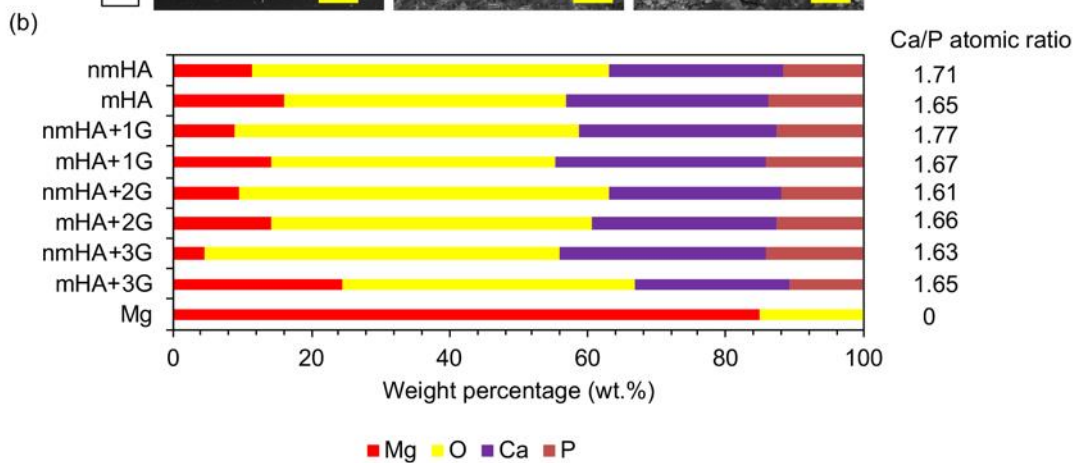
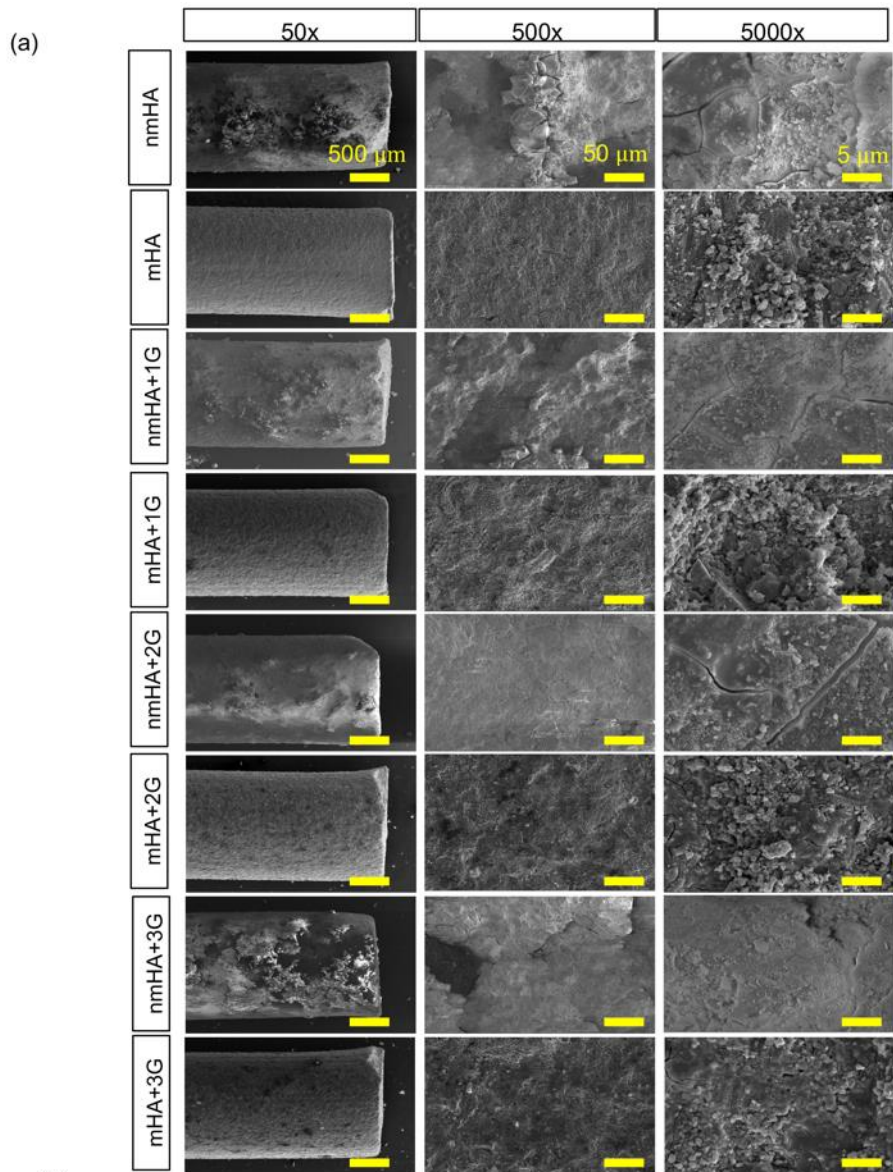


Figure 3-1: Surface characterization and elemental composition of nmHA, mHA, nmHA+1G, mHA+1G, nmHA+2G, mHA+2G nmHA+3G and mHA+3G. (a) SEM images of the samples at an original magnification of 50x (first column), 500 (second column), 5000x (third column). The scale bars equal to 500 μm , 50 μm and 5 μm , respectively. (b) surface elemental composition (wt.%) of the samples at 500x magnification.

3.3.2 BMSC morphology and density in direct contact and indirect contact with Mg mini-screws in direct culture *in vitro*

Figure 3-2a and b show the representative fluorescence images of BMSCs cultured with the nmHA, nmHA+1G, nmHA+2G, nmHA+3G, mHA, mHA+1G, mHA+2G, mHA+3G, controls of non-coated Mg and Ti, glass references and BMSC alone after 24 h of cell culture under direct contact and indirect contact. Under direct contact (Figure 3-2a), attached and viable BMSCs were observed in all groups and the cells show less spreading on the surfaces of HA coated Mg mini-screws when compared with the Ti and PMMA control, and glass reference. Under indirect contact (Figure 3-2b), the morphology of BMSCs surrounding the nmHA, nmHA+1G, nmHA+2G, nmHA+3G, mHA, mHA+1G, mHA+2G, mHA+3G, and Mg indicated normal growth and isotropic cell spreading when compared with the Ti and PMMA control, and glass reference.

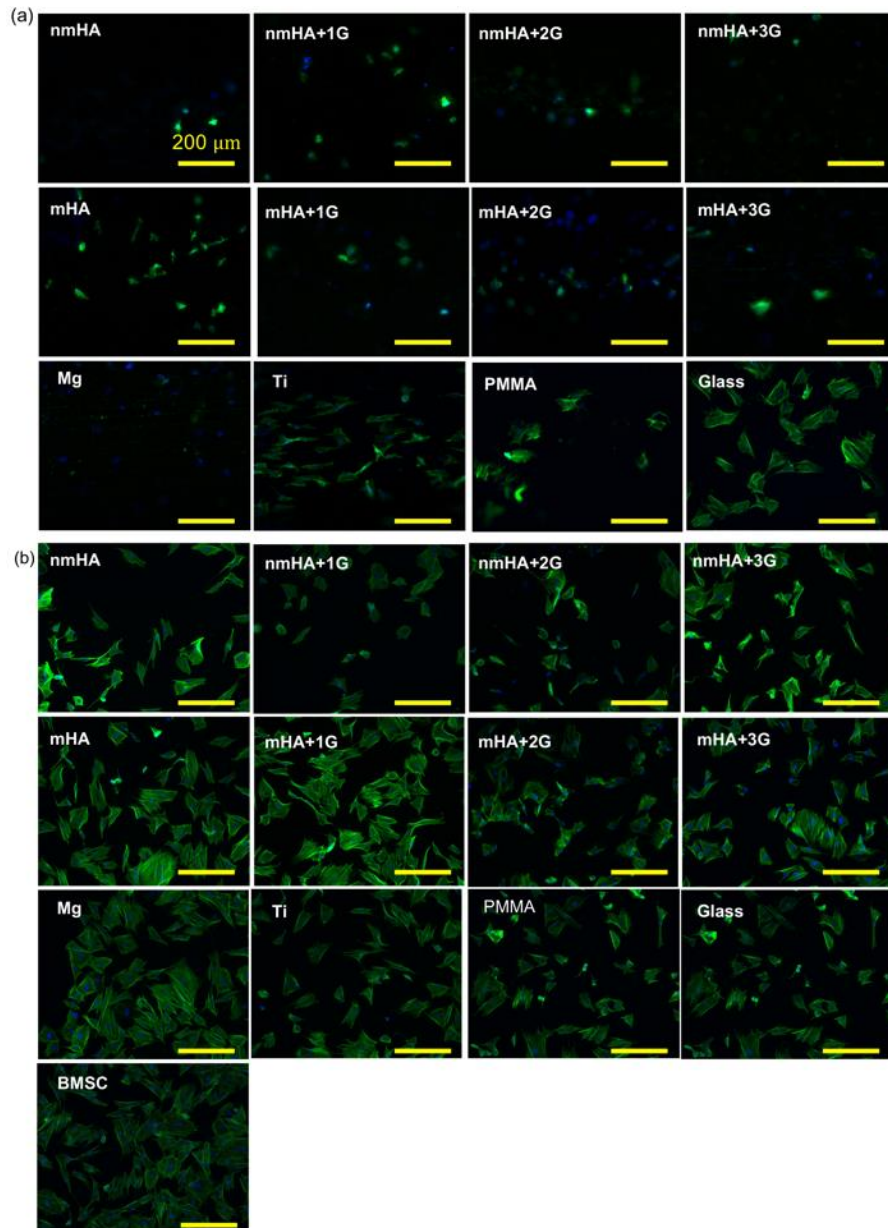


Figure 3-2: Fluorescence images of BMSCs under direct contact and indirect contact with the nmHA, nmHA+1G, nmHA+2G, nmHA+3G, mHA, mHA+1G, mHA+2G, mHA+3G, Mg, Ti and PMMA controls, glass reference and cell-only positive control (labeled as “BMSC”) after 24 h of direct culture. (a) representative fluorescence images of BMSCs adhered on the sample surfaces (direct contact), (b) representative fluorescence images of BMSCs on the tissue culture plates surrounding the samples (indirect contact). Green color indicates Alexa Fluor® 488-phalloidin stained F-actin (cytoskeleton) and blue color indicates DAPI stained nuclei. The images were taken at an original magnification of 10x with the scale bar = 200 μm.

The BMSC adhesion densities under direct and indirect contact with the HA coated Mg mini-screws, Mg, Ti and PMMA controls, glass reference and BMSC positive control are quantified and summarized in Figure 3-3. Figure 3-3a shows the BMSC adhesion density under direct contact with the samples after 24 h of cell culture. Kruskal Wallis was used to determine statistically significant differences in the cell adhesion density under direct contact because the data sets were non-parametric. The nmHA, nmHA+1G, nmHA+2G, nmHA+3G and Mg samples had significantly lower BMSC adhesion densities when compared with the glass reference. Kruskal Wallis confirmed a significantly lower BMSC adhesion density for nmHA, nmHA+1G, mHA+1G, nmHA+2G, nmHA+3G, mHA+3G and Mg when compared with Ti control under direct contact. No significant differences was found among all HA coated Mg samples. Figure 3-3b showed the BMSC adhesion density in direct contact with the samples after 24 h of cell culture. ANOVA was used to determine statistically significant differences in the cell adhesion density under indirect contact because the data sets were parametric. ANOVA confirmed a statistically significantly lower BMSC adhesion densities of nmHA, nmHA+1G, nmHA+2G when compared with the Mg control under indirect contact. The nmHA+2G had a significantly lower BMSC adhesion density than the mHA+1G, mHA+2G samples, glass reference and BMSCs only control.

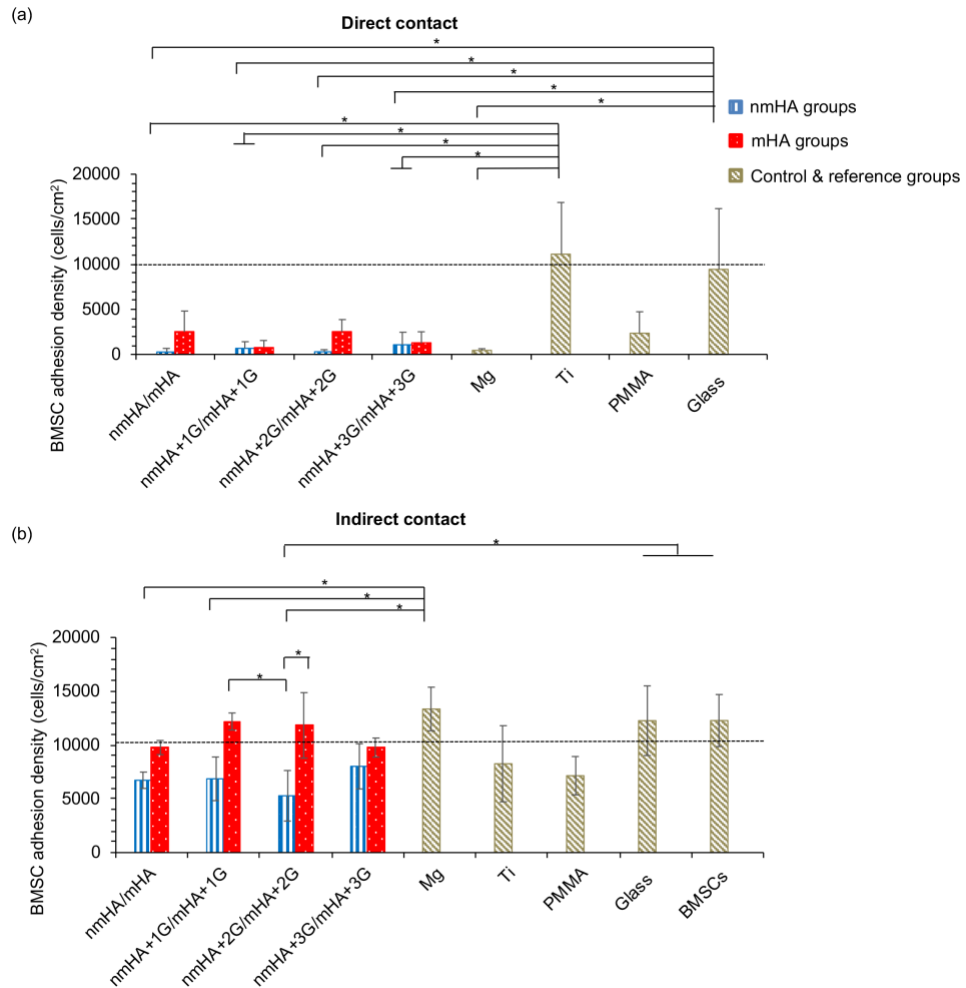


Figure 3-3: Adhesion density of BMSCs under direct and indirect contact with nmHA, nmHA+1G, nmHA+2G, nmHA+3G, mHA, mHA+1G, mHA+2G, mHA+3G, Mg, Ti and PMMA controls, glass reference and cell-only positive control (labeled as “BMSCs”) after 24 h of direct culture. (a) adhesion density of BMSCs under direct contact, (b) adhesion density of BMSCs under indirect contact. Values are mean \pm SD, n = 3; * p < 0.05.

3.3.3 Mass change and post-culture media analyses after 24-h cell culture

Figure 3-4 showed the ratio of final/initial dry mass ($\frac{M_f}{M_0}$) of all groups of samples and controls after 24 h of cell culture. All HA coated Mg samples and Mg control show mass gain after 24-h cell culture. ANOVA was used to determine the statistically

significant differences in the mean final/initial dry mass because the data sets were parametric. No statistically significant difference in the final/initial dry mass was found among all groups of samples.

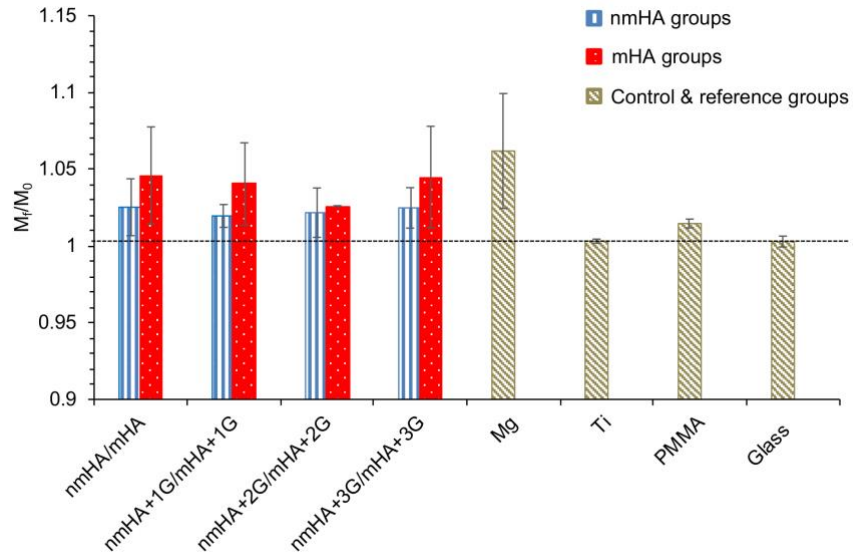


Figure 3-4: Mass change (ratio of final/initial dry mass M_f/M_0) for materials of interest after 24-h direct culture with BMSCs. Values are mean \pm SD of the means, $n = 3$; $*p < 0.05$.

Figure 3-5a shows the pH of the media of all groups of samples, controls and reference after 24 h of cell culture. One-way ANOVA was used to determine the statistically significant differences in the pH of the collected cultured media because the data sets were parametric. The pH of the nmHA and nmHA+1G were significantly higher than the mHA+1G, mHA+2G, Ti control, glass reference and DMEM. The measurements for Mg^{2+} and Ca^{2+} concentration are summarized in Figure 3-5b and c. Kruskal-Wallis method was used to determine the statistically significant differences in the $[Mg^{2+}]$ of the collected cultured media because the data sets were non-parametric. nmHA, nmHA+1G, nmHA+2G

and nmHA+3G had significantly higher $[Mg^{2+}]$ than the Ti and PMMA controls, glass reference, BMSC and DMEM after 24 h of cell culture. mHA, mHA+2G and mHA+3G had significantly higher $[Mg^{2+}]$ than the Ti control. The $[Mg^{2+}]$ in the culture media of the nmHA and nmHA+1G were significantly higher when compared with the non-coated Mg control. The $[Mg^{2+}]$ in the culture media of the nmHA sample was significantly higher than the mHA and mHA+1G. One-way ANOVA was used to determine the statistically significant differences in the $[Ca^{2+}]$ of the collected cultured media because the data sets were parametric. The $[Ca^{2+}]$ in the culture media of the nmHA, nmHA+1G, nmHA+2G, nmHA+3G, mHA, mHA+1G, mHA+2G samples were significantly lower than the non-coated Mg, Ti, PMMA controls, glass reference, BMSC and DMEM. The $[Ca^{2+}]$ in the culture media of the mHA+3G sample was significantly lower than the glass reference. Among the HA-coated Mg samples, the mHA, mHA+1G and mHA+2G samples had significantly higher $[Ca^{2+}]$ than the nmHA, nmHA+1G, nmHA+2G, nmHA+3G samples, but had significantly lower $[Ca^{2+}]$ than the mHA+3G. The $[Ca^{2+}]$ in the media of the mHA+3G sample was significantly higher than the nmHA, nmHA+1G, nmHA+2G, nmHA+3G samples.

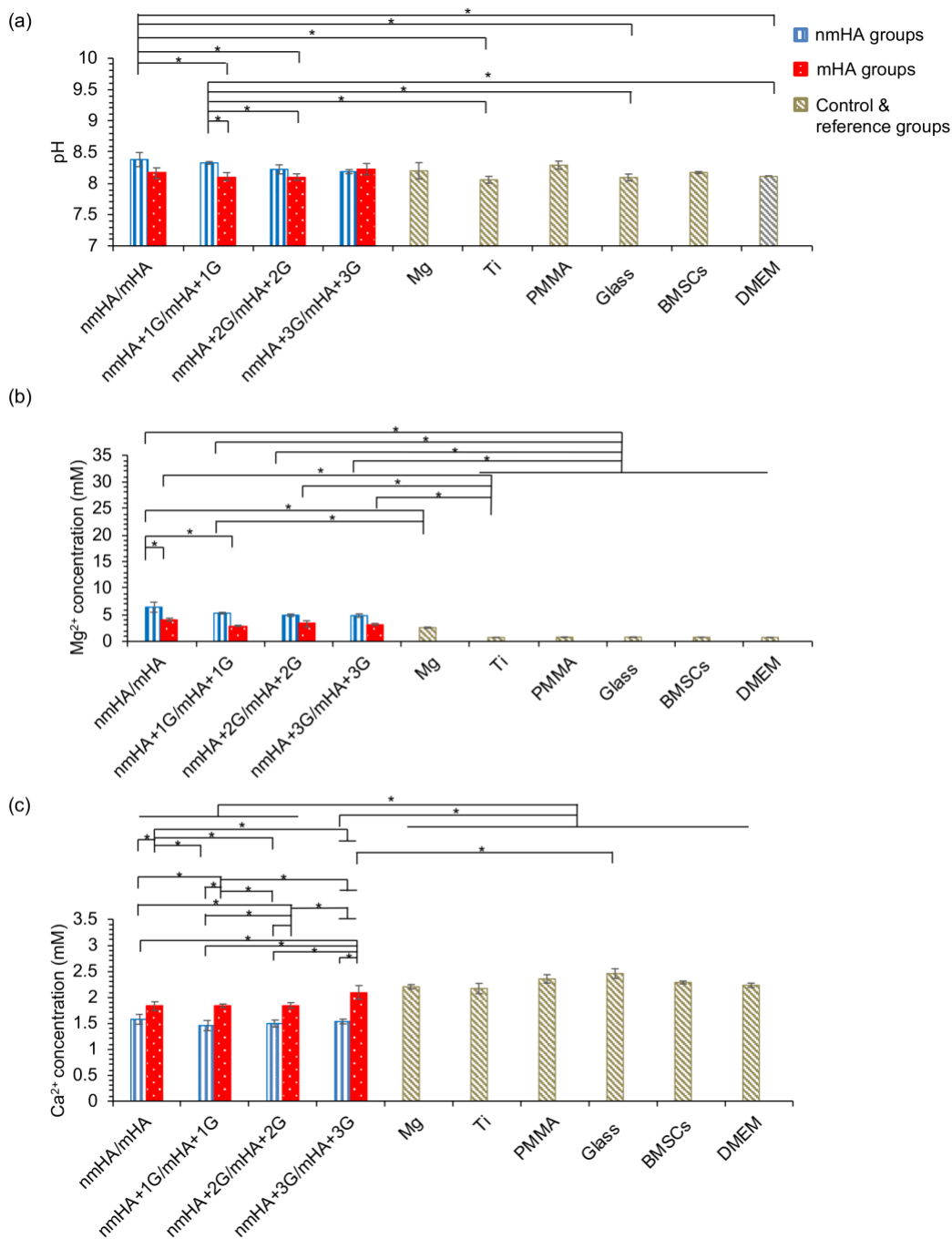


Figure 3-5: Analysis of pH and ionic concentrations in the culture media at 24 h of direct culture with the nmHA, nmHA+1G, nmHA+2G, nmHA+3G, mHA, mHA+1G, mHA+2G, mHA+3G, Mg, Ti and PMMA controls, glass reference and BMSCs positive control, and blank DMEM media. (a) pH of media, (b) Mg²⁺ ion concentration, (c) Ca²⁺ ion concentration. Values are mean \pm SD, n = 3. * p < 0.05.

3.3.4 Bacterial adhesion and viability of the HA coated Mg mini-screws

The bacterial density in the culture media and adhered on the surfaces of samples were both counted using CFU method and summarized in Figure 3-6. ANOVA was used to determine the statistically significant differences in the CFUs from the culture media because the data sets were parametric. For bacteria from the culture media, the CFUs of the nmHA, nmHA+1G, nmHA+2G, nmHA+3G, mHA+1G, mHA+2G, mHA+3G samples were significantly lower than the Mg, Ti and PMMA controls and glass reference. The CFUs of the mHA sample was significantly lower than the Mg control, but was significantly higher than the nmHA, nmHA+1G, nmHA+2G, nmHA+3G mHA+1G, mHA+2G, mHA+3G samples. The CFUs of the nmHA+1G, nmHA+2G, nmHA+3G, mHA+2G, mHA+3G samples were significantly lower than the *S. aureus* positive control. Among the HA coated Mg mini-screws, ANOVA confirmed that the nmHA, nmHA+1G, nmHA+2G, nmHA+3G samples had a significantly higher CFUs than the mHA+3G sample. The CFUs of the nmHA and nmHA+1G were significantly higher than the mHA+2G. Among the nmHA coated Mg samples, ANOVA confirmed a significantly higher CFUs of the nmHA sample than the nmHA+1G sample. Among the mHA coated Mg samples, the mHA+1G sample had a significantly higher CFUs when compared with the mHA+2G and mHA+3G samples. Furthermore, the mHA+2G had a significantly higher CFUs than the mHA+3G sample.

The statistically significant differences in the CFUs adhered on the surfaces of the samples were analyzed using one-way ANOVA because the data sets were parametric. ANOVA confirmed significantly lower CFUs of the nmHA, nmHA, nmHA+1G,

nmHA+2G, nmHA+3G, mHA, mHA+1G, mHA+2G, mHA+3G, non-coated Mg control than Ti, PMMA controls and glass reference.

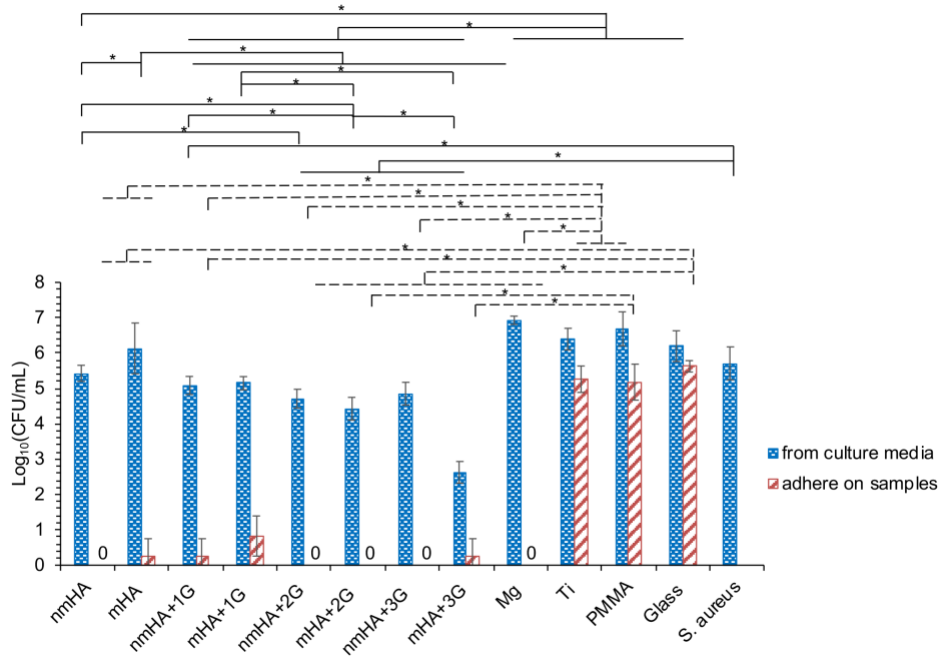


Figure 3-6: Bacteria density from the culture media and adhered on materials of interest after they cultured in rSFB+10%FBS for 24 h, as quantified from the colony forming units (CFUs). (a) Bacteria density from the culture media cultured with the materials of interest. (b) Bacteria density adhered on the surfaces of materials of interest. The initial seeding density was 3.6×10^6 CFU/mL. The materials of interest were cultured with *S. aureus* in 0.233 mL of r-SBF+10%FBS. Data are mean \pm SD, n=3; * $p < 0.05$.

3.3.5 Post-culture media analyses after 24-h bacterial culture

Figure 3-7a shows the pH of the r-SBF with 10% FBS for bacterial culture. ANOVA was used to determine the statistically significant differences in the pH of the media after 24 h of bacterial culture, because the datasets were parametric. It was found that the pH of the media cultured with the nmHA, nmHA+1G, nmHA+2G, nmHA+3G, mHA, mHA+1G, mHA+2G, mHA+3G samples were significantly higher than the Ti,

PMMA control, glass and r-SBF reference and *S. aureus* positive control. The pH of the media cultured with the nmHA, nmHA+1G, nmHA+2G, nmHA+3G, mHA+2G and mHA+3G samples were significantly higher than the Mg control. The pH of the media cultured with the nmHA, nmHA+1G, nmHA+2G, nmHA+3G samples were significantly higher than the mHA and mHA+2G samples. The media cultured with the nmHA, nmHA+1G, nmHA+2G, nmHA+3G and mHA+3G samples had significantly higher pH than the mHA+1G sample. The Mg²⁺ and Ca²⁺ concentrations of the media after 24 h of bacterial culture were summarized in Figure 3-7b and Figure 3-7c, respectively. Kruskal-Wallis method was to determine the statistically significant differences in the Mg²⁺ concentration because the data sets were non-parametric. For the Mg²⁺ concentration of the media cultured with the HA coated Mg mini-screws, the mHA+1G sample had a significantly lower Mg²⁺ concentration than the nmHA+3G and mHA+3G samples. The Mg²⁺ concentration of the media cultured with the nmHA, nmHA+1G, nmHA+2G, nmHA+3G and mHA+3G samples were significantly higher than the glass reference, *S. aureus* control and r-SBF. The Mg²⁺ concentration of the media cultured with the nmHA, nmHA+2G, nmHA+3G and mHA+3G samples were significantly higher than the Ti and PMMA controls. The Mg²⁺ concentration of the media cultured with the nmHA+3G and mHA+3G samples were significantly higher than the *S. aureus* control and r-SBF. The statistically significant differences in the Ca²⁺ concentration was analyzed using the Kruskal-Wallis method because the data sets were non-parametric. The Ca²⁺ concentration of the media cultured with the nmHA, nmHA+1G, nmHA+2G, nmHA+3G and mHA+3G samples were significantly lower than the Ti, PMMA control and glass reference. The Ca²⁺

concentration of the media cultured with the nmHA+1G, nmHA+2G and nmHA+3G samples were significantly lower than the *S. aureus* positive control and r-SBF. The Ca²⁺ concentration of the media cultured with the nmHA and mHA+3G samples were significantly lower than the r-SBF. For the Ca²⁺ concentration of the media cultured with the HA coated Mg mini-screws, the mHA+2G sample had significantly higher Ca²⁺ concentration when compared with the nmHA, nmHA+1G, nmHA+2G, nmHA+3G and mHA+3G samples.

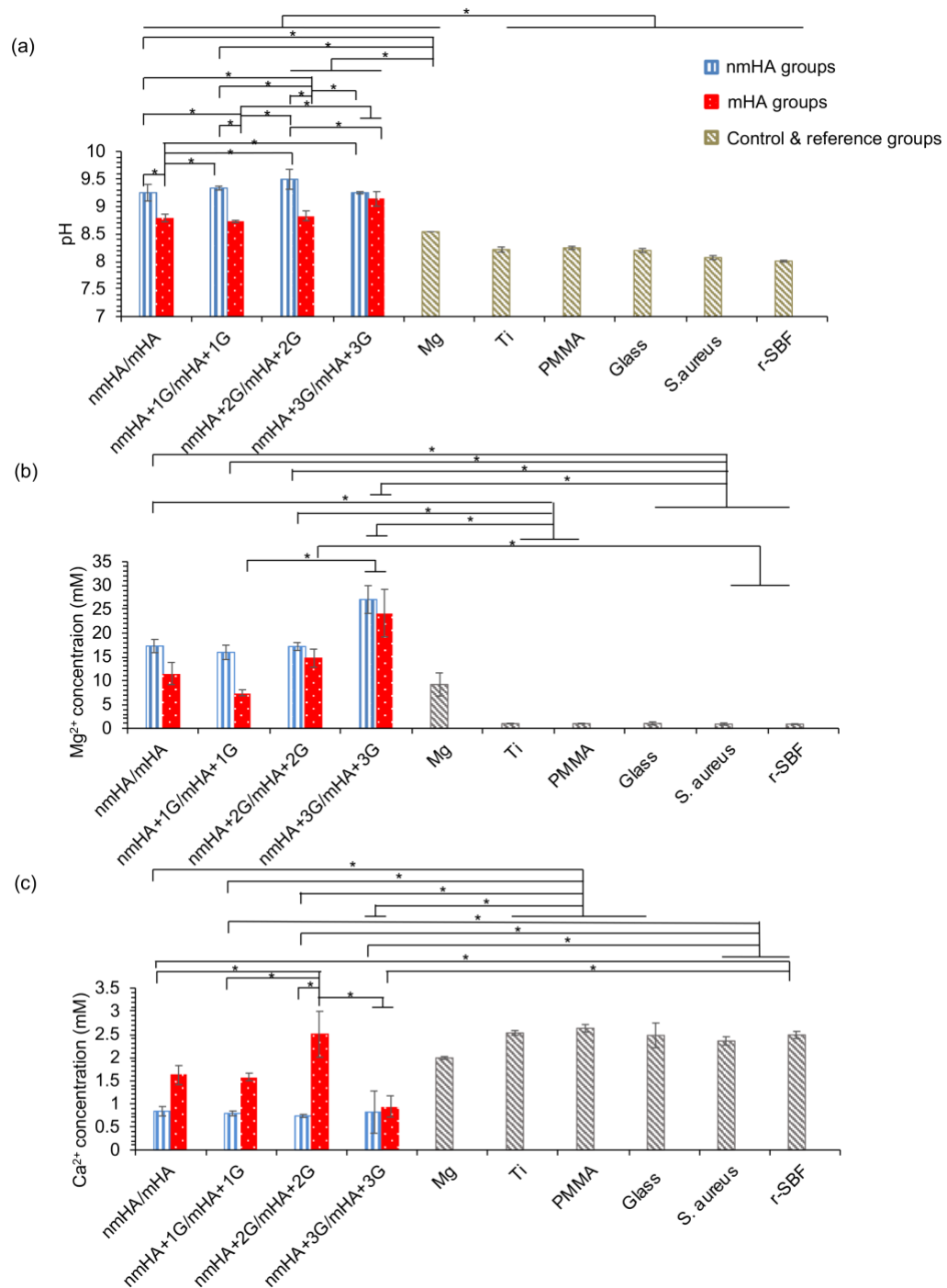


Figure 3-7: Analysis of pH and ionic concentrations in the media of the nmHA, nmHA+1G, nmHA+2G, nmHA+3G, mHA, mHA+1G, mHA+2G, mHA+3G, Mg, Ti and PMMA controls, glass reference and *S. aureus* positive control, and blank r-SBF. (a) pH of media, (b) Mg²⁺ ion concentration, (c) Ca²⁺ ion concentration. Values are mean \pm SD, n = 3; *p < 0.05.

3.3.6 Degradation properties (qualitative analyses) of HA coated Mg miniscrews

after 12-week immersion study

Figure 3-8 shows the microscopic images of the nmHA, mHA, mHA+1G, mHA+2G, mHA+3G and non-coated Mg samples at each prescribed time point during the 12 weeks of immersion in r-SBF. It is visible that small white crystal started to form on the surfaces of the nmHA, mHA, mHA+1G, mHA+2G, mHA+3G samples and Mg control at day 1 of immersion. At day 3 of immersion, the mHA, mHA+2G, mHA+3G samples and Mg control started to lose their regular shape, whereas the nmHA and mHA+1G samples started to lose their regular shape at day 5 of immersion. As the immersion time extended, more white crystals grown on the surface of the HA-coated Mg mini-screws and Mg control. All samples were fully covered with white crystals at 7 days of immersion. Mg showed the most accumulation of the white crystals on its surface at the end of the 12 weeks of immersion.

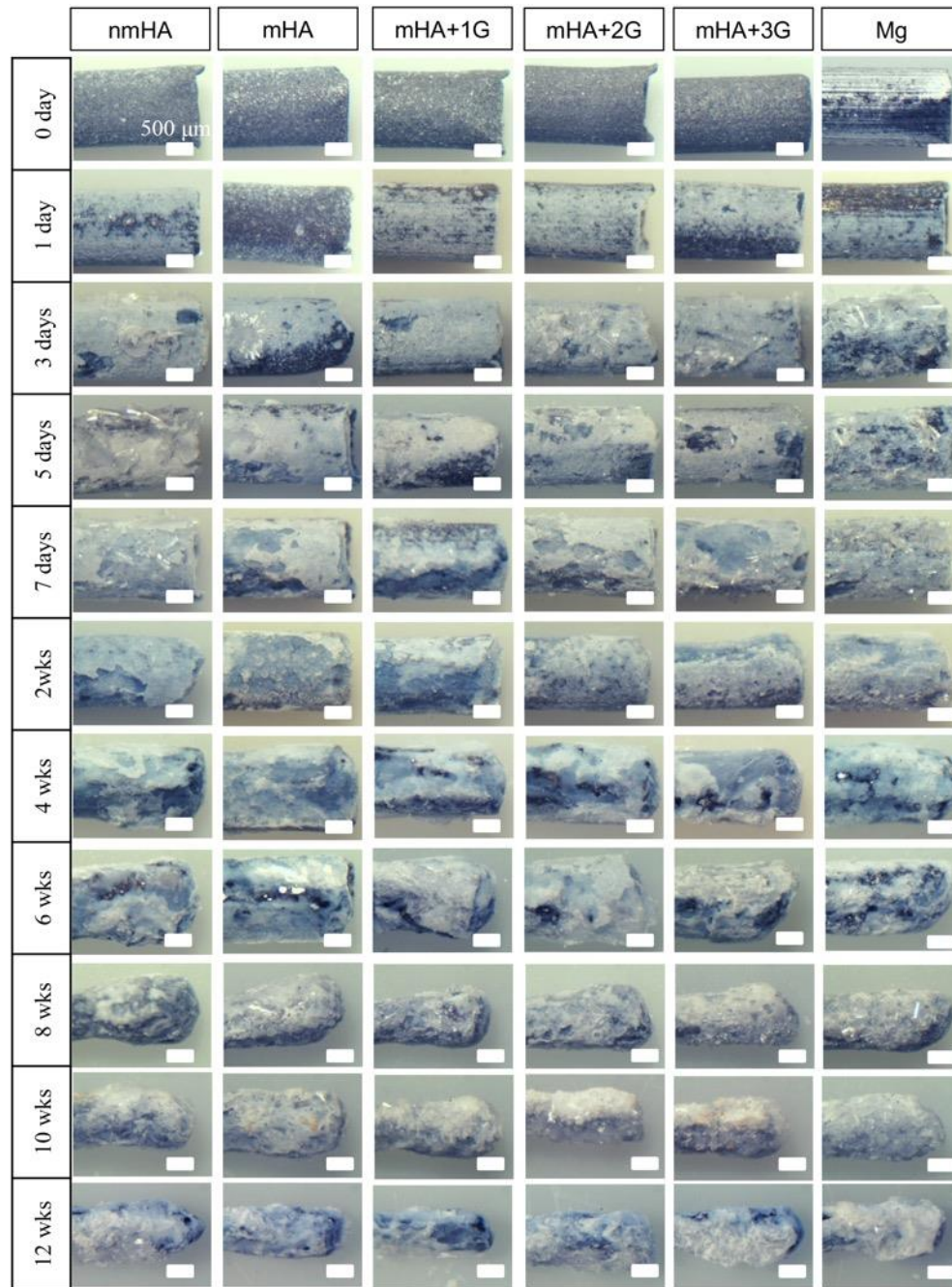


Figure 3-8: Macroscopic images of nmHA, mHA, mHA+1G, mHA+2G, mHA+3G and non-coated Mg control at each prescribed time point during 12 weeks of immersion in r-SBF. The scale bar was 500 μm for all images. The samples before immersion is shown in 0-day row.

The surface morphology and elemental composition were characterized after 12 weeks of immersion using SEM/EDS, as shown in Figure 3-9. No cracks were found on the surface of the nmHA, mHA, mHA+1G, mHA+2G, mHA+3G and non-coated Mg samples (Figure 3-9a,b,c,d,e,f), which could be ascribed to the full coverage of the non-soluble degradation products. The EDS analyses in Figure 3-9g shows the presence of Mg, Ca, P, O and C in all the HA-coated Mg mini-screws and non-coated Mg control. The mHA+3G had a higher Ca/P atomic ratio when compared with the nmHA, mHA, mHA+1G, mHA+2G samples and Mg control. The percentages of Ca and P in the mHA+3G sample increased was higher than other samples, indicating higher Ca/P depositions or a better preservation of the HA coating during the immersion. Figure 3-10 shows the XRD spectra for the nmHA, mHA, mHA+1G, mHA+2G, mHA+3G samples and Mg control after 12 weeks of immersion in r-SBF. The phases were identified according to the standards in the Inorganic Crystal Structure Database (ICSD): 02-020-0669 for $\text{MgCO}_3 \cdot 3\text{H}_2\text{O}$, 00-033-0878 for $\text{Mg}_3(\text{PO}_4)_2 \cdot 8\text{H}_2\text{O}$ and 01-086-0174 for CaCO_3 . The XRD spectra confirmed the deposition of $\text{MgCO}_3 \cdot 3\text{H}_2\text{O}$, $\text{Mg}_3(\text{PO}_4)_2 \cdot 8\text{H}_2\text{O}$ and CaCO_3 on surface of all the HA coated Mg mini-screws and Mg control, which in agreement with the detection of Mg, C, P, O and C elements for all the samples from the EDS analyses.

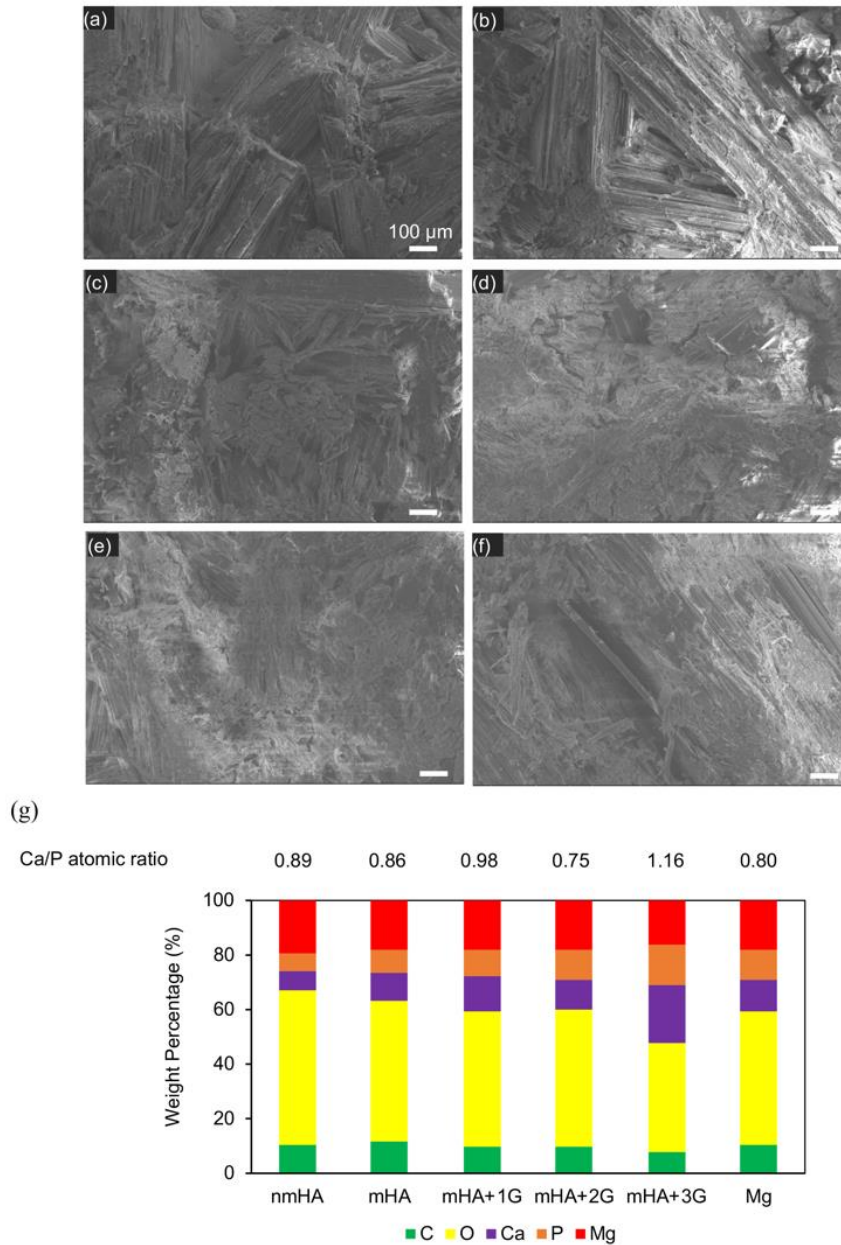


Figure 3-9: Surface morphology and elemental composition of material of interest. (a) nmHA, (b) mHA, (c) mHA+1G, (d) mHA+2G, (e) mHA+3G and (f) Mg control after 12 weeks immersion in r-SBF. The original magnifications for all SEM images were 200x, scale bar =100 μ m. (g) surface elemental composition (wt.%) of nmHA, mHA, mHA+1G, mHA+2G, mHA+3G and non-coated Mg control at 200x magnification.

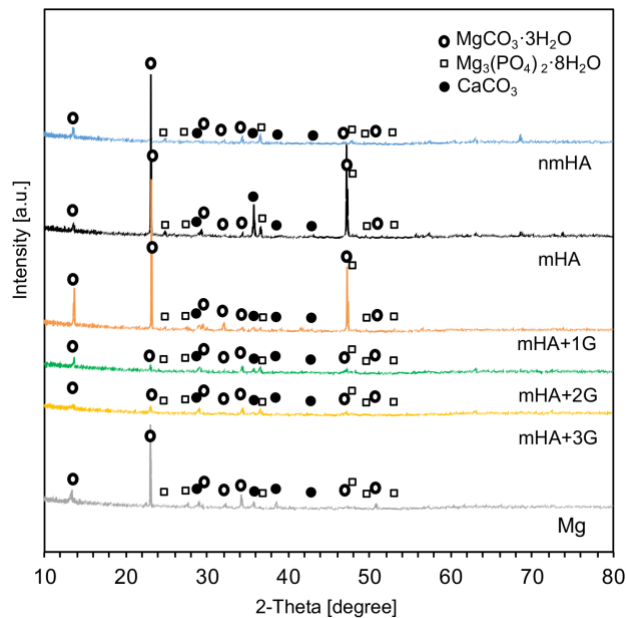


Figure 3-10: XRD spectra of the degradation layers on the surface of all samples after immersion in r-SBF for 12 weeks. Phases were identified based on $\text{MgCO}_3 \cdot 3\text{H}_2\text{O}$ (ICSD pattern 00-020-0669), $\text{Mg}_3(\text{PO}_4)_2 \cdot 8\text{H}_2\text{O}$ (ICSD pattern 00-033-0878) and CaCO_3 (ICSD pattern 01-086-0174).

3.3.7 Degradation properties (quantitative analyses) of HA coated Mg mini-screws after immersion in r-SBF

The ratios of final mass/initial mass ($\frac{M_f}{M_0}$) of the HA coated Mg mini-screws and Mg control are shown in Figure 3-11a, where M_f means the final dried mass of each sample at each prescribed time point and M_0 means the initial dried mass of each sample at 0 h before the immersion study. nmHA, mHA, mHA+1G, mHA+2G had mass gain after 1 day and 3 days of immersion, while mass loss was found after 5 days of immersion. The mHA had a mass loss at all prescribed time points. the non-coated Mg control showed a mass gain at 1 day, 3 days and 5 days of immersion and a mass loss after 1 weeks of immersion.

nmHA and non-coated Mg had the least mass loss, followed by the order of mHA, mHA+3G, mHA+2G and mHA+1G. It was found that mHA+1G had the most mass loss, with only 30% mass remained after 12 weeks of immersion. Loading gentamicin was found to accelerating the mass loss of nmHA because more mass loss was occurred for mHA with gentamicin when compared with mHA along (without gentamicin). nmHA showed the least mass loss, with 36% mass remained at 12 weeks.. When the amount of gentamicin was increased from 10 wt. % to 30 wt. %, the mass loss of mHA coated Mg decreased. From Figure 3-11a, mass loss of nmHA+1G was higher than nmHA+2G, while mass loss of nmHA+2G was larger than nmHA_3G.

Figure 3-11b shows the increase of pH for the post-cultured media at each prescribed time points. All groups of sample and control show that increase in pH after immersion in r-SBF. At 1 day of immersion, Kruskal-Wallis method confirms a significantly lower increased of pH in the media cultured with the nmHA sample than the Mg control. At 5 days of immersion, the increase of pH in the media cultured with the mHA+1G sample was significantly lower than the mHA+3G sample and Mg control. At 2 weeks of immersion, the increase of pH in the media cultured with the nmHA sample was significantly lower than the mHA+2G sample. At 3 weeks of immersion, the increase of pH in the media cultured with the nmHA sample was significantly higher than the mHA+1G. At 4 weeks of immersion, the increase of pH in the media cultured with the nmHA sample was significantly higher than the mHA+3G sample. At 5 weeks of immersion, the increase of pH in the media cultured with the nmHA sample was significantly lower than mHA+2G, mHA+3G and Mg control. The increase of pH in the

media cultured with the mHA+1G sample was significantly lower than the mHA+2G and mHA+3G samples. At 6 weeks of immersion, the increase of pH in the media cultured with the mHA+3G sample was significantly lower than the mHA sample. At 7 weeks of immersion, the increase of pH in the media cultured with the mHA+1G sample was significantly lower than the mHA+3G sample. No significant differences were found among all groups of samples at 3 days, 1 week and 8 weeks of immersion.

The ionic concentration analyses, i.e., Mg^{2+} , Ca^{2+} concentration, are shown in Figure 3-11c and Figure 3-11d, respectively. For Mg^{2+} concentration in the post-culture media, no significant difference was found among all group of samples at each prescribed time points. For Ca^{2+} concentration in the post-culture media at 1 day of immersion, no significant differences were found among all group of samples. At 3 days of immersion, the Ca^{2+} concentration in media cultured with the mHA sample was significantly lower than the mHA+3G sample. At 5 days of immersion, the Ca^{2+} concentration in media cultured with the mHA sample was significantly lower than the mHA+1G and mHA+3G samples. At 7 days of immersion, the Ca^{2+} concentration in media cultured with the mHA sample was significantly lower than the nmHA, mHA+1G, mHA+2G, mHA+3G samples and Mg control. The Ca^{2+} concentration in media cultured with the mHA+2G and mHA+3G samples were significantly lower than the Mg control. At 2 weeks of immersion, the Ca^{2+} concentration in media cultured with the nmHA sample was significantly higher than the mHA, mHA+1G, mHA+2G samples and Mg control. The Ca^{2+} concentration in media cultured with the mHA sample was significantly lower than the mHA+1G, mHA+3G samples and Mg control. The Ca^{2+} concentration in media cultured with the mHA+2G

sample was significantly lower than the mHA+1G, mHA+3G samples and Mg control. At 6 weeks of immersion, the Ca^{2+} concentration in media cultured with the mHA+3G sample was significantly lower than the mHA+1G and mHA+2G samples. The Ca^{2+} concentration in media cultured with the mHA+2G sample was significantly higher than the Mg control. At 8 weeks of immersion, the Ca^{2+} concentration in media cultured with the nmHA sample was significantly higher than the mHA sample and Mg control. The Ca^{2+} concentration in media cultured with the mHA sample and Mg control were significantly lower than the mHA+1G and mHA+2G samples. At 10 weeks of immersion, the Ca^{2+} concentration in media cultured with the nmHA sample was significantly higher than the mHA, mHA+2G samples and Mg control. The Ca^{2+} concentration in media cultured with the mHA sample was significantly lower than the mHA+1G and mHA+3G samples. The Ca^{2+} concentration in media cultured with the mHA+3G sample was significantly lower than the mHA+2G sample and Mg control. At 12 weeks of immersion, the Ca^{2+} concentration in media cultured with the nmHA sample was significantly higher than the mHA sample and Mg control. The Ca^{2+} concentration in media cultured with the mHA sample was significantly lower than the mHA+1G and mHA+2G samples. The Ca^{2+} concentration in media cultured with the mHA+2G sample was significantly higher than the Mg control. No significant differences of the Ca^{2+} concentration in the media was found among all groups of samples at 1 days and 4 weeks of immersion.

Figure 3-11e and f show the average daily degradation rates for the HA coated Mg samples and Mg controls normalized by their initial volume (V_0) and initial surface area (SA_0), respectively. The average daily degradation rates were calculated based on the

measured Mg^{2+} concentrations in the post-culture media (r-SBF) ¹⁷². No significant differences of the average daily degradation rates rate relative to V_0 and SA_0 was found among all groups of samples.

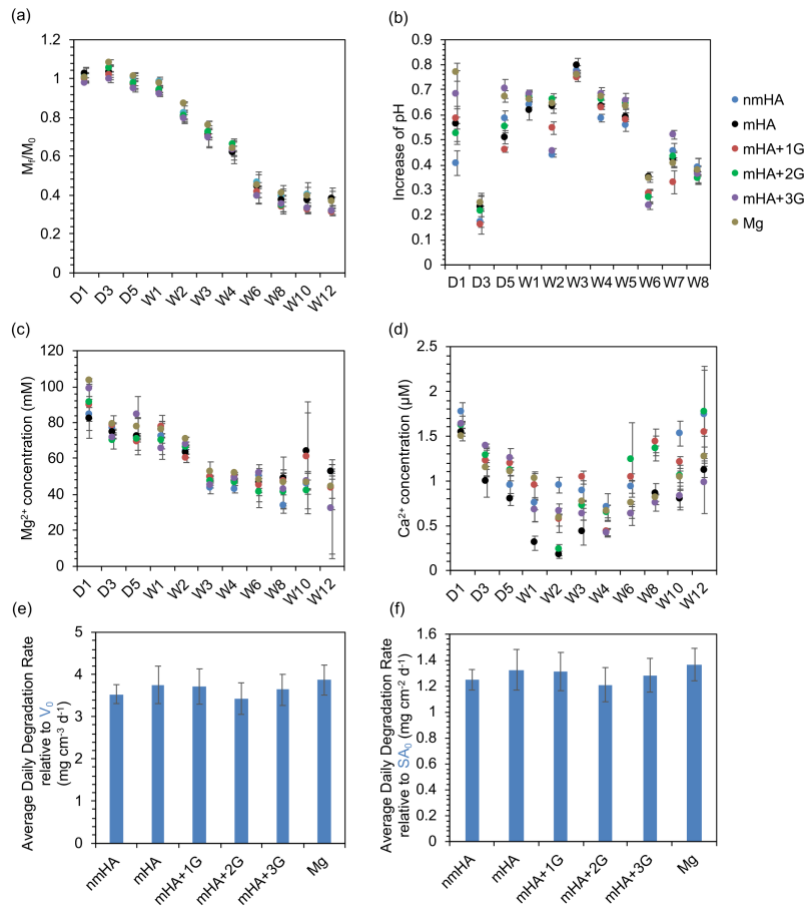


Figure 3-11: The degradation properties of materials of interest when they were immerse in r-SBF. (a) Mass change (the ratio of final/initial dry mass M_f/M_0) (b) Increase of pH (c) Mg^{2+} ion concentration, (d) Ca^{2+} ion concentration, (e) average daily degradation rate relative to the initial volume (V_0) of the mini-screws, (f) average daily degradation rate relative to the initial surface area (SA_0) of the mini-screws. Values are mean \pm SD, $n = 3$ at all time points. * $p < 0.05$.

3.4 Discussion

3.4.1 Degradation properties of the HA-coated Mg mini-screws

Surface characterization of the mHA coatings suggested that the addition of gentamicin (i.e., mHA+1G, mHA+2G, mHA+3G) induced a few agglomerates in the coating layers when compared with the mHA coated Mg without gentamicin that provided a more homogeneous distribution of HA particles. Additionally, depositing nHA particles on top of mHA coating layers induced agglomerates and micro-cracks in the nmHA coating layers (i.e., nmHA, nmHA+1G, nmHA+2G, nmHA+3G). From the post-culture media analyses after 24-h cell culture and bacterial culture, the pH and $[\text{Mg}^{2+}]$ in the culture media of the nmHA coated Mg samples were higher than the mHA coated Mg samples, which could be caused by the agglomerates and micro-cracks on the surfaces of the nmHA coated Mg samples that allow the penetration of aggressive ions in the media to attack the underlying Mg and accelerated the degradation. Therefore, the nmHA sample was selected as a representative for the nmHA coated Mg samples for long term immersion study. The degradation behaviors of the HA coated Mg samples were studied via qualitative analysis of the samples and quantitative analysis of the post-cultured media (r-SBF) at each prescribed time points. The micro-scale surface for the samples during 12-week of immersion shows no apparent difference at each prescribed time points, all lost their structural integrity since 3 days of immersion in r-SBF. The average daily degradation rates for the HA coated Mg samples and Mg control was calculated from the Mg^{2+} concentration in post-culture media (r-SBF) and normalized by the initial volume (V_0) and initial surface area (SA_0). No significant differences was found among all HA coated Mg samples..

3.4.2 Cytocompatibility of the HA-coated Mg mini-screws

In the direct culture method, the nmHA coated Mg samples (i.e., nmHA, nmHA+1G, nmHA+2G, nmHA+3G) shows lower BMSC adhesion density in average than the mHA coated Mg samples under direct contact, possibly because of the higher localized alkalinity and the more agglomerates in the coating layers. In addition, adding gentamicin to the HA coating layers did not have significant effects on the BMSC adhesion and morphology as compared with the nmHA and mHA samples under direct contact. This suggests that the presence of gentamicin in the HA coatings did not interfere the *in vitro* BMSC responses under direct contact.

Under indirect contact, the solubilized degradation products released by the HA coated Mg did not affect the BMSC morphology. The nmHA coated Mg samples shows lower BMSC adhesion density in average than the mHA coated Mg samples under indirect contact, possibly because the higher pH in the media cause by the agglomerates and microcracks in the nmHA coating layers. In addition, adding gentamicin to the HA coating layers did not have significant effects on the BMSC adhesion and morphology when compared with the nmHA and mHA samples under indirect contact. This suggests that the presence of gentamicin in the HA coating layers did not interfere the *in vitro* BMSC responses under indirect contact.

3.4.3 Antimicrobial properties of the HA-coated Mg mini-screws against *S. aureus*

In terms of the viability of *S. aureus* adhered on the surfaces, all HA coated Mg samples and Mg control have antimicrobial effects against *S. aureus* because their CFUs were significantly lower than the Ti, PMMA controls and glass references. But no apparent

difference in the CFUs adhered on the surfaces was found among the HA coated Mg samples and Mg control. For the viability of *S. aureus* from the culture media, all HA coated Mg samples except for the mHA coated Mg sample showed inhibitory effects on the growth of *S. aureus* when compared with the Mg Ti, PMMA controls and glass references. More importantly, the nmHA sample showed significantly lower CFUs from its culture media when compared with the Mg control, which was in agreement with our previous study that showed similar effects of the nHA sample [*unpublished*]. To our best knowledge, very few papers reported the antimicrobial properties of HA nanoparticles. Ge et al. reported a lower average CFUs of *S. aureus* of the HA coated Ti sample when compared with the Ti control.¹⁷³ Baskar et al.¹⁷⁴ reported the antimicrobial property of HA nanoparticles at a concentration of 370.7 $\mu\text{g/mL}$ for 24 h of incubation and investigated its antimicrobial mechanism. Through the measurement of lactate dehydrogenase in the culture media and observation of the surface of the bacteria under TEM, it was found that the HA nanoparticles caused the cell/membrane damage of *S. aureus*.¹⁷⁴

For the viability of *S. aureus* from the culture media, loading gentamicin into the mHA coating layers enhanced its antimicrobial effects against *S. aureus* during 24 h of culture. When the contents of gentamicin in the mHA coating layers increased (i.e., from 0 to 30 wt. %), the CFU of *S. aureus* from the culture media decreased. The mHA + 3G sample had the best antimicrobial effect against *S. aureus*.

3.4.4 HA coated Mg for biomedical applications

In this study, loading gentamicin into the mHA coating layers could guarantee superior degradation properties and cytocompatibility despite very small agglomerates

produced in the coating layers. No significant differences in the degradation rates and BMSC adhesion under direct/indirect contact was found among the mHA+xG ($x = 1, 2, 3$) samples. The deposition of nHA layers onto the mHA coated Mg mini-screws induced micro-cracks and agglomerates in the nmHA coating layers, which could lead to inferior degradation performance and BMSC response when compared with mHA coated Mg mini-screws.

Moreover, the antimicrobial properties of the mHA coated Mg samples was enhanced when the contents of gentamicin increased from 0 wt. % to 30 wt. %. Therefore, the collective properties (i.e., degradation, cytocompatibility, antimicrobial properties) of the mHA coated Mg loaded with 30 wt. % gentamicin indicated its great potential for implant applications. In the future, the mHA coated Mg loaded with 30 wt.% gentamicin will be studied *in vivo* to elucidate its effects on tissue regeneration and bacterial infections.

3.5 Conclusions

In this study, largely homogeneous mHA coatings loaded with gentamicin were created onto the Mg miniscrews, while visible microcracks and agglomerates were formed when nHA coating was applied onto the mHA coated Mg. No significant difference in the BMSC adhesion density under direct contact was found among the HA coated Mg samples and Mg control, but the HA coated Mg samples and Mg control showed reduced cell spreading under direct contact than the Ti and PMMA controls, and glass reference. Under indirect contact, the mHA coated Mg samples had higher BMSC adhesion density when compared with the nmHA coated Mg samples. Moreover, the antimicrobial properties of the mHA coated Mg against *S. aureus* from the culture media was enhanced

when increased content of gentamicin was loaded into the mHA coating layers, specifically, the mHA+3G sample showed the best antimicrobial effects against *S. aureus* from the culture media. The 12-week immersion study shows that the degradation rate among the mHA coated Mg samples and the nmHA sample, and Mg control were similar, without any significant differences. Collectively considering the cytocompatibility, antimicrobial properties and degradation properties, the mHA+3G sample are recommended for further *in vivo* experiments to elucidate its effects on tissue regeneration and bacterial infections.

References

- (1) Yelin, E.; Weinstein, S.; King, T. In *The burden of musculoskeletal diseases in the United States*, Seminars in arthritis and rheumatism, 2016; p 259.
- (2) Inzana, J. A.; Schwarz, E. M.; Kates, S. L.; Awad, H. A. Biomaterials approaches to treating implant-associated osteomyelitis. *Biomaterials* **2016**, *81*, 58-71.
- (3) Kremers, H. M.; Larson, D. R.; Crowson, C. S.; Kremers, W. K.; Washington, R. E.; Steiner, C. A.; Jiranek, W. A.; Berry, D. J. Prevalence of total hip and knee replacement in the United States. *The Journal of bone and joint surgery. American volume* **2015**, *97* (17), 1386.
- (4) Ducheyne, P. *Comprehensive biomaterials II*, Elsevier: 2017.
- (5) Darouiche, R. O. Treatment of infections associated with surgical implants. *N. Engl. J. Med.* **2004**, *350* (14), 1422-1429.
- (6) Campoccia, D.; Montanaro, L.; Arciola, C. R. The significance of infection related to orthopedic devices and issues of antibiotic resistance. *Biomaterials* **2006**, *27* (11), 2331-2339.
- (7) Trampuz, A.; Zimmerli, W. Diagnosis and treatment of infections associated with fracture-fixation devices. *Injury* **2006**, *37* (2), S59-S66.
- (8) Zimmerli, W.; Sendi, P. In *Pathogenesis of implant-associated infection: the role of the host*, Seminars in immunopathology, Springer: 2011; pp 295-306.
- (9) Stewart, P. S.; Costerton, J. W. Antibiotic resistance of bacteria in biofilms. *The lancet* **2001**, *358* (9276), 135-138.
- (10) Viswanathan, V., Off-label abuse of antibiotics by bacteria. Taylor & Francis: 2014.
- (11) Valstar, E. R.; Nelissen, R. G.; Reiber, J. H.; Rozing, P. M. The use of Roentgen stereophotogrammetry to study micromotion of orthopaedic implants. *ISPRS J. Photogramm.* **2002**, *56* (5-6), 376-389.
- (12) Gristina, A. G. Biomaterial-centered infection: microbial adhesion versus tissue integration. *Sci.* **1987**, *237* (4822), 1588-1595.
- (13) Johnson, C. T.; Wroe, J. A.; Agarwal, R.; Martin, K. E.; Guldberg, R. E.; Donlan, R. M.; Westblade, L. F.; García, A. J. Hydrogel delivery of lysostaphin eliminates orthopedic implant infection by *Staphylococcus aureus* and supports fracture healing. *Proceedings of the National Academy of Sciences* **2018**, *115* (22), E4960-E4969.

- (14) Cipriano, A. F.; Lin, J.; Lin, A.; Sallee, A.; Le, B.; Cortez Alcaraz, M. C.; Guan, R.-G.; Botimer, G.; Inceoğlu, S.; Liu, H. Degradation of Bioresorbable Mg–4Zn–1Sr Intramedullary Pins and Associated Biological Responses in Vitro and in Vivo. *ACS Appl. Mater. Interfaces* **2017**, *9* (51), 44332-44355.
- (15) Trumbo, P.; Schlicker, S.; Yates, A. A.; Poos, M. Dietary reference intakes for energy, carbohydrate, fiber, fat, fatty acids, cholesterol, protein and amino acids. *J. Acad. Nutr. Diet.* **2002**, *102* (11), 1621.
- (16) Song, M.-S.; Zeng, R.-C.; Ding, Y.-F.; Li, R. W.; Easton, M.; Cole, I.; Birbilis, N.; Chen, X.-B. Recent advances in biodegradation controls over Mg alloys for bone fracture management: a review. *J. Mater. Sci. Technol.* **2019**, *35* (4), 535-544.
- (17) Geetha, M.; Singh, A. K.; Asokamani, R.; Gogia, A. K. Ti based biomaterials, the ultimate choice for orthopaedic implants—a review. *Prog. Mater. Sci.* **2009**, *54* (3), 397-425.
- (18) Chen, Q.; Thouas, G. A. Metallic implant biomaterials. *Mater. Sci. Eng. R Rep.* **2015**, *87*, 1-57.
- (19) Hornberger, H.; Virtanen, S.; Boccaccini, A. Biomedical coatings on magnesium alloys—a review. *Acta Biomater.* **2012**, *8* (7), 2442-2455.
- (20) Riaz, U.; Shabib, I.; Haider, W. The current trends of Mg alloys in biomedical applications—A review. *J. Biomed. Mater. Res., Part B* **2019**, *107* (6), 1970-1996.
- (21) Zhao, D.; Witte, F.; Lu, F.; Wang, J.; Li, J.; Qin, L. Current status on clinical applications of magnesium-based orthopaedic implants: A review from clinical translational perspective. *Biomaterials* **2017**, *112*, 287-302.
- (22) Chen, Y.; Xu, Z.; Smith, C.; Sankar, J. Recent advances on the development of magnesium alloys for biodegradable implants. *Acta Biomater.* **2014**, *10* (11), 4561-4573.
- (23) Windhagen, H.; Radtke, K.; Weizbauer, A.; Diekmann, J.; Noll, Y.; Kreimeyer, U.; Schavan, R.; Stukenborg-Colsman, C.; Waizy, H. Biodegradable magnesium-based screw clinically equivalent to titanium screw in hallux valgus surgery: short term results of the first prospective, randomized, controlled clinical pilot study. *Biomed. Eng. Online* **2013**, *12* (1), 62.
- (24) Biber, R.; Pauser, J.; Brem, M.; Bail, H. J. Bioabsorbable metal screws in traumatology: a promising innovation. *Trauma Case Rep.* **2017**, *8*, 11-15.
- (25) Biber, R.; Pauser, J.; Geßlein, M.; Bail, H. J. Magnesium-based absorbable metal screws for intra-articular fracture fixation. *Case Rep. Orthop.* **2016**, *2016*, 9673174.

- (26) Han, P.; Cheng, P.; Zhang, S.; Zhao, C.; Ni, J.; Zhang, Y.; Zhong, W.; Hou, P.; Zhang, X.; Zheng, Y. In vitro and in vivo studies on the degradation of high-purity Mg (99.99 wt.%) screw with femoral intracondylar fractured rabbit model. *Biomaterials* **2015**, *64*, 57-69.
- (27) Huang, S.; Wang, B.; Zhang, X.; Lu, F.; Wang, Z.; Tian, S.; Li, D.; Yang, J.; Cao, F.; Cheng, L. High-purity weight-bearing magnesium screw: Translational application in the healing of femoral neck fracture. *Biomaterials* **2020**, *238*, 119829.
- (28) Zhao, D.; Huang, S.; Lu, F.; Wang, B.; Yang, L.; Qin, L.; Yang, K.; Li, Y.; Li, W.; Wang, W. Vascularized bone grafting fixed by biodegradable magnesium screw for treating osteonecrosis of the femoral head. *Biomaterials* **2016**, *81*, 84-92.
- (29) Han, H.-S.; Loffredo, S.; Jun, I.; Edwards, J.; Kim, Y.-C.; Seok, H.-K.; Witte, F.; Mantovani, D.; Glyn-Jones, S. Current status and outlook on the clinical translation of biodegradable metals. *Mater. Today* **2019**, *23*, 57-71.
- (30) Kumar, K.; Gill, R.; Batra, U. Challenges and opportunities for biodegradable magnesium alloy implants. *Mater. Technol.* **2018**, *33* (2), 153-172.
- (31) Poinern, G. E. J.; Brundavanam, S.; Fawcett, D. Biomedical magnesium alloys: a review of material properties, surface modifications and potential as a biodegradable orthopaedic implant. *Am. J. Biomed. Eng.* **2012**, *2* (6), 218-240.
- (32) Noviana, D.; Paramitha, D.; Ulum, M. F.; Hermawan, H. The effect of hydrogen gas evolution of magnesium implant on the postimplantation mortality of rats. *J. Orthop. Transl.* **2016**, *5*, 9-15.
- (33) Lee, J.-W.; Han, H.-S.; Han, K.-J.; Park, J.; Jeon, H.; Ok, M.-R.; Seok, H.-K.; Ahn, J.-P.; Lee, K. E.; Lee, D.-H. Long-term clinical study and multiscale analysis of in vivo biodegradation mechanism of Mg alloy. *Proc. Natl. Acad. Sci.* **2016**, *113* (3), 716-721.
- (34) Abisegapriyan, K.; Rajeshwari, A.; Kundu, S.; Subramanian, B. Magnesium glassy alloy laminated nanofibrous polymer as biodegradable scaffolds. *J. Non-Cryst. Solids* **2018**, *502*, 210-217.
- (35) Jia, Z.; Xiu, P.; Xiong, P.; Zhou, W.; Cheng, Y.; Wei, S.; Zheng, Y.; Xi, T.; Cai, H.; Liu, Z. Additively manufactured macroporous titanium with silver-releasing micro-/nanoporous surface for multipurpose infection control and bone repair—a proof of concept. *ACS Appl. Mater. Interfaces* **2016**, *8* (42), 28495-28510.
- (36) Oliveira, W.; Silva, P.; Silva, R.; Silva, G.; Machado, G.; Coelho, L.; Correia, M. Staphylococcus aureus and Staphylococcus epidermidis infections on implants. *J. Hosp. Infect.* **2018**, *98* (2), 111-117.

- (37) Raphael, J.; Holodniy, M.; Goodman, S. B.; Heilshorn, S. C. Multifunctional coatings to simultaneously promote osseointegration and prevent infection of orthopaedic implants. *Biomaterials* **2016**, *84*, 301-314.
- (38) Costerton, J. W.; Stewart, P. S.; Greenberg, E. P. Bacterial biofilms: a common cause of persistent infections. *Sci.* **1999**, *284* (5418), 1318-1322.
- (39) Hall-Stoodley, L.; Costerton, J. W.; Stoodley, P. Bacterial biofilms: from the natural environment to infectious diseases. *Nat. Rev. Microbiol.* **2004**, *2* (2), 95.
- (40) Sabaté Brescó, M.; Harris, L. G.; Thompson, K.; Stanic, B.; Morgenstern, M.; O'Mahony, L.; Richards, R. G.; Moriarty, T. F. Pathogenic mechanisms and host interactions in *Staphylococcus epidermidis* device-related infection. *Front. Microbiol.* **2017**, *8*, 1401.
- (41) Boles, B. R.; Horswill, A. R. Agr-mediated dispersal of *Staphylococcus aureus* biofilms. *PLoS Pathog.* **2008**, *4* (4), e1000052.
- (42) Arciola, C. R.; Campoccia, D.; Montanaro, L. Implant infections: adhesion, biofilm formation and immune evasion. *Nat. Rev. Microbiol.* **2018**, *16* (7), 397.
- (43) Otto, M. Staphylococcal biofilms. *Curr. Top. Microbiol. Immunol.* **2008**, *322*, 207-228.
- (44) Sawai, J.; Kojima, H.; Igarashi, H.; Hashimoto, A.; Shoji, S.; Sawaki, T.; Hakoda, A.; Kawada, E.; Kokugan, T.; Shimizu, M. Antibacterial characteristics of magnesium oxide powder. *World J. Microbiol. Biotechnol.* **2000**, *16* (2), 187-194.
- (45) Sawai, J. Quantitative evaluation of antibacterial activities of metallic oxide powders (ZnO, MgO and CaO) by conductimetric assay. *J. Microbiol. Methods* **2003**, *54* (2), 177-182.
- (46) Wetteland, C. L.; Nguyen, N.-Y. T.; Liu, H. Concentration-dependent behaviors of bone marrow derived mesenchymal stem cells and infectious bacteria toward magnesium oxide nanoparticles. *Acta Biomater.* **2016**, *35*, 341-356.
- (47) Nguyen, N.-Y. T.; Grelling, N.; Wetteland, C. L.; Rosario, R.; Liu, H. Antimicrobial Activities and Mechanisms of Magnesium Oxide Nanoparticles (nMgO) against Pathogenic Bacteria, Yeasts, and Biofilms. *Sci. Rep.* **2018**, *8* (1), 16260.
- (48) Hickey, D. J.; Muthusamy, D.; Webster, T. J. Electrophoretic deposition of MgO nanoparticles imparts antibacterial properties to poly-L-lactic acid for orthopedic applications. *J. Biomed. Mater. Res. A* **2017**, *105* (11), 3136-3147.

- (49) Ricker, A.; Liu-Snyder, P.; Webster, T. J. The influence of nano MgO and BaSO₄ particle size additives on properties of PMMA bone cement. *Int. J. Nanomed.* **2008**, *3* (1), 125.
- (50) Cipriano, A. F.; Lin, J.; Miller, C.; Lin, A.; Alcaraz, M. C. C.; Soria Jr, P.; Liu, H. Anodization of magnesium for biomedical applications—Processing, characterization, degradation and cytocompatibility. *Acta Biomater.* **2017**, *62*, 397-417.
- (51) Cortez Alcaraz, M. C.; Cipriano, A. F.; Lin, J.; Soria Jr, P.; Tian, Q.; Liu, H. Electrophoretic Deposition of Magnesium Oxide Nanoparticles on Magnesium: Processing Parameters, Microstructures, Degradation, and Cytocompatibility. *ACS Appl. Bio Mater.* **2019**, *2* (12), 5634-5652.
- (52) Lindström, R.; Johansson, L.-G.; Thompson, G. E.; Skeldon, P.; Svensson, J.-E. Corrosion of magnesium in humid air. *Corros. Sci.* **2004**, *46* (5), 1141-1158.
- (53) Handbook, A. S. Magnesium and magnesium alloys. In *ASM international*; Baker, M. A. a. H., Ed.; 1999; pp 106-118.
- (54) Nordlien, J. H.; Nisancioglu, K.; Ono, S.; Masuko, N. Morphology and structure of water-formed oxides on ternary MgAl alloys. *J. Electrochem. Soc.* **1997**, *144* (2), 461-466.
- (55) Miley, H. Fundamentals of oxidation and tarnish. *The corrosion handbook. New York: John Wiley* **1948**, 11-20.
- (56) Asami, K.; Ono, S. Quantitative X-Ray Photoelectron Spectroscopy Characterization of Magnesium Oxidized in Air. *J. Electrochem. Soc.* **2000**, *147* (4), 1408-1413.
- (57) Seyeux, A.; Liu, M.; Schmutz, P.; Song, G.; Atrens, A.; Marcus, P. ToF-SIMS depth profile of the surface film on pure magnesium formed by immersion in pure water and the identification of magnesium hydride. *Corros. Sci.* **2009**, *51* (9), 1883-1886.
- (58) Barchiche, C.-E.; Rocca, E.; Juers, C.; Hazan, J.; Steinmetz, J. Corrosion resistance of plasma-anodized AZ91D magnesium alloy by electrochemical methods. *Electrochim. Acta* **2007**, *53* (2), 417-425.
- (59) Gray, J.; Luan, B. Protective coatings on magnesium and its alloys—a critical review. *J. Alloys Compd.* **2002**, *336* (1-2), 88-113.
- (60) Zhu, Y.; Wu, G.; Zhang, Y.-H.; Zhao, Q. Growth and characterization of Mg (OH) 2 film on magnesium alloy AZ31. *Appl. Surf. Sci.* **2011**, *257* (14), 6129-6137.
- (61) Tian, P.; Liu, X. Surface modification of biodegradable magnesium and its alloys for biomedical applications. *Regener. Biomater.* **2015**, *2* (2), 135-151.

- (62) Li, B.; Gao, P.; Zhang, H.; Guo, Z.; Zheng, Y.; Han, Y. Osteoimmunomodulation, osseointegration, and in vivo mechanical integrity of pure Mg coated with HA nanorod/pore-sealed MgO bilayer. *Biomater. Sci.* **2018**, *6* (12), 3202-3218.
- (63) Wang, J.; Tang, J.; Zhang, P.; Li, Y.; Wang, J.; Lai, Y.; Qin, L. Surface modification of magnesium alloys developed for bioabsorbable orthopedic implants: a general review. *J. Biomed. Mater. Res., Part B* **2012**, *100* (6), 1691-1701.
- (64) Moreno, R.; Ferrari, B. Nanoparticles dispersion and the effect of related parameters in the EPD kinetics. In *Electrophoretic deposition of nanomaterials*; Springer: New York, 2012; pp 73-128.
- (65) Blawert, C.; Dietzel, W.; Ghali, E.; Song, G. Anodizing treatments for magnesium alloys and their effect on corrosion resistance in various environments. *Adv. Eng. Mater.* **2006**, *8* (6), 511-533.
- (66) JIS, Z.; Association, J. S. Antimicrobial products—Test for antimicrobial activity and efficacy. *Minister of International Trade Industry and Health Care* **2000**.
- (67) Zhang, C.; Lin, J.; Nguyen, N.-Y. T.; Guo, Y.; Xu, C.; Seo, C.; Villafana, E.; Jimenez, H.; Chai, Y.; Guan, R. Antimicrobial Bioresorbable Mg–Zn–Ca Alloy for Bone Repair in a Comparison Study with Mg–Zn–Sr Alloy and Pure Mg. *ACS Biomater. Sci. Eng.* **2019**.
- (68) Jiang, W.; Tian, Q.; Vuong, T.; Shashaty, M.; Gopez, C.; Sanders, T.; Liu, H. Comparison study on four biodegradable polymer coatings for controlling magnesium degradation and human endothelial cell adhesion and spreading. *ACS Biomater. Sci. Eng.* **2017**, *3* (6), 936-950.
- (69) Necula, B. S.; Fratila-Apachitei, L. E.; Zaat, S. A.; Apachitei, I.; Duszczuk, J. In vitro antibacterial activity of porous TiO₂–Ag composite layers against methicillin-resistant *Staphylococcus aureus*. *Acta Biomater.* **2009**, *5* (9), 3573-3580.
- (70) Necula, B.; Van Leeuwen, J.; Fratila-Apachitei, L.; Zaat, S.; Apachitei, I.; Duszczuk, J. J. A. b. In vitro cytotoxicity evaluation of porous TiO₂–Ag antibacterial coatings for human fetal osteoblasts. **2012**, *8* (11), 4191-4197.
- (71) Cleophas, R. T.; Sjollema, J.; Busscher, H. J.; Kruijtzter, J. A.; Liskamp, R. M. Characterization and activity of an immobilized antimicrobial peptide containing bactericidal PEG-hydrogel. *Biomacromolecules* **2014**, *15* (9), 3390-3395.
- (72) Schofield, W.; Badyal, J. A substrate-independent approach for bactericidal surfaces. *ACS Appl. Mater. Interfaces* **2009**, *1* (12), 2763-2767.

- (73) Francolini, I.; Donelli, G. Prevention and control of biofilm-based medical-device-related infections. *FEMS Immunol. Med. Microbiol.* **2010**, *59* (3), 227-238.
- (74) Gittens, R. A.; Scheideler, L.; Rupp, F.; Hyzy, S. L.; Geis-Gerstorfer, J.; Schwartz, Z.; Boyan, B. D. A review on the wettability of dental implant surfaces II: Biological and clinical aspects. *Acta Biomater.* **2014**, *10* (7), 2907-2918.
- (75) Lei, T.; Ouyang, C.; Tang, W.; Li, L.-F.; Zhou, L.-S. Preparation of MgO coatings on magnesium alloys for corrosion protection. *Surf. Coat. Technol.* **2010**, *204* (23), 3798-3803.
- (76) Lei, T.; Ouyang, C.; Tang, W.; Li, L.-F.; Zhou, L.-S. Enhanced corrosion protection of MgO coatings on magnesium alloy deposited by an anodic electrodeposition process. *Corros. Sci.* **2010**, *52* (10), 3504-3508.
- (77) Wenzel, R. N. Resistance of solid surfaces to wetting by water. *Ind. Eng. Chem.* **1936**, *28* (8), 988-994.
- (78) Mel'gunov, M. S.; Fenelonov, V. B.; Mel'gunova, E. A.; Bedilo, A. F.; Klabunde, K. J. Textural changes during topochemical decomposition of nanocrystalline Mg (OH) 2 to MgO. *J. Phys. Chem. B* **2003**, *107* (11), 2427-2434.
- (79) Johnson, I.; Lin, J.; Liu, H. Surface Modification and Coatings for Controlling the Degradation and Bioactivity of Magnesium Alloys for Medical Applications. In *Orthopedic Biomaterials*; Springer: New York, 2017; pp 331-363.
- (80) Gawlik, M. M.; Wiese, B.; Desharnais, V.; Ebel, T.; Willumeit-Römer, R. The Effect of Surface Treatments on the Degradation of Biomedical Mg Alloys—A Review Paper. *Mater.* **2018**, *11* (12), 2561.
- (81) Wang, S.; Lacefield, W. R.; Lemons, J. E. Interfacial shear strength and histology of plasma sprayed and sintered hydroxyapatite implants in vivo. *Biomaterials* **1996**, *17* (20), 1965-1970.
- (82) Feng, J.; Chen, Y.; Liu, X.; Liu, T.; Zou, L.; Wang, Y.; Ren, Y.; Fan, Z.; Lv, Y.; Zhang, M. In-situ hydrothermal crystallization Mg (OH) 2 films on magnesium alloy AZ91 and their corrosion resistance properties. *Mater. Chem. Phys.* **2013**, *143* (1), 322-329.
- (83) Yang, Y.-C.; Chang, E. Influence of residual stress on bonding strength and fracture of plasma-sprayed hydroxyapatite coatings on Ti-6Al-4V substrate. *Biomaterials* **2001**, *22* (13), 1827-1836.
- (84) Gnedenkov, S.; Khrisanfova, O.; Zavidnaya, A.; Sinebryukhov, S.; Egorkin, V.; Nistratova, M.; Yerokhin, A.; Matthews, A. PEO coatings obtained on an Mg-Mn type

- alloy under unipolar and bipolar modes in silicate-containing electrolytes. *Surf. Coat. Technol.* **2010**, *204* (14), 2316-2322.
- (85) Srinivasan, P. B.; Liang, J.; Blawert, C.; Störmer, M.; Dietzel, W. Characterization of calcium containing plasma electrolytic oxidation coatings on AM50 magnesium alloy. *Appl. Surf. Sci.* **2010**, *256* (12), 4017-4022.
- (86) Durdu, S.; Usta, M. Characterization and mechanical properties of coatings on magnesium by micro arc oxidation. *Appl. Surf. Sci.* **2012**, *261*, 774-782.
- (87) Mandelli, A.; Bestetti, M.; Da Forno, A.; Lecis, N.; Trasatti, S.; Trueba, M. A composite coating for corrosion protection of AM60B magnesium alloy. *Surf. Coat. Technol.* **2011**, *205* (19), 4459-4465.
- (88) Aktuğ, S. L.; Durdu, S.; Kutbay, I.; Usta, M. Effect of $\text{Na}_2\text{SiO}_3 \cdot 5\text{H}_2\text{O}$ concentration on microstructure and mechanical properties of plasma electrolytic oxide coatings on AZ31 Mg alloy produced by twin roll casting. *Ceram. Int.* **2016**, *42* (1), 1246-1253.
- (89) Robinson, D. A.; Griffith, R. W.; Shechtman, D.; Evans, R. B.; Conzemius, M. G. In vitro antibacterial properties of magnesium metal against *Escherichia coli*, *Pseudomonas aeruginosa* and *Staphylococcus aureus*. *Acta Biomater.* **2010**, *6* (5), 1869-1877.
- (90) Sawai, J.; Ishizu, N.; Itoh, M. Kinetic analysis of the bactericidal action of magnesium oxide powder slurry against *Escherichia coli*. *Biocontrol Sci.* **2003**, *8* (3), 123-127.
- (91) Anićić, N.; Vukomanović, M.; Koklic, T.; Suvorov, D. Fewer Defects in the Surface Slows the Hydrolysis Rate, Decreases the ROS Generation Potential, and Improves the Non-ROS Antimicrobial Activity of MgO. *Small* **2018**, *14* (26), 1800205.
- (92) Ribeiro, M.; Monteiro, F. J.; Ferraz, M. P. Infection of orthopedic implants with emphasis on bacterial adhesion process and techniques used in studying bacterial-material interactions. *Biomater* **2012**, *2* (4), 176-194.
- (93) Dizaj, S. M.; Lotfipour, F.; Barzegar-Jalali, M.; Zarrintan, M. H.; Adibkia, K. Antimicrobial activity of the metals and metal oxide nanoparticles. *Materials Science & Engineering: C* **2014**, *44*, 278-284.
- (94) Das, B.; Moumita, S.; Ghosh, S.; Khan, M. I.; Indira, D.; Jayabalan, R.; Tripathy, S. K.; Mishra, A.; Balasubramanian, P. Biosynthesis of magnesium oxide (MgO) nanoflakes by using leaf extract of *Bauhinia purpurea* and evaluation of its antibacterial property against *Staphylococcus aureus*. *Mater. Sci. Eng. C* **2018**, *91*, 436-444.

- (95) Clements, M. O.; Watson, S. P.; Foster, S. J. Characterization of the major superoxide dismutase of *Staphylococcus aureus* and its role in starvation survival, stress resistance, and pathogenicity. *J. Bacteriol.* **1999**, *181* (13), 3898-3903.
- (96) Karavolos, M. H.; Horsburgh, M. J.; Ingham, E.; Foster, S. J. Role and regulation of the superoxide dismutases of *Staphylococcus aureus*. *Microbiology* **2003**, *149* (10), 2749-2758.
- (97) Abdal Dayem, A.; Hossain, M. K.; Lee, S. B.; Kim, K.; Saha, S. K.; Yang, G.-M.; Choi, H. Y.; Cho, S.-G. The role of reactive oxygen species (ROS) in the biological activities of metallic nanoparticles. *Int. J. Mol. Sci.* **2017**, *18* (1), 120.
- (98) Nel, A.; Xia, T.; Mädler, L.; Li, N. Toxic potential of materials at the nanolevel. *Sci.* **2006**, *311* (5761), 622-627.
- (99) Fu, P. P.; Xia, Q.; Hwang, H.-M.; Ray, P. C.; Yu, H. Mechanisms of nanotoxicity: generation of reactive oxygen species. *J. Food Drug Anal.* **2014**, *22* (1), 64-75.
- (100) Reading, N. C.; Sperandio, V. Quorum sensing: the many languages of bacteria. *FEMS Microbiol. Lett.* **2006**, *254* (1), 1-11.
- (101) Sifri, C. D. Quorum sensing: bacteria talk sense. *Clinical infectious diseases* **2008**, *47* (8), 1070-1076.
- (102) Czárán, T.; Hoekstra, R. F. Microbial communication, cooperation and cheating: quorum sensing drives the evolution of cooperation in bacteria. *PloS one* **2009**, *4* (8), e6655.
- (103) MacKintosh, E. E.; Patel, J. D.; Marchant, R. E.; Anderson, J. M. Effects of biomaterial surface chemistry on the adhesion and biofilm formation of *Staphylococcus epidermidis* in vitro. *J. Biomed. Mater. Res., Part A* **2006**, *78* (4), 836-842.
- (104) Andrade, J.; Hlady, V. Protein adsorption and materials biocompatibility: a tutorial review and suggested hypotheses. In *Biopolymers/Non-Exclusion HPLC*; Springer: New York, 1986; pp 1-63.
- (105) Wilson, C. J.; Clegg, R. E.; Leavesley, D. I.; Percy, M. J. Mediation of biomaterial–cell interactions by adsorbed proteins: a review. *Tissue Eng.* **2005**, *11* (1-2), 1-18.
- (106) Reith, G.; Schmitz-Greven, V.; Hensel, K. O.; Schneider, M. M.; Tinschmann, T.; Bouillon, B.; Probst, C. Metal implant removal: benefits and drawbacks—a patient survey. *BMC surgery* **2015**, *15* (1), 96.

- (107) Saris, N. E. 60 Mervaala, H. Karppanen, JA Khawaja and A. Lewenstam. *Clin. Chem. Acta* **2000**, 294, 1.
- (108) Hiromoto, S.; Yamamoto, A. Control of degradation rate of bioabsorbable magnesium by anodization and steam treatment. *Materials Science and Engineering: C* **2010**, 30 (8), 1085-1093.
- (109) Wang, J.; Witte, F.; Xi, T.; Zheng, Y.; Yang, K.; Yang, Y.; Zhao, D.; Meng, J.; Li, Y.; Li, W. Recommendation for modifying current cytotoxicity testing standards for biodegradable magnesium-based materials. *Acta biomaterialia* **2015**, 21, 237-249.
- (110) Kraus, T.; Fischerauer, S. a. c. hanzi, P. j. Uggowitz, j. F. löffler, a. m. Weinberg. *Acta Biomater* **2012**, 8, 1230.
- (111) Zberg, B.; Uggowitz, P. J.; Löffler, J. F. MgZnCa glasses without clinically observable hydrogen evolution for biodegradable implants. *Nature materials* **2009**, 8 (11), 887-891.
- (112) Guarner, F.; Malagelada, J.-R. Gut flora in health and disease. *The Lancet* **2003**, 361 (9356), 512-519.
- (113) Viswanathan, V. Off-label abuse of antibiotics by bacteria. *Gut Microbes* **2014**, 5 (1), 3-4.
- (114) Radha, R.; Sreekanth, D. Insight of magnesium alloys and composites for orthopedic implant applications—a review. *J Journal of magnesium and alloys* **2017**, 5 (3), 286-312.
- (115) Cipriano, A. F.; Sallee, A.; Guan, R.-G.; Zhao, Z.-Y.; Tayoba, M.; Sanchez, J.; Liu, H. Investigation of magnesium–zinc–calcium alloys and bone marrow derived mesenchymal stem cell response in direct culture. *Acta biomaterialia* **2015**, 12, 298-321.
- (116) Zhang, S.; Zhang, X.; Zhao, C.; Li, J.; Song, Y.; Xie, C.; Tao, H.; Zhang, Y.; He, Y.; Jiang, Y. Research on an Mg–Zn alloy as a degradable biomaterial. *Acta biomaterialia* **2010**, 6 (2), 626-640.
- (117) Song, G. Control of biodegradation of biocompatible magnesium alloys. *Corrosion science* **2007**, 49 (4), 1696-1701.
- (118) Zhang, B.; Wang, Y.; Geng, L. Research on Mg-Zn-Ca Alloy as Degradable Biomaterial, w: Biomaterials–Physics and Chemistry. *InTech, Croatia* **2011**.
- (119) Li, Z.; Gu, X.; Lou, S.; Zheng, Y. The development of binary Mg–Ca alloys for use as biodegradable materials within bone. *Biomaterials* **2008**, 29 (10), 1329-1344.

- (120) Marie, P. Strontium ranelate: a physiological approach for optimizing bone formation and resorption. *Bone* **2006**, *38* (2), 10-14.
- (121) Guan, R.; Cipriano, A. F.; Zhao, Z.; Lock, J.; Tie, D.; Zhao, T.; Cui, T.; Liu, H. Development and evaluation of a magnesium–zinc–strontium alloy for biomedical applications—Alloy processing, microstructure, mechanical properties, and biodegradation. *Mater. Sci. Eng. C* **2013**, *33* (7), 3661-3669.
- (122) Cipriano, A. F.; Zhao, T.; Johnson, I.; Guan, R.-G.; Garcia, S.; Liu, H. In vitro degradation of four magnesium–zinc–strontium alloys and their cytocompatibility with human embryonic stem cells. *J. Mater. Sci.: Mater. Med.* **2013**, *24* (4), 989-1003, DOI: 10.1007/s10856-013-4853-1.
- (123) Cipriano, A. F.; Sallee, A.; Tayoba, M.; Alcaraz, M. C. C.; Lin, A.; Guan, R.; Zhao, Z.; Liu, H. Cytocompatibility and early inflammatory response of human endothelial cells in direct culture with Mg-Zn-Sr alloys. *Acta Biomaterialia* **2017**, *48*, 499-520.
- (124) Cipriano, A. F.; Sallee, A.; Guan, R.-G.; Lin, A.; Liu, H. A comparison study on the degradation and cytocompatibility of Mg-4Zn-x Sr alloys in direct culture. *ACS Biomater. Sci. Eng.* **2017**, *3* (4), 540-550.
- (125) Hornberger, H.; Virtanen, S.; Boccaccini, A. R. Biomedical coatings on magnesium alloys—a review. *Acta biomaterialia* **2012**, *8* (7), 2442-2455.
- (126) Lin, J.; Nguyen, N.-Y. T.; Zhang, C.; Ha, A.; Liu, H. H. Antimicrobial properties of MgO nanostructures on magnesium substrates. *ACS omega* **2020**, *5* (38), 24613-24627.
- (127) Johnson, I.; Wang, S. M.; Silken, C.; Liu, H. A systemic study on key parameters affecting nanocomposite coatings on magnesium substrates. *Acta biomaterialia* **2016**, *36*, 332-349.
- (128) Coulthard, M. G.; Kalra, M.; Lambert, H. J.; Nelson, A.; Smith, T.; Perry, J. D. Redefining urinary tract infections by bacterial colony counts. *Pediatrics* **2010**, *125* (2), 335-341.
- (129) Fosmire, G. J. Zinc toxicity. *The American journal of clinical nutrition* **1990**, *51* (2), 225-227.
- (130) Sheikh, M. S.; Santa Ana, C. A.; Nicar, M. J.; Schiller, L. R.; Fordtran, J. S. Gastrointestinal absorption of calcium from milk and calcium salts. *New England Journal of Medicine* **1987**, *317* (9), 532-536.
- (131) Roh, J.-L.; Park, C. I. Routine oral calcium and vitamin D supplements for prevention of hypocalcemia after total thyroidectomy. *The American journal of surgery* **2006**, *192* (5), 675-678.

- (132) Marie, P.; Ammann, P.; Boivin, G.; Rey, C. Mechanisms of action and therapeutic potential of strontium in bone. *Calcified tissue international* **2001**, *69* (3).
- (133) Winek, C.; Buehler, E. J. T.; pharmacology, a. Intravenous toxicity of zinc pyridinethione and several zinc salts. *Toxicology and applied pharmacology* **1966**, *9* (2), 269-273.
- (134) Kroes, R.; Den Tonkelaar, E.; Minderhoud, A.; Speijers, G.; Vonk-Visser, D.; Berkvens, J.; Van Esch, G. Short-term toxicity of strontium chloride in rats. *Toxicology* **1977**, *7* (1), 11-21.
- (135) Cha, P.-R.; Han, H.-S.; Yang, G.-F.; Kim, Y.-C.; Hong, K.-H.; Lee, S.-C.; Jung, J.-Y.; Ahn, J.-P.; Kim, Y.-Y.; Cho, S.-Y. Biodegradability engineering of biodegradable Mg alloys: Tailoring the electrochemical properties and microstructure of constituent phases. *Scientific reports* **2013**, *3* (1), 1-6.
- (136) Lei, T.; Ouyang, C.; Tang, W.; Li, L.-F.; Zhou, L.-S. Enhanced corrosion protection of MgO coatings on magnesium alloy deposited by an anodic electrodeposition process. *Corrosion science* **2010**, *52* (10), 3504-3508.
- (137) Lei, T.; Ouyang, C.; Tang, W.; Li, L.-F.; Zhou, L.-S. Preparation of MgO coatings on magnesium alloys for corrosion protection. *Surface and Coatings Technology* **2010**, *204* (23), 3798-3803.
- (138) Amin, S.; Achenbach, S. J.; Atkinson, E. J.; Khosla, S.; Melton III, L. J. Trends in fracture incidence: a population-based study over 20 years. *Journal of Bone and Mineral Research* **2014**, *29* (3), 581-589.
- (139) Trumbo, P.; Schlicker, S.; Yates, A. A.; Poos, M. Dietary reference intakes for energy, carbohydrate, fiber, fat, fatty acids, cholesterol, protein and amino acids. *Journal of the Academy of Nutrition and Dietetics* **2002**, *102* (11), 1621.
- (140) Geetha, M.; Singh, A. K.; Asokamani, R.; Gogia, A. K. Ti based biomaterials, the ultimate choice for orthopaedic implants—a review. *Progress in materials science* **2009**, *54* (3), 397-425.
- (141) Chen, Q.; Thouas, G. A. Metallic implant biomaterials. *Materials Science and Engineering: R: Reports* **2015**, *87*, 1-57.
- (142) Hornberger, H.; Virtanen, S.; Boccaccini, A. Biomedical coatings on magnesium alloys—a review. *Acta Biomater.* **2012**, *8* (7), 2442-2455.
- (143) Staiger, M. P.; Pietak, A. M.; Huadmai, J.; Dias, G. Magnesium and its alloys as orthopedic biomaterials: a review. *Biomaterials* **2006**, *27* (9), 1728-1734.

- (144) Zeng, R.; Dietzel, W.; Witte, F.; Hort, N.; Blawert, C. Progress and challenge for magnesium alloys as biomaterials. *Advanced Engineering Materials* **2008**, *10* (8), B3-B14.
- (145) Kraus, T.; Fischerauer, S. F.; Hänzi, A. C.; Uggowitzer, P. J.; Löffler, J. F.; Weinberg, A. M. Magnesium alloys for temporary implants in osteosynthesis: in vivo studies of their degradation and interaction with bone. *Acta biomaterialia* **2012**, *8* (3), 1230-1238.
- (146) Rüedi, T. P.; Buckley, R.; Moran, C. G. AO principles of fracture management. *Ann R Coll Surg Engl* **2009**, *91* (5), 448-9.
- (147) Gustilo, R. B.; Merkow, R. L.; Templeman, D. The management of open fractures. *JBJS* **1990**, *72* (2), 299-304.
- (148) Jia, Z.; Xiu, P.; Xiong, P.; Zhou, W.; Cheng, Y.; Wei, S.; Zheng, Y.; Xi, T.; Cai, H.; Liu, Z. Additively manufactured macroporous titanium with silver-releasing micro-/nanoporous surface for multipurpose infection control and bone repair—a proof of concept. *ACS applied materials & interfaces* **2016**, *8* (42), 28495-28510.
- (149) Zhou, H.; Lee, J. Nanoscale hydroxyapatite particles for bone tissue engineering. *Acta biomaterialia* **2011**, *7* (7), 2769-2781.
- (150) Kim, S. M.; Jo, J. H.; Lee, S. M.; Kang, M. H.; Kim, H. E.; Estrin, Y.; Lee, J. H.; Lee, J. W.; Koh, Y. H. Hydroxyapatite-coated magnesium implants with improved in vitro and in vivo biocorrosion, biocompatibility, and bone response. *Journal of Biomedical Materials Research Part A* **2014**, *102* (2), 429-441.
- (151) Sun, J.; Cai, S.; Wei, J.; Ling, R.; Liu, J.; Xu, G. Long-term corrosion resistance and fast mineralization behavior of micro-nano hydroxyapatite coated magnesium alloy in vitro. *Ceramics International* **2020**, *46* (1), 824-832.
- (152) Gao, Y. L.; Liu, Y.; Song, X. Y. Plasma-sprayed hydroxyapatite coating for improved corrosion resistance and bioactivity of magnesium alloy. *Journal of Thermal Spray Technology* **2018**, *27* (8), 1381-1387.
- (153) Rau, J.; Antoniac, I.; Filipescu, M.; Cotrut, C.; Fosca, M.; Nistor, L.; Birjega, R.; Dinescu, M. Hydroxyapatite coatings on Mg-Ca alloy prepared by pulsed laser deposition: properties and corrosion resistance in simulated body fluid. *Ceramics International* **2018**, *44* (14), 16678-16687.
- (154) Prakash, C.; Singh, S.; Pabla, B.; Uddin, M. Synthesis, characterization, corrosion and bioactivity investigation of nano-HA coating deposited on biodegradable Mg-Zn-Mn alloy. *Surface and Coatings Technology* **2018**, *346*, 9-18.

- (155) Kang, Z.; Zhang, J.; Niu, L. A one-step hydrothermal process to fabricate superhydrophobic hydroxyapatite coatings and determination of their properties. *Surface and Coatings Technology* **2018**, *334*, 84-89.
- (156) Maurya, R.; Siddiqui, A. R.; Balani, K. In vitro degradation and biomineralization ability of hydroxyapatite coated Mg-9Li-7Al-1Sn and Mg-9Li-5Al-3Sn-1Zn alloys. *Surface and Coatings Technology* **2017**, *325*, 65-74.
- (157) Mukhametkaliyev, T.; Surmeneva, M.; Vladescu, A.; Cotrut, C. M.; Braic, M.; Dinu, M.; Vranceanu, M.; Pana, I.; Mueller, M.; Surmenev, R. A biodegradable AZ91 magnesium alloy coated with a thin nanostructured hydroxyapatite for improving the corrosion resistance. *Materials Science and Engineering: C* **2017**, *75*, 95-103.
- (158) Dunne, C. F.; Levy, G. K.; Hakimi, O.; Aghion, E.; Twomey, B.; Stanton, K. T. Corrosion behaviour of biodegradable magnesium alloys with hydroxyapatite coatings. *Surface and Coatings Technology* **2016**, *289*, 37-44.
- (159) Kumar, R. M.; Kuntal, K. K.; Singh, S.; Gupta, P.; Bhushan, B.; Gopinath, P.; Lahiri, D. Electrophoretic deposition of hydroxyapatite coating on Mg-3Zn alloy for orthopaedic application. *Surface and Coatings Technology* **2016**, *287*, 82-92.
- (160) Hiromoto, S.; Inoue, M.; Taguchi, T.; Yamane, M.; Ohtsu, N. In vitro and in vivo biocompatibility and corrosion behaviour of a bioabsorbable magnesium alloy coated with octacalcium phosphate and hydroxyapatite. *Acta biomaterialia* **2015**, *11*, 520-530.
- (161) Yang, H.; Yan, X.; Ling, M.; Xiong, Z.; Ou, C.; Lu, W. In vitro corrosion and cytocompatibility properties of nano-whisker hydroxyapatite coating on magnesium alloy for bone tissue engineering applications. *International journal of molecular sciences* **2015**, *16* (3), 6113-6123.
- (162) Shen, S.; Cai, S.; Li, Y.; Ling, R.; Zhang, F.; Xu, G.; Wang, F. Microwave aqueous synthesis of hydroxyapatite bilayer coating on magnesium alloy for orthopedic application. *Chemical Engineering Journal* **2017**, *309*, 278-287.
- (163) Lim, H. K.; Byun, S. H.; Lee, J. Y.; Lee, J. W.; Kim, S. M.; Lee, S. M.; Kim, H. E.; Lee, J. H. Radiological, histological, and hematological evaluation of hydroxyapatite-coated resorbable magnesium alloy screws placed in rabbit tibia. *Journal of Biomedical Materials Research Part B* **2017**, *105* (6), 1636-1644.
- (164) Lim, H.-K.; Byun, S.-H.; Woo, J.-M.; Kim, S.-M.; Lee, S.-M.; Kim, B.-J.; Kim, H.-E.; Lee, J.-W.; Kim, S.-M.; Lee, J.-H. Biocompatibility and biocorrosion of hydroxyapatite-coated magnesium plate: animal experiment. *Materials* **2017**, *10* (10), 1149.

- (165) Byun, S.-H.; Lim, H.-K.; Kim, S.-M.; Lee, S.-M.; Kim, H.-E.; Lee, J.-H. The bioresorption and guided bone regeneration of absorbable hydroxyapatite-coated magnesium mesh. *Journal of Craniofacial Surgery* **2017**, *28* (2), 518-523.
- (166) Tian, Q.; Lin, J.; Rivera-Castaneda, L.; Tسانhani, A.; Dunn, Z. S.; Rodriguez, A.; Aslani, A.; Liu, H. Nano-to-Submicron Hydroxyapatite Coatings for Magnesium-based Bioresorbable Implants–Deposition, Characterization, Degradation, Mechanical Properties, and Cytocompatibility. *Scientific reports* **2019**, *9* (1), 810.
- (167) Li, Q.; Jiang, G.; Wang, D.; Wang, H.; Ding, L.; He, G. Porous magnesium loaded with gentamicin sulphate and in vitro release behavior. *Materials Science and Engineering: C* **2016**, *69*, 154-159.
- (168) Little, M. A.; Kalkhoran, N. M.; Aslani, A.; Tobin, E. J.; Burns, J. E., Process for depositing calcium phosphate therapeutic coatings with different release rates and a prosthesis coated via the process. Google Patents: 2011.
- (169) Cipriano, A. F.; Lin, J.; Miller, C.; Lin, A.; Alcaraz, M. C. C.; Soria Jr, P.; Liu, H. Anodization of magnesium for biomedical applications–Processing, characterization, degradation and cytocompatibility. *Acta Biomater.* **2017**, *62*, 397-417.
- (170) Nguyen, N.-Y. T.; Grelling, N.; Wetteland, C. L.; Rosario, R.; Liu, H. Antimicrobial Activities and Mechanisms of Magnesium Oxide Nanoparticles (nMgO) against Pathogenic Bacteria, Yeasts, and Biofilms. *Scientific Report* **2018**, *8* (1), 16260.
- (171) Simchi, A.; Tamjid, E.; Pishbin, F.; Boccaccini, A. Recent progress in inorganic and composite coatings with bactericidal capability for orthopaedic applications. *Nanomedicine: Nanotechnology, Biology and Medicine* **2011**, *7* (1), 22-39.
- (172) Cipriano, A. F.; Lin, J.; Lin, A.; Sallee, A.; Le, B.; Cortez Alcaraz, M. C.; Guan, R.-G.; Botimer, G.; Inceoğlu, S.; Liu, H. Degradation of Bioresorbable Mg–4Zn–1Sr Intramedullary Pins and Associated Biological Responses in Vitro and in Vivo. *ACS Applied Materials & Interfaces* **2017**, *9* (51), 44332-44355.
- (173) Ge, X.; Leng, Y.; Bao, C.; Xu, S. L.; Wang, R.; Ren, F. Antibacterial coatings of fluoridated hydroxyapatite for percutaneous implants. *Journal of Biomedical Materials Research Part A* **2010**, *95* (2), 588-599.
- (174) Baskar, K.; Anusuya, T.; Venkatasubbu, G. D. Mechanistic investigation on microbial toxicity of nano hydroxyapatite on implant associated pathogens. *Materials Science and Engineering: C* **2017**, *73*, 8-14.